Controlled initiation and quantitative visualization of cell interaction dynamics

- a novel hybrid microscopy method -

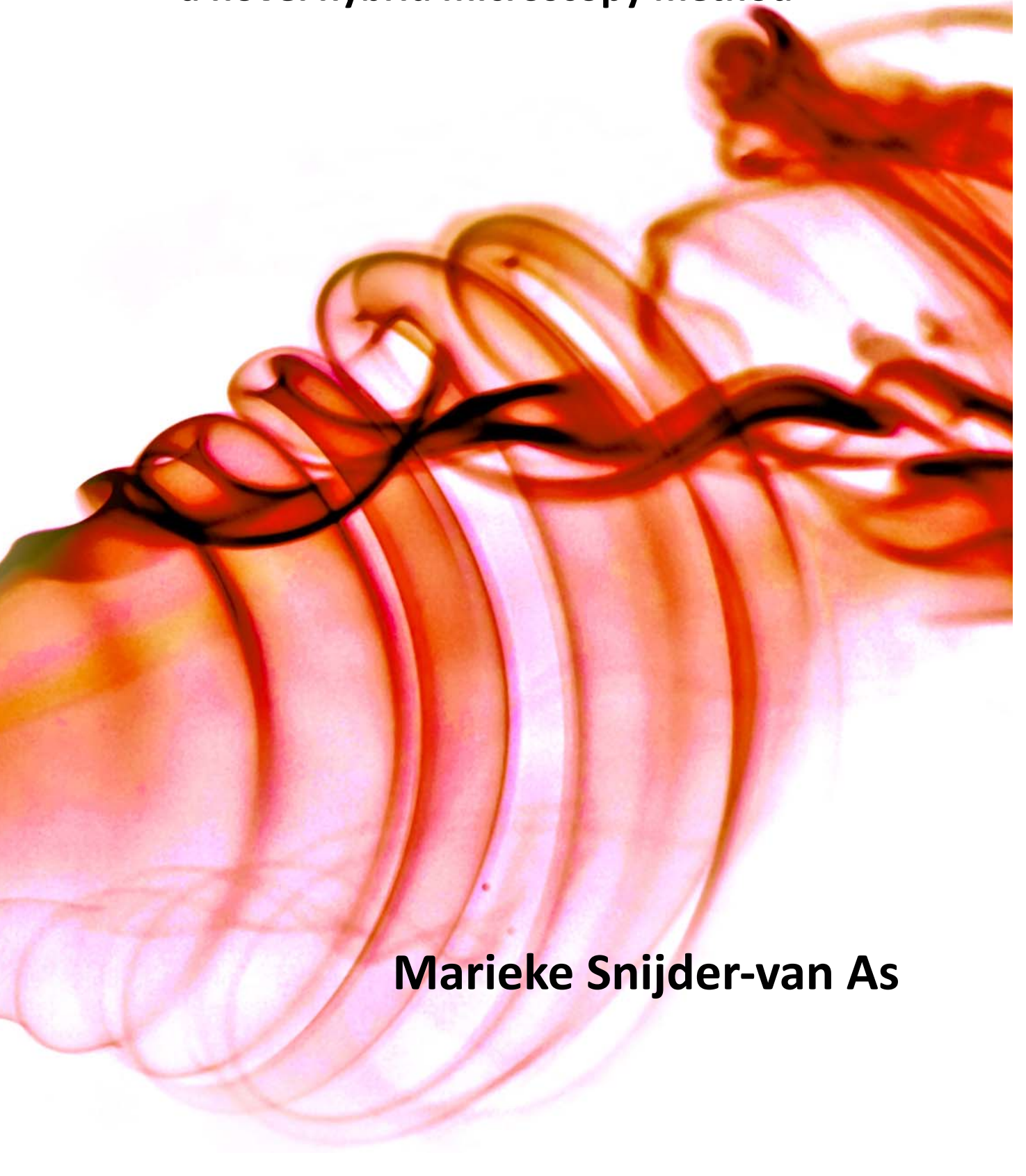

Marieke Snijder-van As

Controlled initiation and quantitative visualization of cell interaction dynamics

- a novel hybrid microscopy method -

Marieke Snijder-van As

Thesis committee members:

Prof. dr.	C.A. van Blitterswijk	University of Twente (chairman)
Prof. dr.	V. Subramaniam	University of Twente (promotor)
Dr.	J.S. Kanger	University of Twente (assistant-promotor)
Prof. dr.	P.M.W. French	Imperial College London
Prof. dr.	J. Neefjes	The Netherlands Cancer Institute
Dr.	A. Cambi	Radboud University Nijmegen Medical Centre
Dr.	B. Rieger	Delft University of Technology
Prof. dr.	K.J. Boller	University of Twente
Prof. dr.	L.W.M.M. Terstappen	University of Twente

The work described in this thesis was performed at the Nanobiophysics (previously Biophysical Engineering) group, MIRA Institute for biomedical technology and technical medicine, Faculty of Science and Technology, University of Twente, PO Box 217, 7500 AE Enschede, The Netherlands.

This research was partially financially supported by the Netherlands Organisation for Scientific Research (NWO-ALW, project 812.08.004), the Institute for Biomedical Technology (BMTI) and the faculty of Science and Technology.

ISBN: 978-90-365-3125-2
DOI: 10.3990/1.9789036531252

Cover design: Marieke Snijder-van As, image by courtesy of Brian Lary.
Printed by Wöhrmann Print Service, Zutphen, The Netherlands

CONTROLLED INITIATION AND QUANTITATIVE VISUALIZATION OF CELL INTERACTION DYNAMICS
- A NOVEL HYBRID MICROSCOPY METHOD -

PROEFSCHRIFT

ter verkrijging van
de graad van doctor aan de Universiteit Twente,
op gezag van de rector magnificus,
prof. dr. H. Brinksma,
volgens besluit van het College voor Promoties
in het openbaar te verdedigen
op donderdag 2 december 2010 om 15.00 uur

door

Martje Ieke van As
geboren op 15 november 1980
te Rotterdam

Dit proefschrift is goedgekeurd door:

Prof. dr. V. Subramaniam (promotor), en
Dr. J.S. Kanger (assistent-promotor)

Table of contents

Chapter 1 –

Introduction

1.1 Motivation

Cell interactions are fundamental to all living organisms. For example, cells interact with the extracellular matrix, blood cells interact with the blood vessel wall, nerve cells pass on signals from the sensory system and back to the motor system, and muscle cells contract and slide over each other during movement. Furthermore, in the adaptive immune system, dendritic cells sense foreign pathogens. These dendritic cells communicate the existence of the infection to other cells, which then fight the infected tissue. Cells interact with their environment via proteins on their plasma membranes. The expression level, organisation and function vary between the many different membrane proteins and cell types (Lodish et al., 2000). Upon interaction, membrane proteins often redistribute. Both the spatial organisation and the dynamics of the molecules are important for cell signalling (Dustin, 2009). A widely used powerful method to study these aspects is fluorescence microscopy. Especially the use of fluorescent proteins allows the visualization of specific molecules with high resolution. High resolution and high fidelity visualisation of the dynamics of membrane molecules requires that the interaction of a cell with a substrate or another cell is observed from the onset of interaction, and that the interaction site is aligned parallel to the focal plane of the objective. These requirements are not generally fulfilled. Current techniques are both limited in controlling the position of interaction (in (x,y,z,t)) and monitoring the interaction (Treanor and Batista, 2007).

The aim of this thesis is to develop, test, and use a method capable of visualizing the dynamics of membrane proteins with high spatial and temporal resolution. The approach comprises the control over the onset of interaction and the spatial position of interaction. The plane of interaction should be aligned parallel to the focal plane of the objective.

The following two quotes demonstrate clearly the importance of, and limitations in the field of fluorescence microscopy:

> "The trend is clear: fluorescence microscopy will have an increasingly important role in cell biology, shaping the way cell biologists approach questions and providing quantitative information that complements and extends traditional biochemical techniques" (Lidke and Wilson, 2009)

> "Live cell fluorescence microscopy has been used to study the developing immunological synapse (IS; see section 1.3, *M.I.S-A*) at cell-cell interactions. While this approach is highly physiological, it presents several drawbacks for rapidly imaging the dynamic events occurring at the IS. The complex topology of the cell-cell interaction requires z-stack acquisition limiting not only the temporal resolution but often the spatial resolution, which is sacrificed in order to decrease acquisition time. In addition, it is difficult to visualize the earliest events of lymphocyte activation because of the impossibility in predicting where cell conjugates will form." (Treanor and Batista, 2007)

To achieve our goal and address both the issue of the onset of interaction and of the spatial resolution, we combine high resolution fluorescence imaging with optical tweezers. Fluorescence imaging is used to measure protein dynamics by studying the fluorescence distribution of the ensemble of molecules in the interaction site, while optical tweezers (OT) are used to control the position and onset of interaction.

This chapter introduces and discusses fluorescence microscopy, total internal reflection fluorescence (TIRF) microscopy and OT. The main concepts of

immunobiology are introduced, in order to gain insight into the biological system that is of interest for the study described in this thesis. Finally, this chapter gives an outline of the thesis.

1.2 Fluorescence microscopy

The development of the microscope by Antoni van Leeuwenhoek (1632-1723) opened up the possibilities of observing processes at much smaller length scales than heretofore possible. Since then, the development of the microscope has not stopped, and nowadays many different microscopy approaches are available to study processes on molecular and cellular scale (micrometer and nanometer scale), often making use of fluorescence labelling. This section introduces important concepts in fluorescence and microscopy.

1.2.1 Fluorescence

Fig. 1.1A shows the Jablonski diagram of the fluorescence process. A molecule absorbs a photon to go from the ground state to one of the levels in the excited state. Via internal conversion the molecule relaxes into the lowest level of the first excited state. Here, it can energetically relax to the ground state by emitting a photon. Since this photon has a lower energy than the absorbed one, it has a longer wavelength. The time the molecule is in the excited state before relaxing to the ground state is the fluorescence lifetime. The excitation spectrum gives the efficiency of excitation over a range of wavelengths, while the emission spectrum gives the wavelength distribution of the emitted photons.

To visualize the dynamics of molecules, a fluorescent dye or a fluorescent protein can be attached to the molecule of interest and monitored with fluorescence microscopy (Giepmans et al., 2006). The discovery of the green fluorescent protein (GFP) from jellyfish, and the ability to genetically encode it as a marker for other proteins of interest, brought a revolution in the application of fluorescence microscopy in cell biology. Specific proteins inside the living cell can be tagged with a green fluorescent protein variant by genetic modification, enabling the visualization of the dynamics of the protein of interest in cells in a minimally invasive manner and without the use of toxic dyes. Tsien and others have engineered several mutants of GFP, including the monomeric red fluorescent

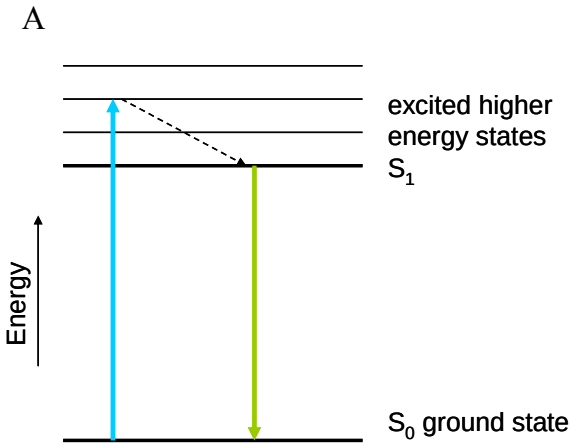

Fig. 1.1 Fluorescence
A. Jablonski diagram showing the energy states involved in fluorescence. The blue arrow indicates an absorbed photon, and after internal conversion (black arrow) the molecule emits a photon (green arrow) B. Several fluorescent proteins with different excitation and emission wavelength ("Reprinted with small adaptations from Tsien, R. Y. (2005) "Building and breeding molecules to spy on cells and tumors." FEBS Letters 579(4): 927, Copyright 2005, with permission from Elsevier")

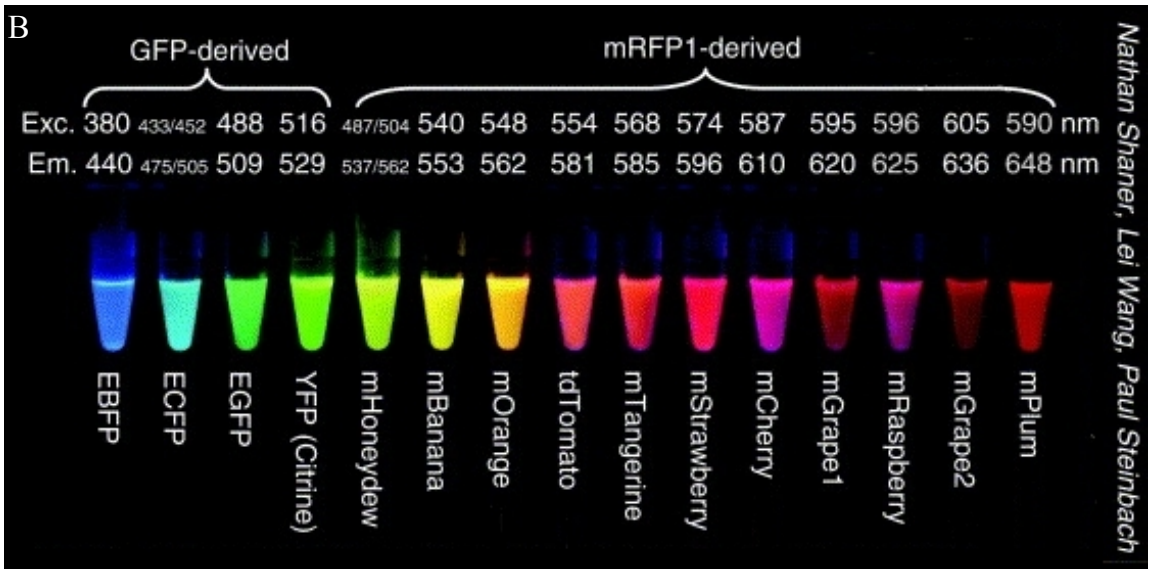

protein (mRFP) used in this thesis, emitting at different wavelengths, as displayed in Fig. 1.1B (Tsien, 2005). Therefore, different proteins can be tagged with different coloured fluorescent proteins and imaged simultaneously.

The application of fluorescence microscopy in cell biology is hampered by photobleaching (which limits the total signal that can be measured) and by autofluorescence of the cell. Therefore, the challenge in fluorescence microscopy lies in the detection of low fluorescence intensities with a high signal-to-background ratio.

1.2.2 Microscopy

Microscopy enables the study of small objects. However, conventional widefield microscopy has a diffraction limited axial and lateral resolution. The lateral resolution is given by the diffraction limit (*d*) and the range of depth in the axial direction that is in focus on the camera is given by the focal depth (*DOF*):

$$d = 0.61\lambda / NA \qquad \text{Eq. 1.1}$$

$$DOF = 2\frac{\lambda n}{NA^2} \qquad \text{Eq. 1.2}$$

where λ is the wavelength, and *NA* is the numerical aperture of the objective, defined by the maximum angle for which a ray can still pass through the objective (θ_m), and the refractive index of the medium adjacent to the objective (*n*):

$$NA = n \sin \theta_m \qquad \text{Eq. 1.3}$$

Considering GFP, with a peak in the emission spectrum at 525 nm, and a water immersion objective with NA=1.2, this gives $d \approx 270$ nm and $DOF \approx 1$ μm. Therefore, we can not distinguish individual molecules that are separated over a distance less than *d* (although the individual molecules are typically ~30x smaller than *d*) without adaptations to the microscope.

Several methods have been developed to increase the precision either in the (*x,y*) or (*z*)-direction. For example, confocal microscopy uses a pinhole in the detection path; only the light in focus will be projected on the detector, decreasing both the axial and lateral resolution (as will be discussed in more detail in chapter 5). Another possibility is very local illumination with a thin probe, as is done in near-field scanning optical microscopy (NSOM); this method improves the lateral precision while simultaneously giving information on the height profile of the sample (Betzig et al., 1986, Chen et al., 2010, van Zanten et al., 2010). Other microscopy methods have been developed to specifically study the molecular dynamics and proximity of molecules to each other. For example, single particle tracking (SPT) uses a low concentration of fluorophores, so every single fluorophore can be traced independently of the others, giving information on diffusion and directed motion (Chen et al., 2006, Owen et al., 2009). Furthermore, in fluorescence recovery after photobleaching (FRAP), a small area of interest is photobleached and the recovery of fluorescence intensity is a measure for diffusion

and mobility of the bleached molecule (Axelrod et al., 1976, Mavrakis et al., 2009, Owen et al., 2009, Reits and Neefjes, 2001). As a last example, in fluorescence resonance energy transfer (FRET) experiments the energy transfer from a donor to an acceptor fluorophore is measured. Since energy transfer is a strongly distance-dependent phenomenon that is efficient only at distances on the order of 5-10 nm, FRET experiments provide information on the proximity of the molecules of interest (Jares-Erijman and Jovin, 2006, van der Krogt et al., 2008, Wessels et al., 2010). Furthermore, high resolution can be achieved by using photoactivatable fluorophores. For further information on these and other optical microscopy methods in imaging cell biology, see the following reviews for examples (Garcia-Saez and Schwille, 2010, Jaiswal and Simon, 2007, Lidke and Wilson, 2009, Navratil et al., 2006, Treanor and Batista, 2007).

Since we aim to study cell membrane proteins, preferably we would like to image only these surface proteins. This can be achieved by TIRF microscopy. TIRF microscopy uses an evanescent wave to illuminate the sample only very close (~100-300 nm) to a glass-water interface, in this way achieving a high axial resolution. Because this versatile method to study membrane protein dynamics forms the basis of the visualisation approach used in this thesis, this technique is discussed in more detail in section 1.3. Furthermore, TIRF microscopy is not a scanning technique, but uses a camera for detection. This opens up the possibility to study faster processes than for example with confocal laser scanning microscopy (CLSM), which is limited to a measurement frequency of ~ 1 Hz.

1.3 Total internal reflection fluorescence microscopy

In total internal reflection fluorescence (TIRF) microscopy, fluorophores are excited by an evanescent field generated at the interface between two media having different refractive indices. Fig. 1.2 schematically depicts the principle of TIRF microscopy. If a beam of light is incident (at an angle θ_i) with an interface between two media with refractive indices n_1 and n_2, respectively, and $n_1 > n_2$, the light will be totally reflected for $\theta_i > \theta_c$, where θ_c is the critical angle: $\theta_c = \sin^{-1}(n_2 / n_1)$. In

this case, an evanescent field exists in the lower refractive index material. For $\theta_i \geq \theta_c$, the intensity profile is given by:

$$I(z) = I_0 e^{-z/d_p} \qquad \text{Eq. 1.4}$$

where z is the direction perpendicular to the interface and I_0 is the intensity at the interface (depending on the angle of incidence, the refractive indices and the polarization of the light), and d_p is the penetration depth, given by

$$d_p = \frac{\lambda}{4\pi}\left(n_1^2 \sin^2\theta_i - n_2^2\right)^{-1/2} \qquad \text{Eq. 1.5}$$

where λ is the wavelength of the light. Although Eq. 1.4 and 1.5 are derived for an infinite beam width, in practise, these equations are approximately equal to those of finite width, focused Gaussian beams (Axelrod, 2007).

In the specific situation of GFP (excited with 488 nm light), $n_1=n_{glass}=1.51$ and $n_2=n_{water}=1.33$, and θ_i = 63 deg, the penetration depth is d_p=190 nm. Since the thickness of a membrane is ~ 10 nm (Lodish et al., 2000), TIRF microscopy can excite the fluorescently tagged membrane proteins. And since the thickness of a cell is upto ~ 15 μm (measurements later in this thesis), TIRF illumination gives low interference from out-of-focus fluorescence from the other side of the cell or from

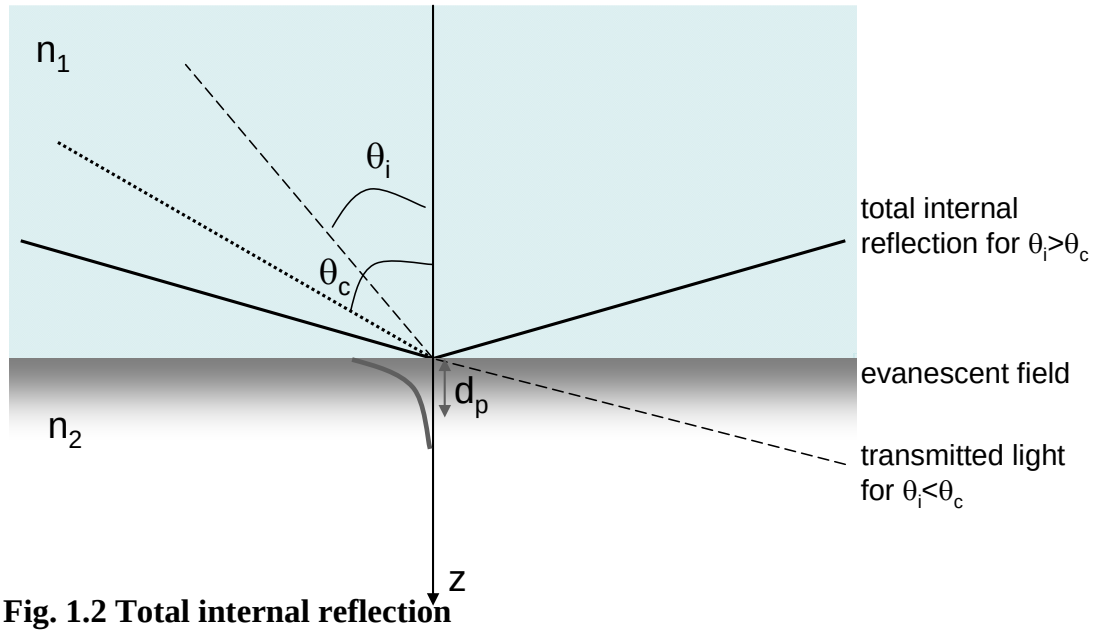

Fig. 1.2 Total internal reflection
Light incident under an angle with the optical axis (z) on a interface between two media with refractive indices n_1 and n_2 ($n_1>n_2$) is refracted for $\theta_i<\theta_c$ (dashed line) or totally reflected for $\theta_i>\theta_c$ (solid line), where the dotted line indicates the critical angle θ_c. Upon total internal reflection, an evanescent field is created with an exponentially decaying intensity (gray to white transition), with a penetration depth d_p.

autofluorescence of the cell. This low penetration depth gives TIRF microscopy a high axial resolution compared to the *DOF* limiting the axial resolution in conventional microscopy (~1 μm). The high signal-to-background ratio is the main advantage of TIRF microscopy, since only fluorophores close to the interface will be excited and out-of-focus light is reduced. This high signal-to-background ratio makes TIRF microscopy a suitable technique for imaging the cell membrane of a cell close to the glass. With TIRF microscopy, we can study the adhesion of a cell to a (functionalized) substrate, see for an example (Mashanov et al., 2003) and the dynamics of membrane proteins upon adhesion (Kaizuka et al., 2009). Furthermore, it is possible to combine TIRF microscopy with other techniques, for example, FRAP and SPT to determine mobility (Toomre and Manstein, 2001), or FRET and polarization measurements to determine vicinity and orientation of the fluorophores (Axelrod, 2007).

1.3.1 Functionalized substrates for TIRF microscopy

Although the low penetration depth is the main advantage of TIRF microscopy (high signal-to-background), it also sets the limitation that fluorophores at distances beyond the extent of the evanescent field cannot be excited. This limits the application of TIRF microscopy for the study of cell-cell interactions. Chapter 5 describes investigations that address this issue for cell-cell interactions. A method to circumvent this issue is to use functionalized substrates that mimic the membrane of another cell and study with TIRF microscopy the interaction of a cell with this functionalized glass substrate. In this case, one or more molecules of interest can be positioned on a glass surface, and a cell interacting with this substrate is expected to respond to the stimulus of the substrate in a similar way as to another cell.

Substrates can be functionalized in several ways, either directly by adsorption to the substrate, or indirectly in supported lipid bilayers. Incubation of the molecule of interest (for example, a protein) on a glass substrate is the most simple method of surface functionalization. The protein will stick to the glass by attractive forces such as electrostatic interactions. A limitation of this method is that the amount of adsorption depends on the type of substrates and proteins used, and the orientation of the molecules can hardly be controlled. This can be addressed by the use of self assembled monolayers, which coat the surface with a specifically

oriented layer, which then can be functionalized with the protein of interest (see for example review by (Yan et al., 2004)). This direct surface functionalization can be performed as well with various techniques to pattern the substrate, for example using stamps (see for a review (Hook et al., 2009)). Using patterned surfaces enables the study of the influence of distribution of (several) proteins on cell responses.

Surface functionalization performed by lipid bilayers enables the incorporation of the molecule(s) of interest in the bilayer. This molecule, incorporated in the membrane with a lipid or transmembrane tail, will still be able to move laterally in the membrane. This method, therefore, resembles the mobility of the membrane proteins more than the direct adsorption of the molecule to the glass. For more information on supported lipid bilayers, see for example the review by (Groves and Dustin, 2003).

In this thesis, we use the simplest method for surface functionalization to develop and test our TIRF-OT microscope: adsorption of the molecule of interest to the glass surface (if necessary via a linker).

1.4 Optical tweezers

Optical tweezers (OT) refers to the use of a focussed laser beam to trap particles (for example, polystyrene beads and cells). OT exploits the momentum carried by photons. Considering a beam of light focussed at a dielectric particle that has a diameter larger than the wavelength, Fig. 1.3 schematically depicts the forces exerted on the particle by a beam of light. On the surface of the particle, light is reflected, giving rise to a scattering force, the magnitude of which increases upon larger refractive indices differences between the particle and its surroundings. Part of the light will be refracted by the particle, giving rise to a change in momentum of the light and, consequently, a change in momentum of the particle. If the intensity of the light is varying across the particle, this change in momentum varies correspondingly, which results in a net force pointed in the direction of higher intensity (Fig. 1.3A). This force is referred to as the gradient force.

If the light is strongly focused, the particle is directed to the focal point by the gradient force (Fig. 1.3B) (Ashkin et al., 1986). Simultaneously, the scattering force pushes the particle in the propagation direction of the incident light. When the

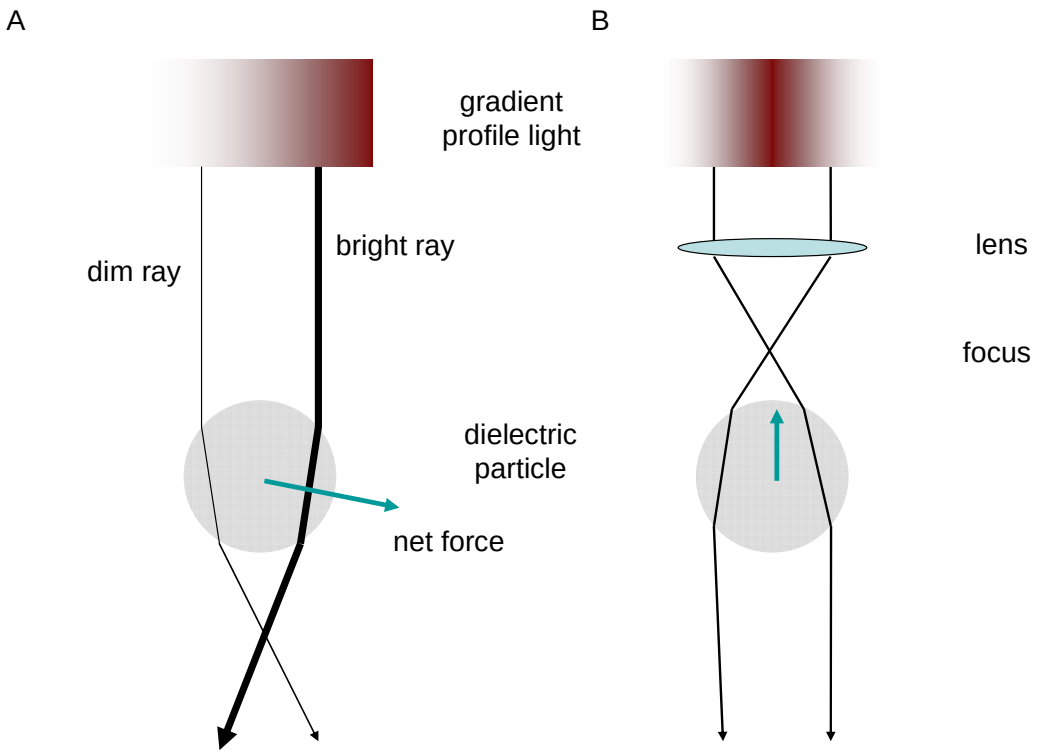

Fig. 1.3 Optical Tweezers A) Non-focussed light beam with a gradient in intensity interacts with a dielectric particle. The light is refracted and due to the gradient in intensity, a net force is directed towards the high intensity light. B) A focused light beam with a symmetrical intensity gradient, for example, a Gaussian beam, enables stable trapping of the particle in the focus of the light (highest intensity point).

scattering force and the gradient force are of equal magnitude but oppositely directed, the net force on the particle is zero, resulting in a trapping position of the particle just below the focus.

The force exerted by OT on the trapped particle is linear with the laser power, and further depends on the refractive index contrast of the particle with its surroundings, the NA of the objective, and the particle size (Svoboda and Block, 1994). Optical tweezers can trap cells, since cells have a higher refractive index than their surrounding (~1.38 (van Manen et al., 2008) compared to 1.33 for water). The size and the refractive index of a cell cannot be adjusted, so the force needed to trap and move a particle has to be adjusted by the power of the laser. However, high laser intensities can cause cell damage due to, for example, heating caused by absorption of the light. Therefore, the absorption of water and proteins at the wavelength used should be as low as possible. This is fulfilled for wavelengths in the (near) infrared region (Ramser and Hanstorp, 2010).

Besides implementing single optical tweezers in a microscope, it is possible to create multiple traps. This could be done, for example, by separating the light of a laser beam by a polarizing beam splitter and creating optical tweezers from both polarized light paths (Fällman and Axner, 1997). Another method, able to create multiple optical traps, is the use of a spatial light modulator that shapes the beam such that the light is focussed at different positions in the field of view, and that these focal points can be individually moved (Dufresne and Grier, 1998). Optical tweezers generated by this method are called holographic optical tweezers.

The combination of OT with fluorescence microscopy has been used to study single molecules (for example, (Murade et al., 2009)) and cells (review by (Ramser and Hanstorp, 2010)). Furthermore, optical tweezers recently have been applied for alignment of the interaction site between two cells parallel to the focal plane of the objective (Oddos et al., 2008) and for the possibility to induce the interaction ((McNerney et al., 2010), and this work). Also the combination of TIRF microscopy and optical tweezers has been described recently (Kyoung et al., 2007). However, this combination has not been used to study cell interactions from the onset of interaction, as will be the aim in this thesis.

Alternatives for manipulation of cells are, for example, the use of micropipettes. However, the advantage of OT over micropipettes is that they do not physically contact the cell, thereby avoiding any adverse influence due to contact with the cell. Besides, OT can be used versatilely in microfluidic ‘closed’ systems. If the wavelength and power are chosen correctly, OT provides a clean, minimally disturbing means of studying cell processes (Sheetz, 1998). Therefore, we will use OT to control the positioning (in space and time) for the visualisation of cell interactions.

1.5 Cell interactions in the immune system

In this thesis, we focus on cells from the immune system. This section introduces some aspects of adaptive immunity (1.5.1), the molecular interactions and dynamics of cellular interactions between cells in the adaptive immune system (1.5.2), and the proteins studied in this thesis (1.5.3).

1.5.1 Innate and adaptive immunity

The immune system protects the body from pathogens, like viruses and bacteria, and abnormal, for example cancerous, cells. All cells of the immune system are derived from the precursor of all blood cells, the pluripotent hematopoietic stem cell in the bone marrow. From this stem cell, red blood cells, platelets and two main categories of white blood cells are derived, the latter being the immune cells (Janeway Jr. et al., 2005). The two categories are immune cells from the myeloid lineage, like macrophages and antigen presenting dendritic cells (DCs), and cells from the lymphoid lineage, like T-cells (matured in the thymus) and B-cells (matured in the bone marrow).

Classically, the immune system is divided in two parts: the innate and the adaptive immune system. The innate immune response is an early reaction to pathogens, recognizing common features of these pathogens and discriminating them from the molecules familiar to the body. In innate immunity, phagocytic macrophages recognize and bind pathogens, upon which these macrophages are activated and secrete molecules initiating inflammation. However, the innate immune system depends on recognition of invariant receptors and, therefore, only recognizes common features of pathogens. Many pathogens can overcome actions of the innate immune system and, besides, the innate immunity does not lead to immunological memory. To overcome these limitations, another function of the innate immune system is to help triggering the adaptive immune response. This is achieved by cells of the innate immune system secreting inflammatory cytokines which leads to activation of other immune cells and by antigen presentation of digests of pathogens. For example, DCs can endocytose non-self antigens and present peptides derived from these antigens on their cell surface to T-cells (Janeway Jr. et al., 2005).

A central principle of the adaptive immune response is the variations in the antigen-receptor binding-site (Janeway Jr. et al., 2005). Clonal selection, that is, rearranging the receptor gene segments during development of the lymphocyte, generates a cell presenting multiple molecules of one unique antigen receptor. This holds both for the B-cell receptor on B-cells, capable of producing antigen specific antibodies, as well as for the T-cell receptor on T-cells, capable of recognizing and destroying infected cells. By clonal deletion the self-reactive receptors are removed

during development of an embryo, because otherwise adaptive immune responses might occur against self antigens, resulting in autodestruction, a phenomenon seen in autoimmune diseases.

Upon high affinity interaction from a foreign molecule presented by an antigen-presenting cell, like a DC, with a T-cell receptor on a lymphocyte, this T-cell becomes activated and will differentiate into effector T-cells with the same specificity for this foreign molecule. Such T-cells will destroy pathogen infected cells, or activate other immune cells in order to fight infection. In addition, antigen specific B-cells can secrete antibodies. After the pathogen has been eliminated, memory T- and B-cells will stay present, ensuring a more rapid and effective response upon a second infection.

1.5.2 T-cell activation

Activation of T-cells is critical to the initiation of the adaptive immune response. The process of this response is schematically depicted in Fig. 1.4A. First, DCs encounter pathogens, endocytose these pathogens and fragment the pathogens into small peptides. Second, the DC matures, migrates to the lymph nodes and presents the peptides bound to major histocompatibility complexes (MHCs) on their cell surface. Third, the DC interacts with T-cells in the lymph node. The peptide-MHC complex on the DC can be recognized by the T-cell receptor (TCR) on the T-cell. Only when the TCR specifically recognises this peptide-MHC complex with its unique antigen receptor composition, the T-cell will be activated. Fourth, the activated T-cells proliferate and develop into effector T-cells which interfere with the pathogen or infected cells.

Fig. 1.4B depicts a detailed schematic of proteins involved in the interaction of a DC with a T-cell. Not only the peptide-MHC complex and the TCR are engaged, but also other proteins are required during the DC-T-cell interaction. The membrane proteins involved have specific tasks in the interaction, although the line between the adhesion function, to stabilise the interaction, and the costimulatory function, to generate intracellular signals, is often not clear (Dustin, 2007). Contact initiation and stabilisation occurs, for example, by binding of LFA-1 (leukocyte function-associated antigen 1) on T-cells to ICAM-1 (intercellular adhesion molecule 1) on DCs (Grakoui et al., 1999). Costimulation of the T-cell occurs, for

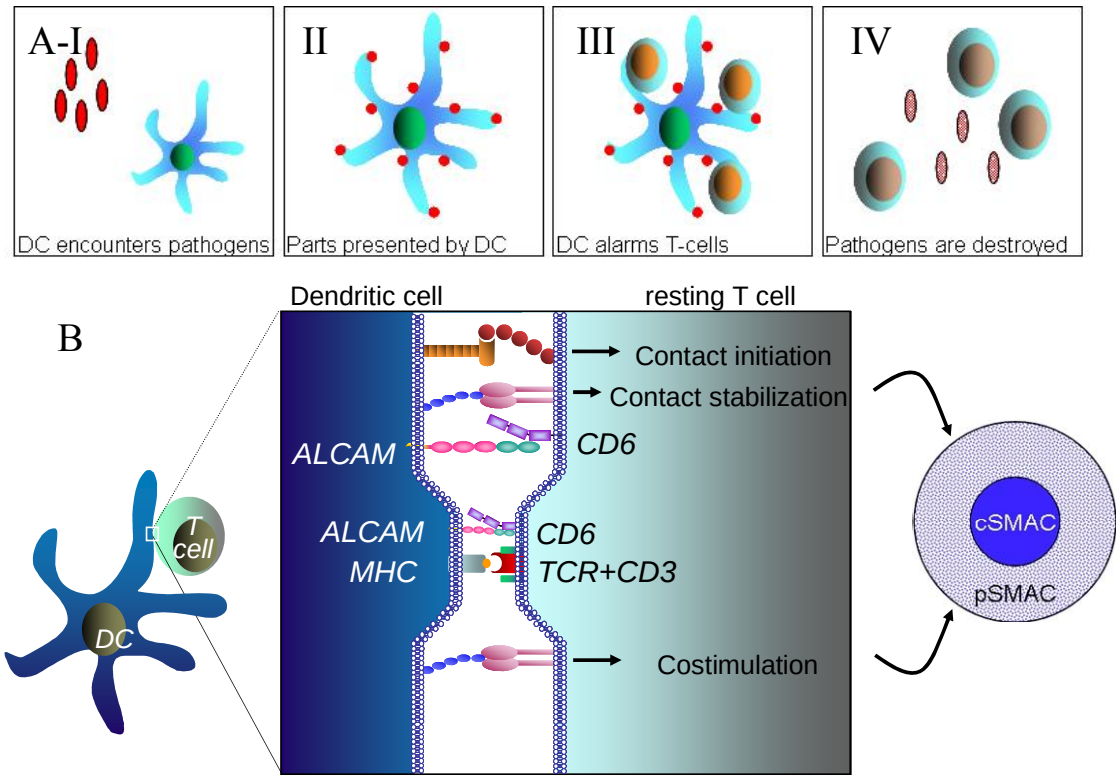

Fig. 1.4 T-cell activation A. Schematic representation of the adaptive immune response, where a DC encounters a pathogen (I) and presents peptides on is cell surface (II). The DC interacts with T-cell (III), which evolve in effector cells to interfere with the infection (IV). B. Schematic representation of the immunological synapse: a zoom in of the side view (middle) of the DC-T-cell interaction in which various membrane molecules play a role. These molecules are organized in a central (c) and peripheral (p) supramolecular activation cluster (c/p-SMAC), depicted with a top view at the left.

example, by CD4[1] or CD8 on the T-cell; without these proteins no optimal signalling occurs. Furthermore, CD3, which forms a complex with the TCR, is required for cell-surface expression of the TCR and signal transduction by the TCR (Janeway Jr. et al., 2005). Upon contact, the cells are triggered to reorganize cell-surface receptors in the immunological synapse, which has a bullseye-structure (Fig. 1.4B). In the central supramolecular activation complex (cSMAC), the TCR and associated signalling molecules are enriched, and in the peripheral SMAC (pSMAC), among others, LFA-1 can be found. Other proteins, like CD43, seem excluded from the contact area (Lin et al., 2005, Dustin, 2009). It has been proposed that the size of the membrane molecules influences their position in the IS,

[1] CD stands for cluster of differentiation, the international nomenclature to identify and investigate cell surface molecules on white blood cells.

however, also the actin cytoskeleton has a role in this reorganisation (Huppa and Davis, 2003, Burroughs and Wulfing, 2002, Choudhuri et al., 2005, Gaus et al., 2005).

T-cell activation is a complex process involving many molecular interactions on and in the cell. The amount of TCRs bound influences the strength of the signalling, measured by the calcium flux (Huppa and Davis, 2003). Upon interaction, the cytoplasmic tail of CD3 is phosphorylated (a phosphate (PO_4) group is added to the molecule), activating CD3. Mossman et al. (2005) performed an experiment on patterned bilayers and show that the spatial location of the TCR is related to the signalling activity. Furthermore, binding of the TCR or other molecules, like LFA-1, induce cytoskeletal rearrangements necessary for synapse formation (Huppa and Davis, 2003, Billadeau and Burkhardt, 2006). Experiments between nanopatterned, structured bilayers and T-cells show that the movement of TCR molecules by the actin cytoskeleton occurs in clusters (DeMond et al., 2008). These clusters seem to move with the actin via a linkage that allows slip, since the clusters can move around barriers when these barriers are (partially) directed towards the centre of the synapse. This suggests a model in which the relative coupling strength of a membrane molecule to the actin sorts the molecules in the IS (DeMond et al., 2008).

The organisation and the role of the immunological synapse are subject of extensive study. Varma et al. suggest that upon formation of a mature cSMAC, TCR signalling is terminated (2006), for example by internalization of the TCR (Griffiths et al., 2010). Bousso (2008) discusses the arrest of T-cells on dendritic cells monitored with two-photon microscopy, in which the molecular organisation at the interaction site also plays a role. This arrest is related to the symmetry in the segregation of the membrane molecules (Dustin, 2007). Studies of the immunological synapses between a target cell and a cytotoxic T-cell show secretion of molecules by the T-cell (Griffiths et al., 2010). All these processes require orchestrated cellular signalling pathways. Dustin (2009) reviews experimental results on the cellular context of T-cell signalling. He summarizes that the dynamics of TCR microclusters is important for the signalling and that filamentous actin has an important, but not fully understood, role in this (Dustin, 2009, Kaizuka et al., 2007). Until now, most studies have been carried out on cells interacting with

molecules in artificial planar membranes. Studies on cell-cell interactions are limited.

1.5.3 ALCAM and CD6

In this thesis, we focus our attention on two proteins that participate in the immunological synapse: the activated leukocyte cell adhesion molecule (ALCAM) and its ligand CD6, also depicted in Fig. 1.4B.

CD6 is a cell membrane protein, found on thymocytes, T-cells, some B-cells and brain cells (Wee et al., 1993). It consists of three extracellular scavenger receptor cysteine-rich domains, a transmembrane domain and a cytoplasmic domain (Aruffo et al., 1997). ALCAM was characterized as a ligand for CD6 (Bowen et al., 1995), although alternative isoforms have been detected, one of which cannot bind to ALCAM and is up-regulated upon activation of T-cells (Castro et al., 2007). Kobarg et al. (1997) showed by CD3 stimulation that the CD6 cytoplasmic tail influences the calcium flux and that tyrosines in the tail are phosphorylated.

ALCAM (CD166) is a cell surface protein with five extracellular immunoglobulin domains and a small cytoplasmic tail. It is involved in cell adhesion in many different cell types (Swart, 2002), including in cancer metastasis, via homophilic ALCAM-ALCAM interactions. In the latter process the most membrane-distal domain is critical and the actin cytoskeleton is involved (Swart et al., 2005, Nelissen et al., 2000, van Kempen et al., 2001, Zimmerman et al., 2004). In the immune system, ALCAM is highly expressed on dendritic cells, and binds in a heterotypic interaction to CD6 (Zimmerman et al., 2006) with which it colocalizes in the immunological synapse (Gimferrer et al., 2004). The CD6-ALCAM interaction is between the membrane proximal domain of CD6 with the membrane distal domain of ALCAM (Bowen et al., 2000), see Fig. 1.4B. The interaction between ALCAM and CD6 has high affinity, whereas the ALCAM-ALCAM binding has a low affinity (te Riet et al., 2007).

Zimmerman et al. (2006) have shown that CD6 is essential for T-cell proliferation, for stable DC-T-cell contacts, and that CD6 is a costimulatory molecule in T-cell activation. CD6 might perform its function via the binding of SLP-76, a positive regulator of T-cell activation, to the cytoplasmic tail of CD6 (Hassan et al., 2006). Another possibility for CD6 to exert its function is by its

binding to Syntenin-1, a protein that can bind cytoskeletal proteins and signal transduction effectors (Gimferrer et al., 2005).

Although the importance of CD6-ALCAM interactions for DC-T-cell communication has been shown, the distribution dynamics of CD6 and ALCAM during interaction is still largely unknown. Furthermore, the influence of underlying processes, like cytoskeleton rearrangements, has not been quantified. This lack in current understanding motivates to study ALCAM and CD6 dynamics upon interaction, using the hybrid microscope developed in this thesis

1.6 Outline of thesis

In this thesis, we describe the development, testing and usage of a new total internal reflection fluorescence and optical tweezers microscopy method to induce and quantitatively visualize cell-substrate and cell-cell interactions. Chapter 2 describes the development and design of the instrument, flowcell and data analysis. Chapter 3 presents the realization and testing of the novel TIRF-OT microscopy method. As a model system the interaction between functionalized surfaces and cells expressing GFP-tagged ALCAM is studied. In chapter 4, the hybrid TIRF-OT microscope is used to investigate the role of CD6 in cell-cell interactions, by monitoring the dynamics of cell spreading and CD6 recruitment on functionalized surfaces. Chapter 5 studies the applicability of the method for cell-cell interactions. Also, a comparison to alternative methods is given. Finally, chapter 6 gives general conclusions and discussion.

References

ARUFFO, A., BOWEN, M. A., PATEL, D. D., HAYNES, B. F., STARLING, G. C., GEBE, J. A. & BAJORATH, J. 1997. CD6-ligand interactions: a paradigm for SRCR domain function? *Immunology Today,* 18**,** 498-504.

ASHKIN, A., DZIEDZIC, J. M., BJORKHOLM, J. E. & CHU, S. 1986. Observation of a Single-Beam Gradient Force Optical Trap for Dielectric Particles. *Optics Letters,* 11**,** 288-290.

AXELROD, D. 2007. Total Internal Reflection Fluorescence Microscopy. *Optical Imaging and Microscopy.* Berlin: Springer Berlin/Heidelberg.

AXELROD, D., KOPPEL, D. E., SCHLESSINGER, J., ELSON, E. & WEBB, W. W. 1976. Mobility Measurement by Analysis of Fluorescence Photobleaching Recovery Kinetics. *Biophysical Journal,* 16**,** 1055-1069.

BETZIG, E., LEWIS, A., HAROOTUNIAN, A., ISAACSON, M. & KRATSCHMER, E. 1986. NEAR-FIELD SCANNING OPTICAL MICROSCOPY (NSOM) -

DEVELOPMENT AND BIOPHYSICAL APPLICATIONS. *Biophysical Journal,* 49**,** 269-279.

BILLADEAU, D. D. & BURKHARDT, J. K. 2006. Regulation of cytoskeletal dynamics at the immune synapse: New stars join the actin troupe. *Traffic,* 7**,** 1451-1460.

BOUSSO, P. 2008. T-cell activation by dendritic cells in the lymph node: lessons from the movies. *Nature Reviews Immunology,* 8**,** 675-684.

BOWEN, M. A., ARUFFO, A. A. & BAJORATH, J. 2000. Cell surface receptors and their ligands: In vitro analysis of CD6-CD166 interactions. *Proteins-Structure Function and Genetics,* 40**,** 420-428.

BOWEN, M. A., PATEL, D. D., LI, X., MODRELL, B., MALACKO, A. R., WANG, W. C., MARQUARDT, H., NEUBAUER, M., PESANDO, J. M. & FRANCKE, U. 1995. Cloning, mapping, and characterization of activated leukocyte-cell adhesion molecule (ALCAM), a CD6 ligand. *J. Exp. Med.,* 181**,** 2213-2220.

CASTRO, M. A. A., OLIVEIRA, M. I., NUNES, R. J., FABRE, S., BARBOSA, R., PEIXOTO, A., BROWN, M. H., PARNES, J. R., BISMUTH, G., MOREIRA, A., ROCHA, B. & CARMO, A. M. 2007. Extracellular Isoforms of CD6 Generated by Alternative Splicing Regulate Targeting of CD6 to the Immunological Synapse. *J Immunol,* 178**,** 4351-4361.

CHEN, J., PEI, Y., CHEN, Z. & CAI, J. 2010. Quantum dot labeling based on near-field optical imaging of CD44 molecules. *Micron,* 41**,** 198-202.

CHEN, Y., LAGERHOLM, B. C., YANG, B. & JACOBSON, K. 2006. Methods to measure the lateral diffusion of membrane lipids and proteins. *Methods,* 39**,** 147-153.

DEMOND, A. L., MOSSMAN, K. D., STARR, T., DUSTIN, M. L. & GROVES, J. T. 2008. T Cell Receptor Microcluster Transport through Molecular Mazes Reveals Mechanism of Translocation. *Biophys. J.,* 94**,** 3286-3292.

DUFRESNE, E. R. & GRIER, D. G. 1998. Optical tweezer arrays and optical substrates created with diffractive optics. *Review of Scientific Instruments,* 69**,** 1974-1977.

DUSTIN, M. L. 2007. Cell adhesion molecules and actin cytoskeleton at immune synapses and kinapses. *Current Opinion in Cell Biology,* 19**,** 529.

DUSTIN, M. L. 2009. The Cellular Context of T Cell Signaling. *Immunity,* 30**,** 482-492.

FÄLLMAN, E. & AXNER, O. 1997. Design for fully steerable dual-trap optical tweezers. *Appl. Opt.,* 36**,** 2107-2113.

GARCIA-SAEZ, A. J. & SCHWILLE, P. 2010. Surface analysis of membrane dynamics. *Biochimica Et Biophysica Acta-Biomembranes,* 1798**,** 766-776.

GIEPMANS, B. N. G., ADAMS, S. R., ELLISMAN, M. H. & TSIEN, R. Y. 2006. The Fluorescent Toolbox for Assessing Protein Location and Function. *Science,* 312**,** 217-224.

GIMFERRER, I., CALVO, M., MITTELBRUNN, M., FARNOS, M., SARRIAS, M. R., ENRICH, C., VIVES, J., SANCHEZ-MADRID, F. & LOZANO, F. 2004. Relevance of CD6-mediated interactions in T cell activation and proliferation. *Journal Of Immunology,* 173**,** 2262-2270.

GIMFERRER, I., IBANEZ, A., FARNOS, M., SARRIAS, M. R., FENUTRIA, R., ROSELLO, S., ZIMMERMANN, P., DAVID, G., VIVES, J., SERRA-PAGES, C. & LOZANO, F. 2005. The lymphocyte receptor CD6 interacts with syntenin-1, a scaffolding protein containing PDZ domains. *Journal of Immunology,* 175**,** 1406-1414.

GRAKOUI, A., BROMLEY, S. K., SUMEN, C., DAVIS, M. M., SHAW, A. S., ALLEN, P. M. & DUSTIN, M. L. 1999. The immunological synapse: A molecular machine controlling T cell activation. *Science,* 285**,** 221-227.

GRIFFITHS, G. M., TSUN, A. & STINCHCOMBE, J. C. 2010. The immunological synapse: a focal point for endocytosis and exocytosis. *Journal of Cell Biology,* 189**,** 397-406.

GROVES, J. T. & DUSTIN, M. L. 2003. Supported planar bilayers in studies on immune cell adhesion and communication. *Journal of Immunological Methods,* 278**,** 19-32.

HASSAN, N. J., SIMMONDS, S. J., CLARKSON, N. G., HANRAHAN, S., PUKLAVEC, M. J., BOMB, M., BARCLAY, A. N. & BROWN, M. H. 2006. CD6 Regulates T-Cell Responses through Activation-Dependent Recruitment of the Positive Regulator SLP-76. *Mol. Cell. Biol.,* 26**,** 6727-6738.

HOOK, A. L., VOELCKER, N. H. & THISSEN, H. 2009. Patterned and switchable surfaces for biomolecular manipulation. *Acta Biomaterialia,* 5**,** 2350-2370.

HUPPA, J. B. & DAVIS, M. M. 2003. T-cell-antigen recognition and the immunological synapse. *Nature Reviews Immunology,* 3**,** 973-983.

JAISWAL, J. K. & SIMON, S. M. 2007. Imaging single events at the cell membrane. *Nature Chemical Biology,* 3**,** 92-98.

JANEWAY JR., C. A., TRAVERS, P., WALPORT, M. & SHLOMCHIK, M. J. 2005. *Immunobiology*, Garland Science Publishing.

JARES-ERIJMAN, E. A. & JOVIN, T. M. 2006. Imaging molecular interactions in living cells by FRET microscopy. *Current Opinion in Chemical Biology,* 10**,** 409-416.

KAIZUKA, Y., DOUGLASS, A. D., VARDHANA, S., DUSTIN, M. L. & VALE, R. D. 2009. The coreceptor CD2 uses plasma membrane microdomains to transduce signals in T cells. *J Cell Biol*.

KAIZUKA, Y., DOUGLASS, A. D., VARMA, R., DUSTIN, M. L. & VALE, R. D. 2007. Mechanisms for segregating T cell receptor and adhesion molecules during immunological synapse formation in Jurkat T cells. *Proc Natl Acad Sci U S A,* 104**,** 20296-301.

KOBARG, J., WHITNEY, G. S., PALMER, D., ARUFFO, A. & BOWEN, M. A. 1997. Analysis of the tyrosine phosphorylation and calcium fluxing of human CD6 isoforms with different cytoplasmatic domains. *European Journal of Immunology,* 27**,** 2971-2980.

KYOUNG, M., KARUNWI, K. & SHEETS, E. D. 2007. A versatile multimode microscope to probe and manipulate nanoparticles and biomolecules. *J Microsc,* 225**,** 137-46.

LIDKE, D. S. & WILSON, B. S. 2009. Caught in the act: quantifying protein behaviour in living cells. *Trends in Cell Biology,* 19**,** 566-574.

LIN, J., MILLER, M. J. & SHAW, A. S. 2005. The c-SMAC: sorting it all out (or in). *Journal of Cell Biology,* 170**,** 177-182.

LODISH, H., BERK, A., ZIPURSKY, S. L., MATSUDAIRA, P., BALTIMORE, D. & DARNELL, J. 2000. *Molecular cell biology,* New York, W.H. Freemand and Company.

MASHANOV, G. I., TACON, D., KNIGHT, A. E., PECKHAM, M. & MOLLOY, J. E. 2003. Visualizing single molecules inside living cells using total internal reflection fluorescence microscopy. *Methods,* 29**,** 142-152.

MAVRAKIS, M., RIKHY, R. & LIPPINCOTT-SCHWARTZ, J. 2009. Plasma Membrane Polarity and Compartmentalization Are Established before Cellularization in the Fly Embryo. *Developmental Cell,* 16**,** 93-104.

MCNERNEY, G. P., HUBNER, W., CHEN, B. K. & HUSER, T. 2010. Manipulating CD4(+) T cells by optical tweezers for the initiation of cell-cell transfer of HIV-1. *Journal of Biophotonics,* 3**,** 216-223.

MOSSMAN, K. D., CAMPI, G., GROVES, J. T. & DUSTIN, M. L. 2005. Altered TCR signaling from geometrically repatterned immunological synapses. *Science,* 310**,** 1191-1193.

MURADE, C. U., SUBRAMANIAM, V., OTTO, C. & BENNINK, M. L. 2009. Interaction of Oxazole Yellow Dyes with DNA Studied with Hybrid Optical Tweezers and Fluorescence Microscopy. *Biophysical Journal,* 97**,** 835-843.

NAVRATIL, M., MABBOTT, G. A. & ARRIAGA, E. A. 2006. Chemical microscopy applied to biological systems. *Anal Chem,* 78**,** 4005-20.

NELISSEN, J. M. D. T., PETERS, I. M., DE GROOTH, B. G., VAN KOOYK, Y. & FIGDOR, C. G. 2000. Dynamic regulation of activated leukocyte cell adhesion molecule-mediated homotypic cell adhesion through the actin cytoskeleton. *Molecular Biology of the Cell,* 11**,** 2057-2068.

ODDOS, S., DUNSBY, C., PURBHOO, M. A., CHAUVEAU, A., OWEN, D. M., NEIL, M. A. A., DAVIS, D. M. & FRENCH, P. M. W. 2008. High-Speed High-Resolution Imaging of Intercellular Immune Synapses Using Optical Tweezers. *Biophysical Journal,* 95**,** L66-L68.

OWEN, D. M., WILLIAMSON, D., RENTERO, C. & GAUS, K. 2009. Quantitative Microscopy: Protein Dynamics and Membrane Organisation. *Traffic,* 10**,** 962-971.

RAMSER, K. & HANSTORP, D. 2010. Optical manipulation for single-cell studies. *Journal of Biophotonics,* 3**,** 187-206.

REITS, E. A. J. & NEEFJES, J. J. 2001. From fixed to FRAP: measuring protein mobility and activity in living cells. *Nature Cell Biology,* 3**,** E145-E147.

SHEETZ, M. P. (ed.) 1998. *Laser Tweezers in Cell Biology,* San Diego: Academic Press.

SVOBODA, K. & BLOCK, S. M. 1994. Biological Applications of Optical Forces. *Annual Review of Biophysics and Biomolecular Structure,* 23**,** 247-285.

SWART, G. W. M. 2002. Activated leukocyte cell adhesion molecule (CD166/ALCAM): Developmental and mechanistic aspects of cell clustering and cell migration. *European Journal Of Cell Biology,* 81**,** 313-321.

SWART, G. W. M., LUNTER, P. C., VAN KILSDONK, J. W. J. & VAN KEMPEN, L. 2005. Activated leukocyte cell adhesion molecule (ALCAM/CD166): Signaling at the divide of melanoma cell clustering and cell migration? *Cancer And Metastasis Reviews,* 24**,** 223-236.

TE RIET, J., ZIMMERMAN, A. W., CAMBI, A., JOOSTEN, B., SPELLER, S., TORENSMA, R., VAN LEEUWEN, F. N., FIGDOR, C. G. & DE LANGE, F. 2007. Distinct kinetic and mechanical properties govern ALCAM-mediated interactions as shown by single-molecule force spectroscopy. *J Cell Sci,* 120**,** 3965-3976.

TOOMRE, D. & MANSTEIN, D. J. 2001. Lighting up the cell surface with evanescent wave microscopy. *Trends in Cell Biology,* 11**,** 298.

TREANOR, B. & BATISTA, F. D. 2007. Mechanistic insight into lymphocyte activation through quantitative imaging and theoretical modelling. *Current Opinion in Immunology,* 19**,** 476.

TSIEN, R. Y. 2005. Building and breeding molecules to spy on cells and tumors. *FEBS Letters,* 579**,** 927.

VAN DER KROGT, G. N., OGINK, J., PONSIOEN, B. & JALINK, K. 2008. A comparison of donor-acceptor pairs for genetically encoded FRET sensors: application to the Epac cAMP sensor as an example. *PLoS One,* 3**,** e1916.

VAN KEMPEN, L., NELISSEN, J., DEGEN, W. G. J., TORENSMA, R., WEIDLE, U. H., BLOEMERS, H. P. J., FIGDOR, C. G. & SWART, G. W. M. 2001. Molecular basis for the hemophilic activated leukocyte cell adhesion molecule (ALCAM)-ALCAM interaction. *Journal Of Biological Chemistry,* 276**,** 25783-25790.

VAN MANEN, H.-J., VERKUIJLEN, P., WITTENDORP, P., SUBRAMANIAM, V., VAN DEN BERG, T. K., ROOS, D. & OTTO, C. 2008. Refractive Index Sensing of

Green Fluorescent Proteins in Living Cells Using Fluorescence Lifetime Imaging Microscopy. *Biophysical Journal,* 94**,** L67-L69.

VAN ZANTEN, T. S., CAMBI, A. & GARCIA-PARAJO, M. F. 2010. A nanometer scale optical view on the compartmentalization of cell membranes. *Biochimica et Biophysica Acta (BBA) - Biomembranes,* 1798**,** 777-787.

VARMA, R., CAMPI, G., YOKOSUKA, T., SAITO, T. & DUSTIN, M. L. 2006. T cell receptor-proximal signals are sustained in peripheral microclusters and terminated in the central supramolecular activation cluster. *Immunity,* 25**,** 117-27.

WEE, S. F., SCHIEVEN, G. L., KIRIHARA, J. M., TSU, T. T., LEDBETTER, J. A. & ARUFFO, A. 1993. Tyrosine Phosphorylation of Cd6 by Stimulation of Cd3 - Augmentation by the Cd4 and Cd2 Coreceptors. *Journal of Experimental Medicine,* 177**,** 219-223.

WESSELS, J. T., YAMAUCHI, K., HOFFMAN, R. M. & WOUTERS, F. S. 2010. Advances in Cellular, Subcellular, and Nanoscale Imaging In Vitro and In Vivo. *Cytometry Part A,* 77A**,** 667-676.

YAN, L., HUCK, W. T. S. & WHITESIDES, G. M. 2004. Self-Assembled Monolayers (SAMs) and Synthesis of Planar Micro- and Nanostructures. 44**,** 175 - 206.

ZIMMERMAN, A. W., JOOSTEN, B., TORENSMA, R., PARNES, J. R., VAN LEEUWEN, F. N. & FIGDOR, C. G. 2006. Long-term engagement of CD6 and ALCAM is essential for T-cell proliferation induced by dendritic cells. *Blood,* 107**,** 3212-20.

ZIMMERMAN, A. W., NELISSEN, J. M. D. T., VAN EMST-DE VRIES, S. E., WILLEMS, P. H. G. M., DE LANGE, F., COLLARD, J. G., VAN LEEUWEN, F. N. & FIGDOR, C. G. 2004. Cytoskeletal restraints regulate homotypic ALCAM-mediated adhesion through PKC alpha independently of Rho-like GTPases. *Journal of Cell Science,* 117**,** 2841-2852.

Chapter 2 –

Development of hybrid TIRF-OT imaging modality

To develop a hybrid TIRF-OT microscopy method, various design and technical aspects have to be considered. This chapter describes the requirements for the TIRF-OT microscope (section 2.1), followed by the theory on steerable optical tweezers (section 2.2) and on total internal reflection fluorescence microscopy (section 2.3). Section 2.4 presents the computer automation, followed by the total implementation of the hybrid TIRF-OT microscope (section 2.5). Finally, the flow cell design (section 2.6) and the data analysis method are discussed (section 2.7).

2.1 TIRF-OT design requirements

To study cell-substrate and cell-cell interactions with high spatial and temporal resolution, we have developed a microscope combining the high signal-to-background ratio of TIRF microscopy with the ability to control the onset and position of interaction by means of OT. In order to have a versatile combination, the following requirements have to be met, as depicted in Fig. 2.1:

1. The microscope should be able to measure fluorescent light of at least one cell with high sensitivity and spatial accuracy. This requires the pixel size on a highly sensitive CCD camera to be slightly smaller than the diffraction limit, and the total field of view (depicted by the dashed line in Fig. 2.1) to be larger than the diameter of a cell (~15 μm for a non-stretched cell). For a CCD camera of 512*512 pixels, this results in a field of view of ~ 50*50 μm.
2. The OT should be steerable in *x, y,* and *z*, independent of the focus of the objective, so that the focus of the objective can be positioned at the (expected) interaction site, while manipulating the trapped cell. In Fig. 2.1, the dashed line

is positioned at the focal plane of the objective and at the expected interaction site. The trapped cell in Fig. 2.1 is not yet in place.

3. The trapped cell should be able to move through the whole field of view (laterally) in order to position the trapped cell at the preferred interaction site. Furthermore, the trapped cell should be able to move axially at least a distance of twice the diameter of the cell away from the focal plane of the objective, so the trapped cell can be moved laterally without the chance of unwanted interactions with the corresponding cell adhered at the surface. This requirement is equivalent to a movement in x,y of $\pm$ 25 µm and in z of $\pm$ 50 µm. The accuracy in step size should be minimally 1 µm.
4. At the interaction site, at least two colours should be detected. This would

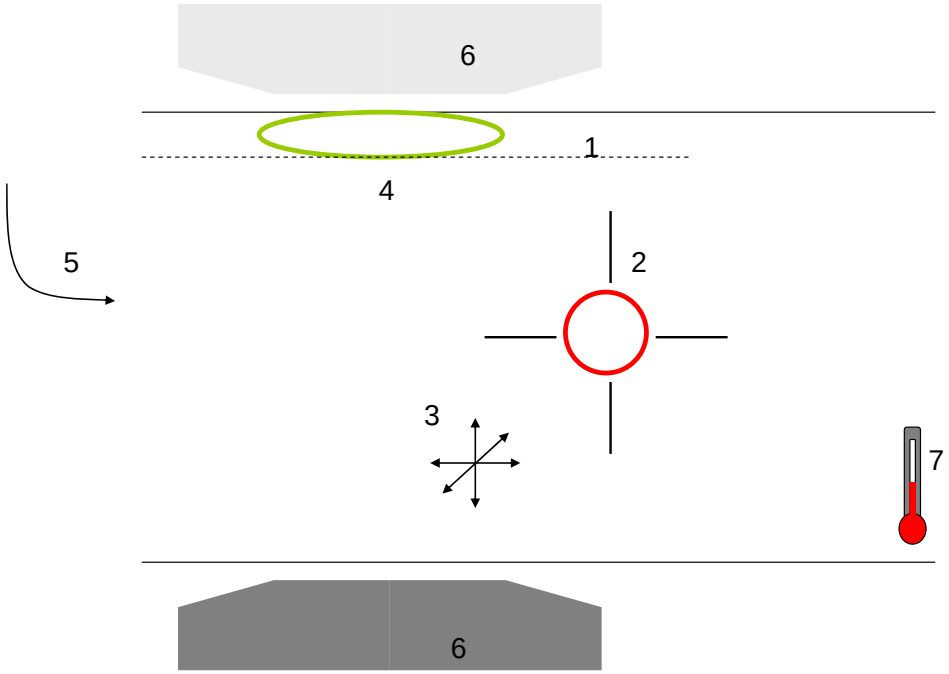

Fig. 2.1 Requirements hybrid TIRF-OT microscope
A green cell attached to a microscope slide and a red cell in the trap are depicted to explain the requirements for a combined TIRF-OT microscope (image not to scale). The dashed line depicts the field of view of the camera, positioned at the focal plane of the objective. The objective (6) can be positioned above or below the sample. The requirements are: a cell in the field of view should be detected with diffraction limited spatial sensitivity (1), the position of the OT should be steerable independent of the focal position of the objective (2), the trapped cell should be steerable in 3D (3), the microscope should detect dual colours (red and green cell, 4), new cells should be added to the sample (5), the objective should be used for OT and fluorescence detection (6) and the temperature in the sample should be 37 ºC (7).

enable the study of, for example, CD6 and ALCAM distributions simultaneous and independent of each other.

5. It should be possible to add (new) cells to the sample, so more experiments can be performed sequentially.
6. For practical reasons, the TIRF microscope objective should also be used for optical trapping.
7. It should be possible to perform the measurements at 37 ºC, to keep the cells vital and to not unduly influence cellular processes and membrane protein distribution dynamics.

2.2 Steerable optical tweezers

The principle of optical tweezers has been explained in section 1.4. To obtain a strongly focused beam in order to be able to trap a particle, in practice, it is required to (over)fill the back-aperture of a high NA objective (Svoboda and Block, 1994). High NA objectives can use water or oil immersion. However, oil immersion gives rise to higher spherical aberrations than water immersion (Lee et al., 2007), creating a less perfect focus (Hecht, 1987). Therefore, water immersion objectives are favourable for optical trapping.

We used two 4f-systems to create optical tweezers steerable with respect to the focus of the objective (see Fig. 2.2). The 4f-system composed by lenses L3 and L4 images the gimbal-mount mirror (GM) on the back-aperture (BA) of the objective (O), while overfilling the BA. Distances d_4, d_5, and d_6 are determined by the focal distances of lenses L3 and L4 (f_3 and f_4, respectively). Tilting GM with a small angle $\Delta\theta$ with respect to the nominal position (45 deg) results in a lateral displacement of the focus of the OT (Δxy), given by:

$$\Delta xy = -2 f_{EFL} \frac{f_3}{f_4} \Delta\theta \qquad \text{Eq. 2.1}$$

where f_{EFL} is the effective focal length of the objective, and $\Delta\theta$ given in radians.

The second 4f-system, composed by lenses L1 and L2 (with focal distances f_1 and f_2, respectively) is used to steer the trap in the axial direction, while maintaining an overfilled BA. A displacement Δl of lens L1 results in an axial displacement of the focus of Δz, given by (Fallman and Axner, 1997):

$$\Delta z = \left(\frac{f_{EFL}}{f_4}\right)^2 \left(\frac{f_3}{f_2}\right)^2 \Delta l \qquad \text{Eq. 2.2}$$

Considering the aforementioned requirements for Δz and Δxy, with f_4 determined by the tube lens of the microscope, a minimal step size of 1 μm, and the practical consideration that Δl should be maximally ~ 2 cm, a lens combination was chosen that meets the requirements. For convenience, the total magnification of the two 4f-systems ($\frac{f_2}{f_1}\frac{f_4}{f_3}$) is 1 and a beam expander determines the overfilling of

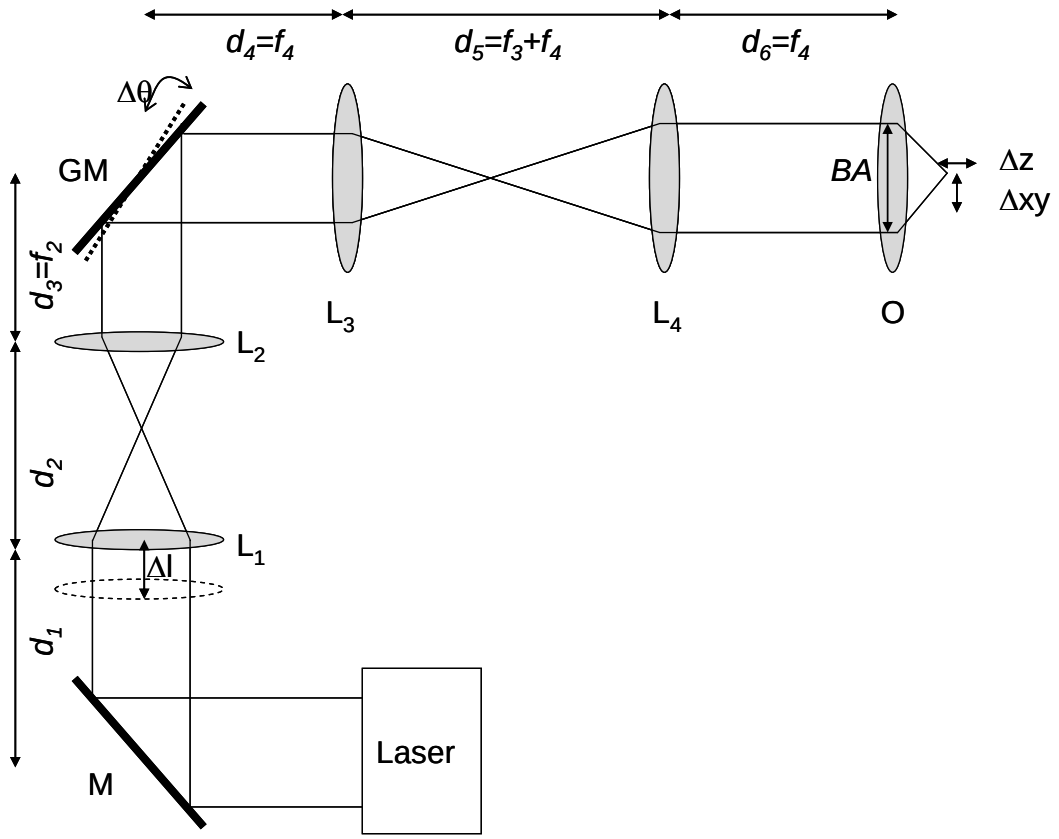

Fig. 2.2 4f-system for optical tweezers
Two 4f-systems composed of lens 1 (L1) and lens 2 (L2), and of lens 3 (L3) and lens 4 (L4). The distances between the components are given in focal distances (not drawn to scale). Gimbal-mount mirror (GM) is imaged at the back-aperture (BA) of the objective (O). When L1 is moved, the distance of the focus by the optical trap is changed with respect to the focal plane of the objective, while remaining the same overfilling of the BA. When GM is tilted, the focus of the laser light is still in the focal plane, but displaced in the lateral direction; the BA remains overfilled. Mirror M is used to direct the laser light.

the back-aperture of the objective (not depicted in Fig. 2.2).

2.3 TIRF microscopy design

2.3.1 TIRF configuration

Basically, two TIRF microscopy configurations are available: one using the objective both for excitation and detection, and the other using the objective only for detection and a prism for TIRF illumination (Fig. 2.3). In objective-based TIRF microscopy, a light beam enters the objective at an offset from the optical axis. In order to achieve an angle of incidence (θ_i) larger than the critical angle (θ_c), objective-based TIRF microscopy requires a high NA objective. In practise, this implies the use of an oil immersion objective with NA>1.4. However, variation of

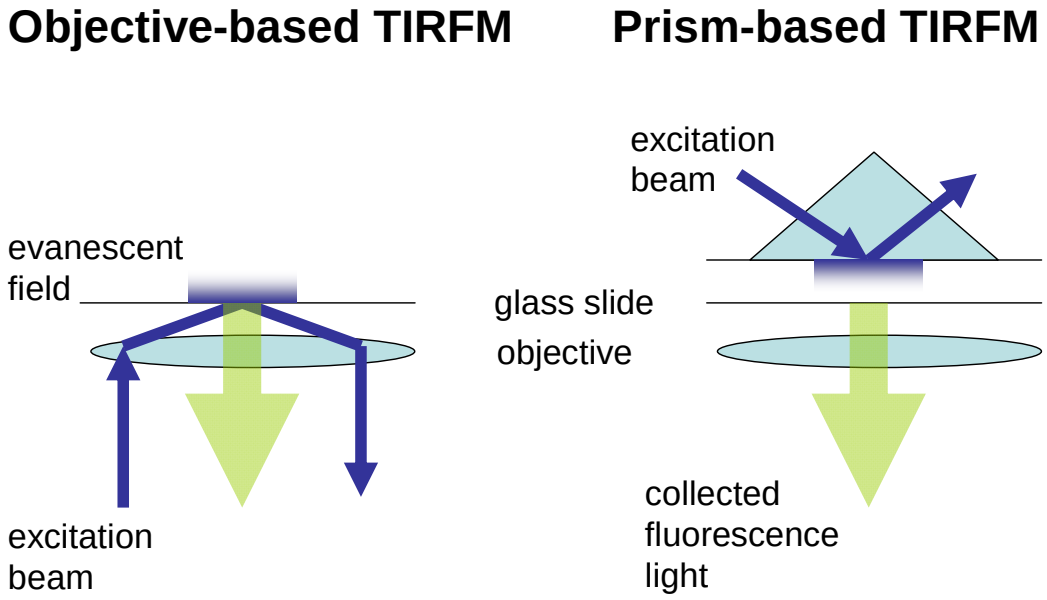

Fig. 2.3 Objective and prism-based TIRF microscopy
In objective TIRF microscopy (TIRFM), the excitation light is entering at the edge of the back aperture of the objective in order to direct the beam under a large angle to the glass slide. Oil is used for immersion between the objective and the glass slide, to prevent total internal reflection at the objective – immersion fluid transition. The objective is also used to collect the fluorescent light and image it on the camera.
In prism-based TIRF microscopy, the excitation light is directed through a high refractive index material (usually a type of glass) to create total internal reflection, for example by a prism as depicted in this figure. In this case, immersion oil is used between the prism and the glass slide, to prevent total internal reflection between the microscope slide and the prism. The fluorescent light is collected by an objective.

the angle of incidence to change the penetration depth is difficult in objective-based TIRF microscopy (Schneckenburger, 2005). In prism-based TIRF microscopy, the light is directed through a prism, hemisphere, trapezoid or a cube in order to obtain total internal reflection, and an objective is used to collect the fluorescent light. A drawback in this configuration can be the sample design and accessibility of the sample. When the prism is positioned on one side of the sample and the objective on the other side (see Fig. 2.3), the distance between the glass slides should be smaller than the working distance of the objective in order to be able to focus on the fluorescence excitation site. This requires a very thin sample. Furthermore, the accessibility by, for example, a pipet to add new cells is hampered. However, a prism-based TIRF microscopy is relatively inexpensive and the specific glass type of the prism used is for most applications not critical (Axelrod, 2001). Furthermore, the signal-to-background ratio is better than for objective TIRF microscopy (Ambrose et al., 1999). Considering requirement 6 (section 2.1) and the preference for a water immersion objective for optical tweezers implementation (section 2.2), we decided to use a water immersion 1.2 NA objective in combination with prism-based TIRF microscopy for the hybrid microscope.

2.3.2 CCD camera

Since the fluorescence intensity is usually low, the chosen detector is important. TIRF is a wide-field technique and as such a 2D imaging detector should be used. The most commonly used detector is a CCD (charged coupled device) camera. In low light conditions, the main challenge is to discriminate signal from background and noise. The noise sources can be divided in three types: read-out noise (which originates from the charge-to-voltage converter), dark noise (which is thermally induced noise from the camera in the absence of light), and shot noise, also called Poisson noise (which origins from the light itself and is the square root of the number of photons). The dark noise can be reduced by cooling the CCD chip of the camera. The read-out noise can be addressed by amplifying the signal, so the signal is larger than the noise level (Andor, 2008). Two camera types that can amplify the signal, and are used in this study, are the intensified CCD camera (ICCD) and the electron multiplying CCD camera (EMCCD). A disadvantage of ICCD cameras is the relatively low quantum efficiency (QE) of the photocathode

(<50%). Alternatively, EMCCD cameras were used, which a have high QE (>90 %, (Andor, 2008)).

2.3.3 Dual colour detection

Requirement 4 (section 2.1) stated that we would like to measure at least two membrane proteins independently, requiring a dual colour system. Three general schemes for multicolour detection are available: sequential imaging of all fluorescence signals on one camera (1), parallel imaging of the fluorescence signals at different regions on the same camera (2), and parallel imaging of the fluorescence signals at different cameras (3). When the fluorescence distribution of high dynamic processes is studied, the first option requires a fast camera. Only with a fast camera can the distribution in one colour channel be related to the distribution in the other colour channel (measured at a later time), without spatial dislocation due to protein dynamics. The second option has two main disadvantages: chromatic aberration interferes with focussing both wavelengths on the same camera, and a possible loss in resolution since only one half of the CCD chip can be used per colour. The third option, albeit more expensive since it requires two cameras, provides a solution for all three disadvantages mentioned: chromatic aberration, loss in resolution and time correlation between the fluorescence signals of different colours and is, therefore, implemented for dual colour experiments.

Preferably, the two cameras used for dual colour detection each detect only the fluorescence of one type of fluorophore. Therefore, the filters in the detection path have to match the measured fluorophores, which preferably have distinct, separated emission spectra. If a camera detects a mix of the fluorescence of both fluorophores, we speak about crosstalk. This crosstalk can be addressed based on theory. When a number of fluorophores ($n_{molecules}$) in the detection volume are excited with a wavelength λ and the excitation intensity (I_{ex}^{λ}) and excitation efficiency of the fluorophore (Φ_{ex}^{λ}) are known, the measured intensity on the camera for that fluorophore can be given by:

$$I = n_{molecules} \cdot I_{ex}^{\lambda} \Phi_{ex}^{\lambda} \int Em(\lambda) \cdot F(\lambda) \cdot d\lambda \qquad \text{Eq. 2.3}$$

where $Em(\lambda)$ is the emission spectrum of the fluorophore, $F(\lambda)$ gives the composite spectral throughput of all filter spectra in the optical path. Using the spectra for the filters in our TIRF microscopy setup, and the known excitation and emission spectra of enhanced GFP and monomeric RFP (mRFP), the fluorescent light recorded from both fluorophores can be calculated per camera (Appendix 2A). This calculation revealed that the excitation efficiency of mRFP for 488 nm illumination is low, and that the amount of GFP fluorescent light detected by camera 2 (detecting the higher wavelengths, called the red camera), as well as the amount of mRFP detected by the camera 1 (detecting the lower wavelengths, called the green camera) is low. However, crosstalk is still possible, and the exact amount of crosstalk will depend on $n_{molecules}$. To separate the fluorophore contributions from each other, Eq. 2.4 can be used:

$$I_{GFP}^{green} = \frac{I^{green} - \beta I^{red}}{1-\alpha\beta} \quad \text{and} \quad I_{RFP}^{red} = \frac{I^{red} - \alpha I^{green}}{1-\alpha\beta} \qquad \text{Eq. 2.4}$$

where α and β are determined by the calculations (Appendix 2A) and depend on the excitation intensities, excitation efficiencies and whether imaging is performed simultaneously or sequentially, I_{GFP}^{green} is the intensity image of only GFP fluorescence detected by the green camera, I^{green} is the recorded image by the green camera, and I_{RFP}^{red} and I^{red} are defined similarly. However, α and β are independent of $n_{molecules}$, and I^{green} and I^{red} can be corrected for differences in sensitivity between both camera (Appendix 2A).

2.4 Computer control

In order to control the position of the OT, a LabVIEW (National Instruments) VI was written. Both the scanning mirror and the scanning lens are moved by motorized linear translation stages. The scanning mirror has two actuators, enabling tilting in two dimensions and, therefore, movement in *x* and *y*. All actuators are stepper motor driven by a MotionMaster2000 controller (Newport, Irvine, CA) connected to the computer. In the LabVIEW VI, the step size and the home position (*x,y,z*=0,0,0) of the trap can be set.

Furthermore, an executable file was written in Visual Basic (Microsoft), to control the image acquisition for the ICCD camera. The executable file controlled the delay time between the images and saved the experimental settings in the recorded image (stack) file.

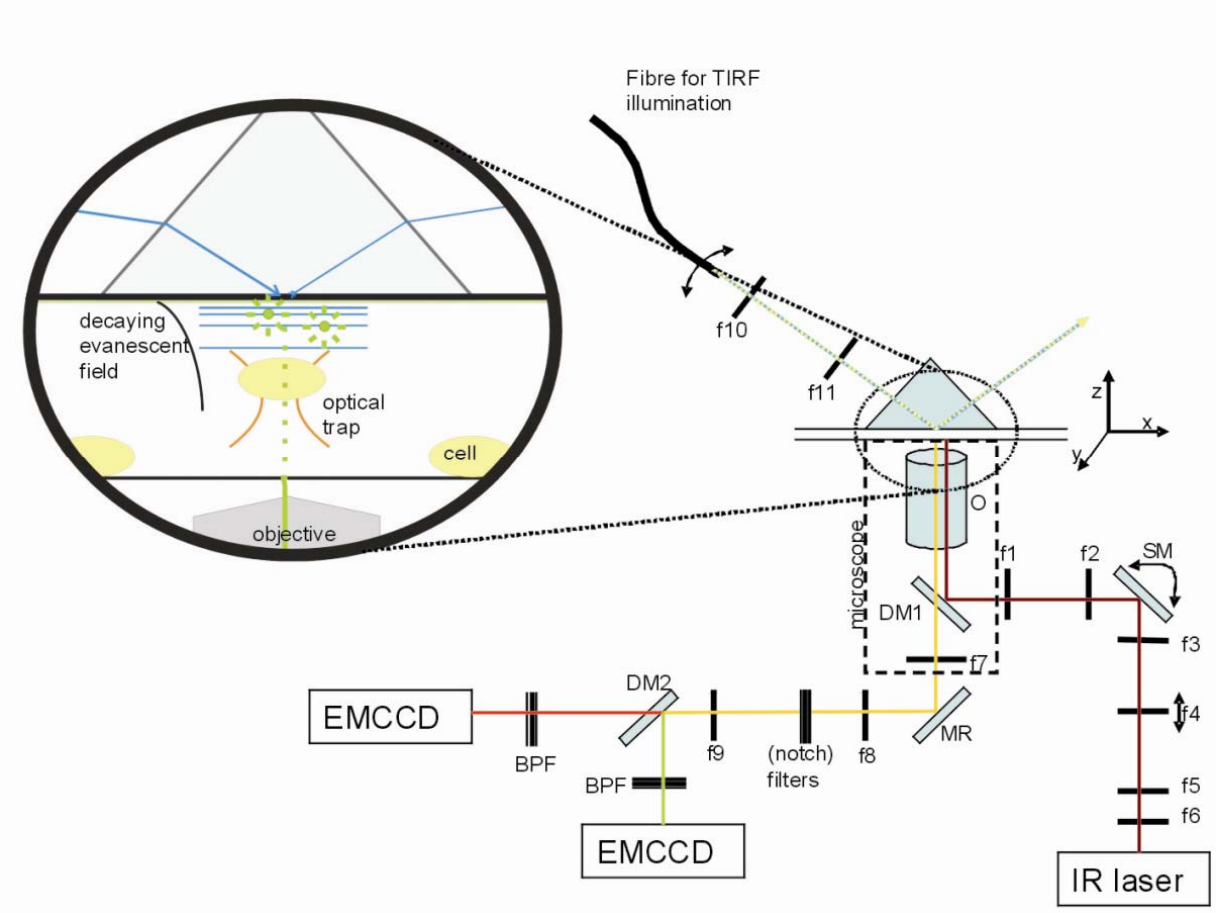

Fig. 2.4 Schematic drawing of hybrid TIRF-OT microscope implementation
Combined TIRF-OT setup (image not to scale): In the optical tweezers pathway (dark red) f1 (*f* = 160 mm), f2 (*f* = 120 mm), f3 (*f* = 30 mm) and f4 (*f* = 40 mm) are a 4 lens system with a scanning mirror (SM) and a movable lens (f4) to direct the laser beam; f5 and f6 form a beam expander (*f* = 100 resp. -10 mm). The infrared light enters the microscope through the epi port of the microscope. DM1 (short pass 700 nm) reflects the infra red light of the optical tweezers, but transmits all other wavelengths. The light is focused by objective O. The laser light for TIRF illumination is coming through a fibre. The arm for TIRF illumination with the fibre, f10 (*f* = 10) and f11 (*f* = 160) is movable, to change the angle of incidence; the light is directed on a glass prism (*n* = 1.52). The focal length of f8 and f7 is 160 mm. In the detection path (yellow) a dichroic mirror (DM2, longpass 560) was positioned after implementation of dual colour detection. Before the cameras, a band pass filter (BPF 525/50, 514/30 or 593/40) was positioned, matching the emission wavelength of the fluorophore. A short pass filter (SPF 700 nm) is used to block remaining IR light. Lens f9 (*f* = 300 mm) is used to image the light on the intensified CCD camera.

2.5 TIRF-OT implementation

Fig. 2.4 shows a schematic of the constructed dual colour setup. The prism-based TIRF is constructed on a Zeiss Axiovert 135 TV microscope (Oberkochen, Germany), positioned on an optical table (Newport). 488 nm and 568 nm laser light from an Ar and ArKr laser (Coherent Inc., Santa Clara, CA) is guided to the setup by an optical fibre with two entrances and one exit. A shutter is positioned in front of the fibre input (controlled by the CCD camera) to block illumination when no images are acquired, in order to minimize photobleaching. A water immersion objective (Leica 100x, NA 1.2, Wetzlar, Germany) is used to collect the fluorescence from the sample and to generate an optical trap. The microscope was equipped with a heated stage and the objective was equipped with a heater ring (PeCon, Germany) to set the experimental temperature to ~ 37 ºC (requirement 7, section 2.1). Fluorescence images presented in chapter 3 are recorded with an image intensified CCD camera (Pentamax 512FT, Roper Scientific, Trenton, NJ), using WinSpec/32 (Roper Scientific). Fluorescence images presented in chapters 4 and 5 are recorded with an EMCCD camera (Ixon+, Andor), using Andor Solis software.

An infrared (wavelength: 1064 nm) solid-state laser (Millennia IR, SpectraPhysics – Newport, Mountain View, CA) is used for optical trapping. A scanning mirror is used to steer the position of the trap in the x-y plane, whereas a moveable lens is used to position the trap in the z-direction; both are stepper motor driven by the MotionMaster2000 (Newport) and controlled by Labview software (National Instruments, Austin, Texas). Dichroic mirrors and filters are used to direct only the desired wavelengths to the specific parts of the setup. For the single colour experiments of chapter 3, no DM2 was implemented.

Fig. 2.5 shows a photograph of the hybrid TIRF-OT microscope, built on an optical table. At the back of the microscope, the OT part is situated, which is shown in close-up in the inset photograph.

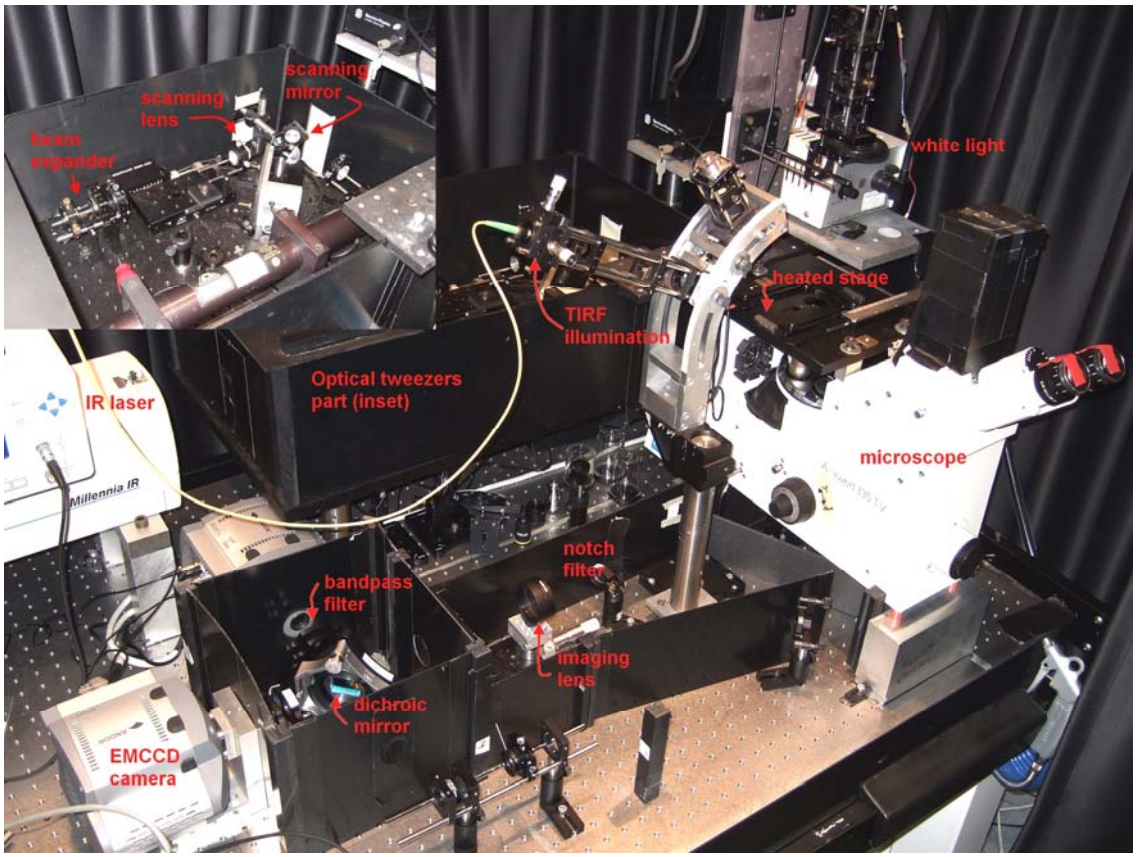

Fig. 2.5 TIRF-OT implementation Photograph of optical table on which the hybrid TIRF-OT microscope is built, inset contains close-up photo of OT part

2.6 Flow cell design

2.6.1 Requirements

The setup developed in this thesis combines prism-based TIRF microscopy with optical tweezers. The prism is positioned on one side of the sample, whereas the objective used for imaging and trapping is positioned at the other side of the sample. Therefore, the sample requires glass on two sides of the medium including the cells (Fig. 2.6a). When no spacer is used between the glass slides, the medium between the slides will evaporate and the distance between the glass slides will change continuously. That would cause the interaction site to move out of focus. Therefore, a flowcell with a spacer is needed. This section describes the development and final design of the flowcells used in this thesis.

The main requirements for the flowcell are:

1. After preparing the flowcell, it should be possible to add (new) cells in the flowcell.
2. The thickness of the flowcell should be such that it enables visualisation of the TIRF-excitation side of the sample. The objective (100x, 1.2 NA, Wetzlar, Germany) has a maximum working distance of ~70-100 μm, using coverglasses of thickness 1,5 (that is, 170 μm).
3. The prism for TIRF illumination should be positioned on the flowcell. The top material should be optically flat and have a refractive index larger than

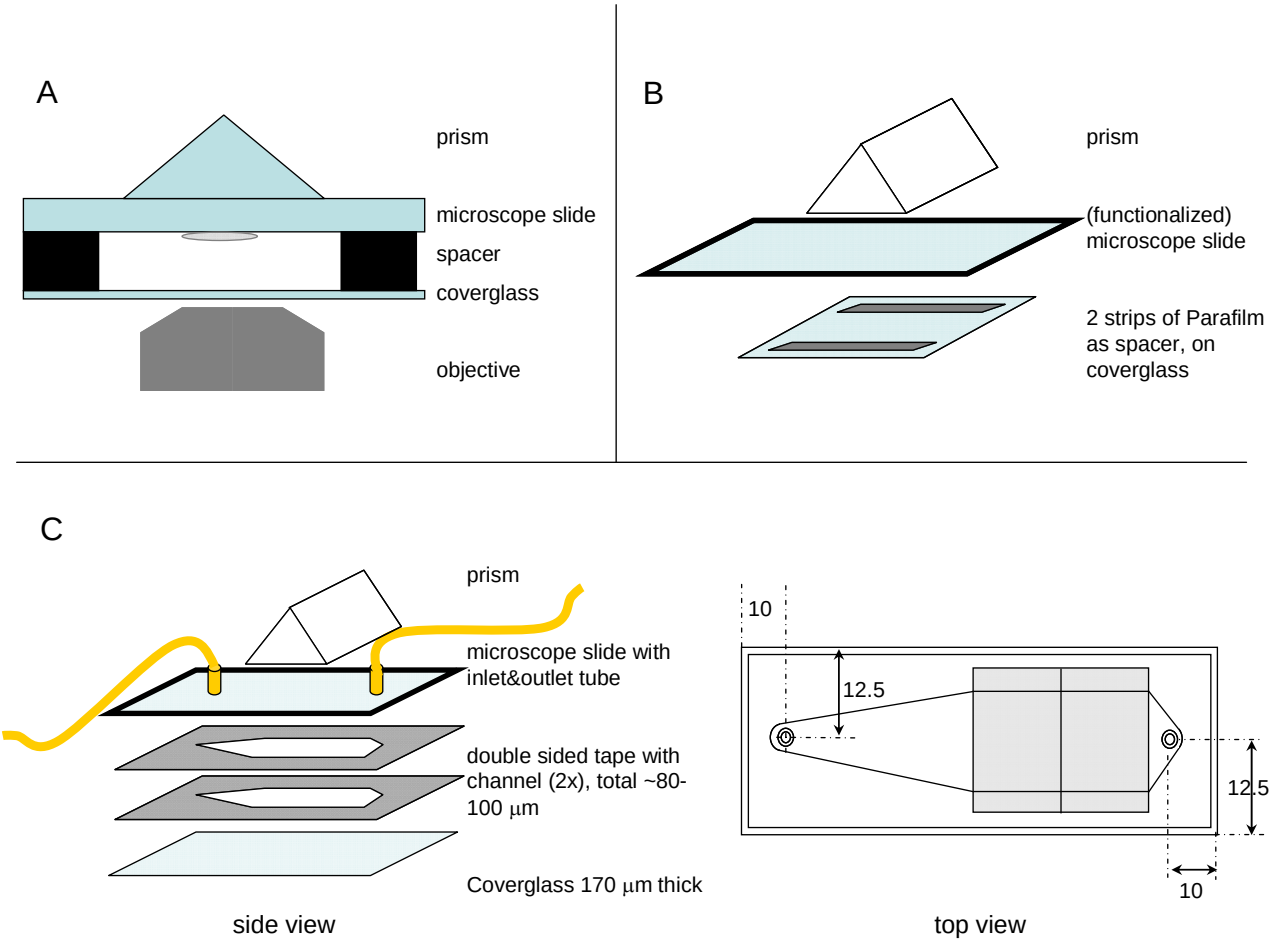

Fig. 2.6 Flowcell design
Schematic drawings of the flowcell (not to scale, except top view in C). A. The general flowcell design incorporates a microscope glass to which a cell is attached, a coverglass and a spacer. The prism is positioned on top of the flow cell, while the objective studies the cell from below. B. Side view of flowcell 1, using two stripes of Parafilm as a spacer, creating a channel for the cells. C. Side view and top view of flowcell 2 with double sided tape a spacer, cut into shape to create a channel (sizes in the top view). An inlet and an outlet tube are glued to the microscope slide. The gray part in the top view gives the size and position of the prism.

that of water and cells (~1.33-1.38), to enable TIRF illumination. The top side of the flowcell should be large enough (prism basal area is 2x1.5 cm), and stable enough so the glass is not bent by the mass of the prism.

4. The laser beam for TIRF excitation should not be disturbed by the walls, tubes etc. of the flowcell.

2.6.2 Design of flowcell 1

The first design for a flowcell is depicted in Fig. 2.6b; a microscope glass and a coverglass are separated with two lines of Parafilm M (Alcam Packaging, Neenah, WI) with an opening between them where the medium (+ cells) can be flown in. The microscope glass (26*76*10 mm) used as the top glass slide stabilizes the flowcell and prevents bending of the flowcell. Before fabrication of the flowcell, the microscope glass can be functionalized. Then, the Parafilm and the coverglass are positioned and the flowcell is heated (> 60 ˚C) shortly, so the Parafilm melts and holds the glasses together. After the first inflow of medium (by capillary forces, when a droplet is positioned next to the channel), new medium can be flown in by adding a new droplet and using a tissue at the other side of the channel to aspire out the old medium. This type of flowcell is used in the experiments of chapter 3.

The disadvantage of this method is two-fold. First, the heating of the Parafilm makes the method impossible to use when the microscope glass is pre-incubated with cells, because they will not survive the heating step. Second, the inflow of new medium is impractical. The first problem can be tackled by using (thin) double sided tape; however, the second problem requires an alternative flowcell.

2.6.3 Design of flowcell 2 with inlet and outlet

This section describes the design of a flowcell with inlet and outlet for optimal inflow of new cells (first requirement, section 2.6.1). This flowcell 2 uses double sided tape (3M, 467 MP tape, thickness 0.06 mm, according to the manufacturer) as a spacer. The inlet and outlet should not hinder the illumination (fourth requirement, section 2.6.1). Therefore, a small inlet tube was positioned far from the prism, through a hole in the microscope slide. The outlet tube was larger and positioned at the other side of the prism. Furthermore, the area available for

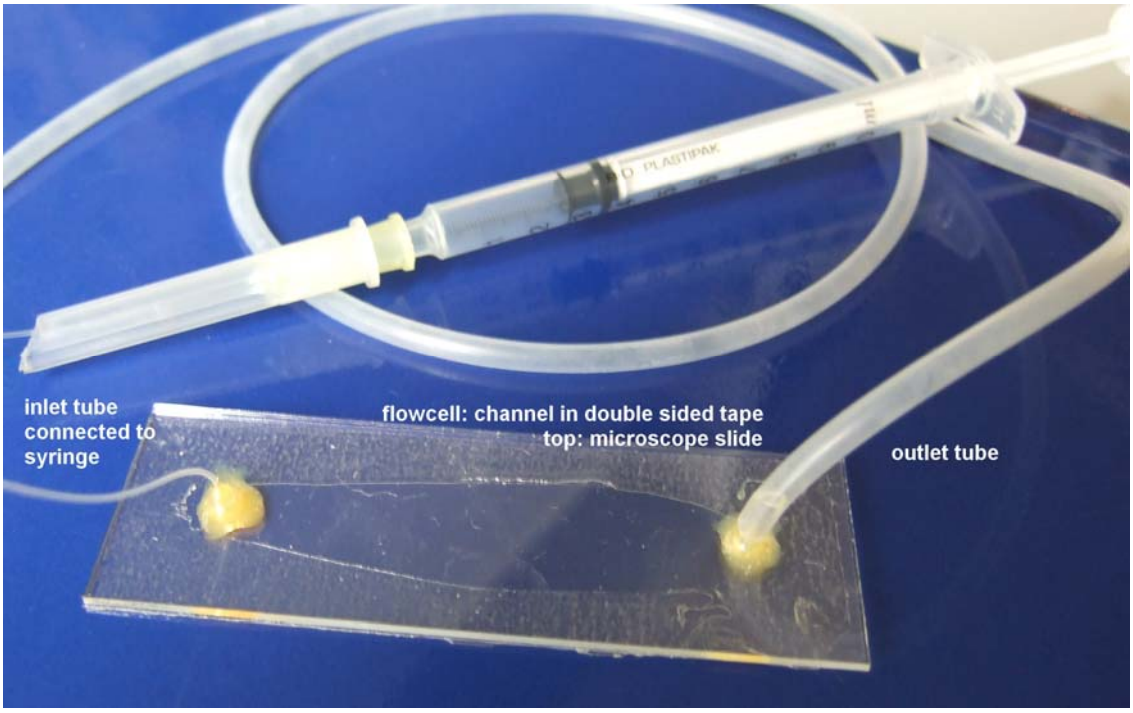

Fig. 2.7 Photograph of flowcell 2 with inlet and outlet Double sided tape with a channel is sandwiched between a cover glass and a microscope glass. Via a syringe cells and medium can be flown in the channel.

cell-cell or cell-substrate interactions had to be as large as possible. Altogether, this let to the design depicted in Fig. 2.6c, with tape widths of at least 5 mm and two layers of tape used to make the flowcell. For functionalization of the microscope slide with either proteins or cells, one layer of tape is positioned, a hydrophobic barrier is drawn, and, within that area, the glass is functionalized. The second layer of tape is placed on the coverglass, and when the excess of medium is removed from the microscope glass, the tape layers can be positioned on top of each other with undisturbed adhesiveness and no influence on cell viability. Fig. 2.7 gives a photograph of this type of flowcells, where the various parts are indicated in the picture.

2.7 Data analysis

2.7.1 Isodata thresholding – theory

The analysis of the collected fluorescence intensity images was performed in DIPimage (Delft University of Technology, The Netherlands, www.diplib.org), a scientific image processing toolbox for Matlab (The MathWorks, Natick, MA),

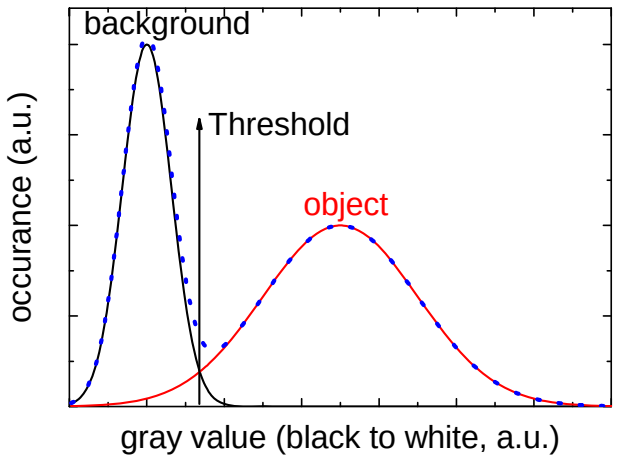

Fig. 2.8 Isodata thresholding
A histogram of all the intensities in a fictive image (blue dotted line). The histogram is composed of two intensity distributions, the image (red) and background (black). The threshold is determined by isodata thresholding, and depicted by the black arrow.

unless stated otherwise. To perform automatic data analysis on the acquired images, an important step is the discrimination of the fluorescence signal from the background. Segmentation of the image in background and signal (specifically: ALCAM-GFP or CD6-RFP fluorescence) is performed by isodata thresholding (Ridler and Calvard, 1978) after appropriated preprocessing, for example noise reduction filtering. This isodata thresholding method assumes a bimodal intensity distribution with two means, and calculates the threshold in an iterative process (DIPimage, 2010). Fig. 2.8 shows a (fictive) intensity distribution (blue dotted line) of an image. The position of the determined threshold is shown by the black arrow, assuming two normal distributions (black line for background and red line for signal).

2.7.2 Data analysis – measures

After segmentation of the fluorescence image, (statistical) analysis is performed on the determined cell body (pixel intensity > threshold value). We calculated the size of the cell body (also called contact size and size of the contact site), and the mean and maximum pixel intensity within the cell body, using a built in measure function in DIPimage. The contact size was determined by counting all pixels with an intensity above the threshold value and converting this number into μm^2 using the pixel calibration of the system.

Furthermore, we tested several measures for the homogeneity of the cell body. For this, we performed a second isodata thresholding within the cell body, to

determine whether high intensity spots were present (above the on average lower intensity average fluorescence of the cell body). We used the number of spots divided by the contact size as a measure for the homogeneity. Again, it should be noted that the isodata thresholding will find spots, even in a fully homogenous cell body. The correctness of measures based on the second thresholding (to find the spots) should, therefore, always be manually validated.

2.7.3 Image overlap in dual colour experiments

In our dual colour experiments, images are collected by two cameras. Even after careful alignment of the cameras, locations on the sample do not coincide in the image coordinates on both cameras. The images are slightly rotated and shifted with respect to each other, and the magnification is also slightly different. This can be accounted for by processing the images offline. To accomplish this, we imaged a test slide with many 100 nm fluorescent beads detected onto both cameras. These images have many high intensity points that colocalize in the sample plane. We set the image of camera 1 as the reference. Then, we determined a rough value for the zoom, shift and rotation in order to translate the image on camera 2 to overlap the high intensity spot distribution on camera 1, using the DIPimage function *fmmatch*. Afterwards, the DIPimage function *find_affine_trans* was used to fine tune the determined magnification, shift and rotation values. Finally, the determined values were stored and used to translate all images obtained by the camera 2 by matrix transformation (with *affine_trans*) to overlap with the images obtained by camera 1. These translated images were saved and used afterwards in the analysis and colocalisation studies.

References

AMBROSE, W. P., GOODWIN, P. M. & NOLAN, J. P. 1999. Single-molecule detection with total internal reflection excitation: Comparing signal-to-background and total signals in different geometries. *Cytometry,* 36**,** 224-231.

ANDOR 2008. Andor Catalog - Digital Camera Fundamentals.

AXELROD, D. 2001. Total Internal Reflection Fluorescence Microscopy in Cell Biology. *Traffic,* 2**,** 764-774.

DIPIMAGE. 2010. *Image Processing Fundamentals - Segmentation: http://www.ph.tn.tudelft.nl/Courses/FIP/frames/fip-Segmenta.html* [Online]. [Accessed 2010].

FALLMAN, E. & AXNER, O. 1997. Design for fully steerable dual-trap optical tweezers. *Applied Optics,* 36**,** 2107-2113.

HECHT, E. 1987. *Optics* Reading, MA, Addison-Wesley Publishing Company.

LEE, W. M., REECE, P. J., MARCHINGTON, R. F., METZGER, N. K. & DHOLAKIA, K. 2007. Construction and calibration of an optical trap on a fluorescence optical microscope. *Nat Protoc,* 2**,** 3226-38.

RIDLER, T. W. & CALVARD, S. 1978. Picture Thresholding Using an Iterative Selection Method. *Ieee Transactions on Systems Man and Cybernetics,* 8**,** 630-632.

SCHNECKENBURGER, H. 2005. Total internal reflection fluorescence microscopy: technical innovations and novel applications. *Curr Opin Biotechnol,* 16**,** 13-8.

SHANER, N. C., CAMPBELL, R. E., STEINBACH, P. A., GIEPMANS, B. N. G., PALMER, A. E. & TSIEN, R. Y. 2004. Improved monomeric red, orange and yellow fluorescent proteins derived from Discosoma sp. red fluorescent protein. *Nat Biotech,* 22**,** 1567-1572.

SVOBODA, K. & BLOCK, S. M. 1994. Biological Applications of Optical Forces. *Annual Review of Biophysics and Biomolecular Structure,* 23**,** 247-285.

TSIEN, R. Y. *Tsien Lab Website - Ref. fluorophore spectra* [Online]. [Accessed 2010].

Appendix 2A. Crosstalk - theory

When a number of fluorophores ($n_{molecules}$) in the detection volume are excited with a wavelength λ and the excitation intensity (I_{ex}^{λ}) and excitation efficiency of the fluorophore (Φ_{ex}^{λ}) are known, the measured intensity on the camera for that fluorophore can be given by:

$$I = n_{molecules} \cdot I_{ex}^{\lambda} \Phi_{ex}^{\lambda} \int Em(\lambda) \cdot F(\lambda) \cdot d\lambda \qquad \text{Eq. 2A.1}$$

where $Em(\lambda)$ is the emission spectrum of the fluorophore, $F(\lambda)$ gives the multiplication of all transmission characteristics of all the filters in the optical path. Here, we define the excitation efficiency Φ_{ex}^{λ} based on the quantum yield (ϕ), the extinction coefficient (ε) and the wavelength dependent relative value in the peak normalized absorption spectrum of the fluorophore (A^{λ}): $\Phi_{ex}^{\lambda} = \varepsilon \phi A^{\lambda}$. During the calculations we assume that the camera detects all wavelengths with the same sensitivity. At the end of this appendix, this issue is addressed further.

Eq. 2A.1 can be adjusted to the specific situation of our TIRF microscopy setup, for example using enhanced GFP, 488 nm and 568 nm excitation wavelengths, a band pass filter (*BPF*) for the camera, a 560 nm dichroic mirror (*DM*) between the cameras and a notch filter $notch_{568}$. This gives

$$I_{GFP} = n_{GFP} \cdot I_{ex}^{\lambda} \cdot \Phi_{ex}^{\lambda} \int Em_{GFP} \cdot DM_{560} \cdot notch_{568} \cdot BPF_{camera} d\lambda \qquad \text{Eq. 2A.2}$$

where $I_{ex}^{\lambda} \cdot \Phi_{ex}^{\lambda}$ should be calculated for both excitation wavelengths; for simultaneous excitation by both wavelengths, the total effective excitation is $\left(I_{ex}\Phi_{ex}\right)^{total} = I_{ex}^{488} \cdot \Phi_{ex}^{488} + I_{ex}^{568} \cdot \Phi_{ex}^{468}$. Table 2A.1 shows the origin of the used spectra for the simulations and Table 2A.2 give the excitation efficiencies used. In the calculations based on Eq. 2A.2, the spectra of the fluorophores were multiplied with the spectra of the filters[23].

[2] For the camera detecting green fluorescence, the used reflection spectrum of the dichroic mirror is 1-transmission

Fig. 2A1 gives the normalized intensity of GFP and RFP as a function of the wavelength (solid line) and the calculated intensities which are collected by the two cameras (dashed and dotted line). The lower wavelengths are collected by camera 1 (green) and the higher wavelengths by camera 2 (red). Then, the area under the curves of Fig. 2A1 was integrated from λ=400 nm to λ=700 nm. The results are presented in Table 2A.3.

Table 2A.1 Origin spectra for crosstalk simulations

Variable	***Origin***
Spectrum Em_{GFP}	(Tsien)
Spectrum Em_{RFP}	Christian Blum (unpublished data)
Quantum yield and extinction coefficient	(Shaner et al., 2004)
Transmission filter spectra DM_{560}, $notch_{568}$, $BPF_{514/30}$ and $BPF_{593/40}$	Manufacturer (Semrock, Rochester, NY)

Table 2A.2 Excitation efficiency

Fluorophore	Φ_{488} $(M^{-1}cm^{-1})$	Φ_{568} $(M^{-1}cm^{-1})$
EGFP	$56x10^3*0.6*0.998=34\ x10^3$	$56\ x10^3*0.6*0.004=0.13\ x10^3$
mRFP	$50\ x10^3*0.25*0.29=3.6\ x10^3$	$50\ x10^3*0.25*0.77=9.6\ x10^3$

Table 2A.3 Integrated intensities curves Fig. 2A.1 λ=400-700 nm (solid, dashed and dotted lines respectively)

Fluorophore	*Total area (nm)*	*Green camera (nm)*	*Red camera (nm)*
EGFP	44	24.9 = C_{GFP}^{green}	1.67
mRFP	65.5	1.22	26.4

For optimal separation of the GFP and RFP fluorescence, the ratio between the RFP and GFP contributions on both cameras should be as low as possible, that is: $\frac{I_{GFP}^{red}}{I_{RFP}^{red}}$ and $\frac{I_{RFP}^{green}}{I_{GFP}^{green}}$<<1, where I_{GFP}^{red} is the integrated GFP fluorescence intensity on the red camera. However, these ratios depend on $n_{molecules}$, as can be seen in Eq. 2A.3:

[3] The spectra of the 488 nm notch filter and the 700 nm short pass filter were not incorporated in the calculations, since they did not contribute to a difference between the channels.

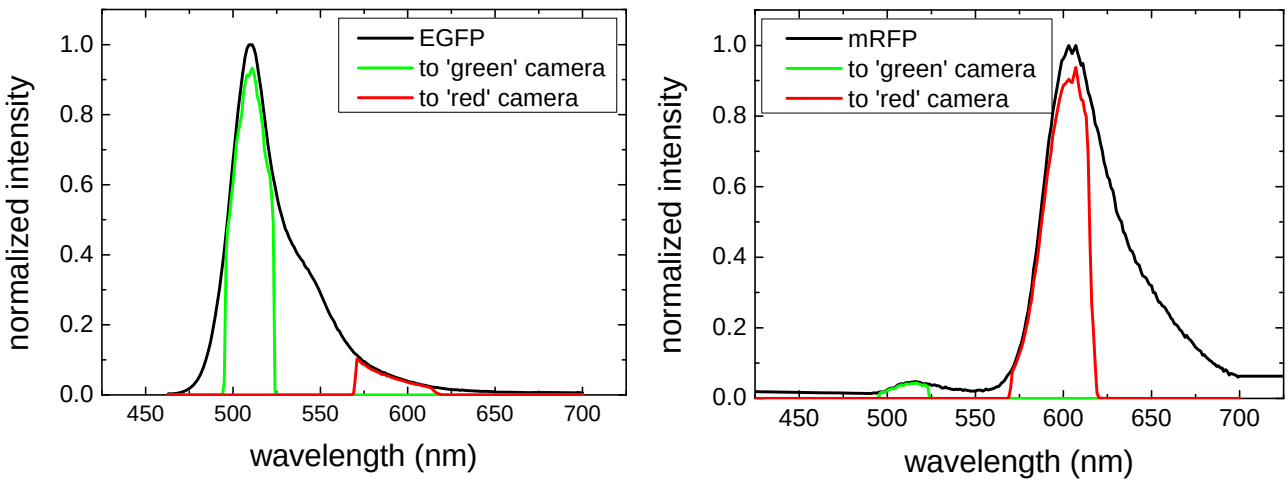

Fig. 2A1 – Normalized emission spectra of EGFP and mRFP and the fraction that is projected on the green camera (collecting light below 560 nm) and to the red camera (collecting light above 560 nm).

$$\frac{I_{GFP}^{red}}{I_{RFP}^{red}} = \frac{n_{GFP}}{n_{RFP}} \frac{C_{GFP}^{red}}{C_{RFP}^{red}} \cdot \frac{I_{ex}^{488}\Phi_{GFP}^{488} + I_{ex}^{568}\Phi_{GFP}^{568}}{I_{ex}^{488}\Phi_{RFP}^{488} + I_{ex}^{568}\Phi_{RFP}^{568}} \qquad \text{Eq. 2A.3a}$$

$$\frac{I_{RFP}^{green}}{I_{GFP}^{green}} = \frac{n_{RFP}}{n_{GFP}} \frac{C_{RFP}^{green}}{C_{GFP}^{green}} \cdot \frac{I_{ex}^{488}\Phi_{RFP}^{488}}{I_{ex}^{488}\Phi_{GFP}^{488}} \qquad \text{Eq. 2A.3b}$$

where C_{GFP}^{red} is the fraction of the GFP fluorescence light to the red camera (Table 2A.3).

Eq. 2A.3a assumes simultaneous illumination with 488 nm and 568 nm light for $\frac{I_{GFP}^{red}}{I_{RFP}^{red}}$. Eq. 2A.3b is slightly different because the Stokes shift requires that excitation with 568 nm does not result in emission below this wavelength, so 568 nm excitation is not considered for the green camera.

Since $\frac{n_{GFP}}{n_{RFP}}$ is unknown, $\frac{I_{GFP}^{red}}{I_{RFP}^{red}}$ and $\frac{I_{RFP}^{green}}{I_{GFP}^{green}}$ are difficult to determine, and further optimisation by calculations is therefore not useful. However, the crosstalk can be accounted for in the following way:

$$I^{green} = I_{GFP}^{green} + I_{RFP}^{green} = I_{GFP}^{green} + \beta I_{RFP}^{red} \qquad \text{Eq. 2A.4a}$$

$$I^{red} = I^{red}_{GFP} + I^{red}_{RFP} = \alpha I^{green}_{GFP} + I^{red}_{RFP} \qquad \text{Eq. 2A.4b}$$

where α and β indicate the fraction of the light detected by the 'unintended' camera, and for simultaneous, respectively, sequential illumination and detection, are independent of $n_{molecules}$:

$$\alpha_{sim} = \frac{C^{red}_{GFP}}{C^{green}_{GFP}} \frac{\Phi^{488}_{GFP} + \chi\Phi^{568}_{GFP}}{\Phi^{488}_{GFP}} \qquad \beta_{sim} = \frac{C^{green}_{RFP}}{C^{red}_{RFP}} \frac{\Phi^{488}_{RFP}}{\Phi^{488}_{RFP} + \chi\Phi^{568}_{RFP}}$$

$$\alpha_{seq} = \frac{C^{red}_{GFP}}{C^{green}_{GFP}} \frac{\chi\Phi^{568}_{GFP}}{\Phi^{488}_{GFP}} \qquad \beta_{seq} = \frac{C^{green}_{RFP}}{C^{red}_{RFP}} \frac{\Phi^{488}_{RFP}}{\chi\Phi^{568}_{RFP}}$$

where $\chi = I^{568}_{ex} / I^{488}_{ex}$, which is set before the experiment and can be estimated from the fibre output powers for both wavelengths, assuming a similar spot size, reflection behaviour on the optical components, and penetration depth. To give an impression of the size of α and β, Table 2A.4 gives the respective values of α and β, for various values of χ.

Table 2A.4 Possible values of α and β, for various values of χ

χ	α_{sim}	β_{sim}	α_{seq}	β_{seq}
0.2	0.067	0.030	0.000051	0.087
1	0.067	0.013	0.00026	0.017
5	0.068	0.0032	0.0013	0.0035
10	0.070	0.0017	0.0026	0.0017

Since these constants (α and β) are known, the measured images I^{green} and I^{red} can be used to determine the images where RFP and GFP are separated, using:

$$I^{green}_{GFP} = \frac{I^{green} - \beta I^{red}}{1 - \alpha\beta} \quad \text{and} \quad I^{red}_{RFP} = \frac{I^{red} - \alpha I^{green}}{1 - \alpha\beta} \qquad \text{Eq. 2A.5}$$

It should be noted, that subtraction of both measured images according to Eq. 2A.5 is only possible when the cameras convert photons to counts in a same way. Otherwise, the sensitivity and EMgain settings have to be corrected for. Using the Poisson distribution of the light, and plotting the variance of the recorded intensity versus the intensity of the light, revealed that the photon processing in Ixon+ cameras occurs in a three step process. First, the photons are converted into

electrons (determined by the quantum efficiency of the photosensitive layer, QE). Second, the electrons are multiplied, as specified by the EM gain setting (EMgain). Third, the electrons are converted into intensity units by the A/D converter, with a certain sensitivity depending on the settings of the camera ($sens_{CCD}$), specified in the specification sheet provided by the manufacturer. Therefore, the recorded fluorescence images can be corrected for the differences between the cameras by replacing I^{green} and I^{red} in Eq. 2A.5 by:

$$I^{green} = I^{green}_{measured} \frac{sens_{CCD-green}}{EMgain_{green} \cdot QE(\lambda)} \qquad \text{Eq. 2A.6a}$$

$$I^{red} = I^{red}_{measured} \frac{sens_{CCD-red}}{EMgain_{red} \cdot QE(\lambda)} \qquad \text{Eq. 2A.6b}$$

Chapter 3 –

Characterisation and testing of TIRF-OT method[4]

3.1 Introduction

It is becoming increasingly evident that for proper signalling not only the type, but also the spatial distribution and dynamics of membrane proteins is important (Grakoui et al., 1999, Cambi et al., 2006, Kusumi et al., 2005). We present here a hybrid TIRF-OT instrument to study the dynamics of the cell surface proteins upon interaction with a functionalized surface. We show that optical tweezers (OT) are excellent tools for spatial and temporal control of the interaction. First, we describe the characterization of the TIRF-OT method (section 3.2). Second, we test the setup by studying cell-substrate interactions. Since cell-cell interaction and communication is of particular relevance in the adaptive immune system, we studied the interaction of ALCAM with CD6 in our proof-of-principle experiments. ALCAM plays an important role in DC – T cell interactions and the ALCAM distribution on the cell surface shows strong changes upon interaction with other cells (Zimmerman et al., 2006). We studied the dynamics of the redistributions of ALCAM using ALCAM-GFP expressing cells brought in contact by OT with a CD6 coated surface. The materials and methods for these experiments are described in section 3.3, the results in section 3.4, followed by the conclusions and discussion in section 3.5.

[4] Parts of this chapter have been published as "Snijder-Van As, M. I., B. Rieger, B. Joosten, V. Subramaniam, C.G. Figdor, and J.S. Kanger (2009). "A hybrid total internal reflection fluorescence and optical tweezers microscope to study cell adhesion and membrane protein dynamics of single living cells." Journal of Microscopy-Oxford **233**(1): 84-92".

3.2 Characterization of a hybrid TIRF-OT microscopy method

3.2.1 Steerable optical tweezers - accuracy

We achieved steerable optical tweezers using two 4f-systems (Fig. 2.2). The scanning lens and scanning mirror determine the accuracy in the trap position. This accuracy was measured using a trapped polystyrene bead and a tracking algorithm. This revealed the trap could be move in steps of ~ 10 nm in the *xy*-direction., and ~ 1nm in the *z*-direction. Furthermore, we measured the axial speed with which a trapped particle can be moved towards the surface. Theoretically, this is limited by the actuator speed, which would correspond to a speed of ~0.6 μm/s. We measured the speed by trapping a fluorescent bead and bringing it towards the surface during constant TIRF illumination and fluorescence detection. This revealed a speed of ~0.5 μm/s. Besides, we measured the beam diameter of the infrared laser beam, in order to ensure slight overfilling of the back-aperture of the objective, which gives a stable optical trap (Lee et al., 2007). This revealed a beam diameter of ~ 950 μm, (at $1/e^2$ values), requiring a beam expansion of ~8x. Finally, a cell was trapped and moved with 1 μm steps in the axial direction with maximum speed. The cell stayed trapped, indicating stable trapping and validating we can move the trap with the maximum possible speed. Since we move the cell upwards in steps of 1 μm and use a measurement frequency of 1 Hz (maximally), the uncertainty in the starting point of interaction is ~ 2s.

To determine the actual accuracy with which a trapped cell can be positioned on a surface or another cell is difficult. This accuracy depends not only on the precision with which the trap can be moved, but also on the shape, size and movement of the trapped cell. In the first place, Brownian motion will give an uncertainty in the positioning; the trapped particle might be (slightly) out of the centre of the trap. Furthermore, in case of a cell, usually a (small) organelle in the cell is trapped. The relation between the Brownian motion of the cell and the displacement of the cell due to displacement of the trap is unknown. Finally, the outer shape of the cell will determine the exact position where the cell will first contact the substrate; the dendrites of a cell might interact with the surface at

another position than the centre of the trap. Together, the accuracy in positioning a cell on a substrate is estimated to be on the order of the radius of the cell.

3.2.2 Optical tweezers: cell damage by laser light

For non-destructive optical trapping of cells, the wavelength and power of the trapping laser have to be considered. Ramser and Hanstrop (2010) review several studies concerning the influence of infrared laser light on cell viability. This viability is usually quantified by measuring the cloning efficiency of cells exposed to light, which might be a more stringent criterion than necessary for cell-substrate and cell-cell interactions. Infrared lasers in general have low absorption by water and, therefore, do not heat the sample too much. Photodamage of cells seems dependent on power density, integral light dosage and possibly other parameters like the size of the illuminated spot (Schneckenburger et al., 2000). This makes comparison between various publications difficult. Schneckenburger et al. (2000) report that colony formation is almost unchanged upon 830 mW, continuous wave, 1064 nm laser illumination for 120 s. In our case, stable cell trapping was observed for a laser power at the backside of the objective of ~500 mW. The average time a cell was held in the trap was ~ 120 s. These values are in the same range as used by Schneckenburger et al., hinting that the infrared laser light used for trapping does not harm the cells. A further indication is that cell spreading is observed upon cell-substrate interactions. Finally, cell morphology imaged with white light did not show changes upon trapping of the cells. A firmer proof of cell viability would be a live-dead staining, for example with trypan blue. In general, this showed that the cells in the flowcell were alive; however, this staining could not specifically target the trapped cells. To conclude this section, we can use a laser power of ~ 500 mW for trapping cells, but the time the cells are trapped should not be longer than necessary to reduce possible photodamage.

3.2.3 Optical tweezers: forces on cells

To calculate the force exerted by the OT on the cell, the escape force can be measured (Svoboda and Block, 1994). We trapped a K562 cell and gradually increased the flow of the buffer surrounding the cell. Once the cell escaped the trap, the displacement recorded by a camera was converted into an escape speed. From

this measurement, the escape force could be calculated as a measure for the trapping force. This revealed a maximum lateral force of ~30 pN on K562 cells exerted by 500 mW of 1064 nm laser light. The axial force that the OT can exert on the cell is smaller than the lateral force (Sheetz, 1998).

In our experiments, we trap a cell and bring it in contact with a surface or another cell in steps of 1 μm at a speed of ~ 0.5 μm/s. Since it is possible that the trap is moved upwards more than necessary to initiate contact, we estimated the effect on the initial contact size of pressing the cell against a glass surface using OT. The stiffness of a cell is determined by the Young's modulus (E), which is 1-100 kPa for living cells (Discher et al., 2005). The indentation of the cell is given by $\Delta L = L_0 P / E$, where L_0 is the diameter of the cell, P is the pressure exerted by the OT. In the specific case described here, P=30 pN/(πx7.5^2 μm^2) and L_0=15 μm, this gives a maximum indentation ΔL of ~ 0.1-10 nm. Since $\Delta L << L_0$, this does not result in a measurable difference in the size of the contact site upon pressing the cell against the glass using OT. This conclusion was confirmed by test experiments (data not shown).

3.2.4 Dual colour detection – crosstalk experiments

To test the crosstalk in our dual colour measurement configuration, cells expressing ALCAM-GFP and cells expressing CD6-RFP were placed in a flow cell on a TIRF microscope (details about the cells, cell culture, flow cell preparation and experimental setup can be found in chapter 5). The intensity ratio (χ, Appendix 2A) between 488 nm and 568 nm laser light was 1:5. The differences between the cameras can be addressed as specified in Appendix 2A. Since the EM gain settings for both cameras were the same, and the quantum efficiencies for GFP and RFP fluorescence detection and the sensitivity of the A/D converter, as specified by the manufacturer, were similar to each other, we ignored the differences between the cameras in the calculations below. TIRF microscopy images with both GFP and RFP expressing cells in the same field of view were collected separately for only 488 nm or 568 nm illumination, and for simultaneous illumination with 488 nm and 568 nm laser light. ImageJ was used to determine the mean and maximum intensity of both fluorophores on both cameras (with background correction).

The $\frac{I_{GFP}^{green}}{I_{GFP}^{red}}$ and $\frac{I_{RFP}^{green}}{I_{RFP}^{red}}$ ratios were determined from the experiments, where green refers to the CCD camera 1 (detecting the lower wavelengths) and red to camera 2 (detecting the higher wavelengths). These ratios can be theoretically described by the formulas in Table 3.1 (based on Appendix 2A). Table 3.2 gives the numbers for the theoretical calculations and the experimentally determined values for the ratios of both fluorophores on both channels (averaged over 7, 6, 7 or 5 cells, respectively). The ratios provide a method to relate theory and experiment.

Table 3.1 Intensity ratios - formulas

488 nm illumination	*488 nm + 568 nm illumination*
$\frac{I_{GFP}^{green}}{I_{GFP}^{red}} = \frac{C_{GFP}^{green}}{C_{GFP}^{red}}$	$\frac{I_{GFP}^{green}}{I_{GFP}^{red}} = \frac{C_{GFP}^{green}}{C_{GFP}^{red}} \frac{\Phi_{GFP}^{488}}{\Phi_{GFP}^{488} + \chi\Phi_{GFP}^{568}}$
$\frac{I_{RFP}^{green}}{I_{RFP}^{red}} = \frac{C_{RFP}^{green}}{C_{RFP}^{red}}$	$\frac{I_{RFP}^{green}}{I_{RFP}^{red}} = \frac{C_{RFP}^{green}}{C_{RFP}^{red}} \frac{\Phi_{RFP}^{488}}{\Phi_{RFP}^{488} + \chi\Phi_{RFP}^{568}}$

Table 3.2 Intensity ratios - numbers

	488 nm illumination		*488 nm + 568 nm illumination*	
	$\frac{I_{GFP}^{green}}{I_{GFP}^{red}}$	$\frac{I_{RFP}^{green}}{I_{RFP}^{red}}$	$\frac{I_{GFP}^{green}}{I_{GFP}^{red}}$	$\frac{I_{RFP}^{green}}{I_{RFP}^{red}}$
Theory	14.9	0.046	14.6	0.0032
Experiment	5±1	1±0.7	3±1	0.1±0.07

For the GFP ratios, the theoretical and experimentally determined numbers are in the same order of magnitude. The experimentally determined RFP ratios, however, differ more than an order of magnitude with the theoretical ratios. This might suggest that the emission spectrum of the RFP fluorophore attached to the CD6 is not the same as the one used for the theoretical calculations. However, the change between only 488 nm and 488 nm + 568 nm illumination for the experimental and theoretical ratios for RFP is similar, indicating that the excitation efficiencies used in the calculations correspond to the experimental values.

Together, the experimentally determined GFP ratios that correspond to the theoretical values and the change between the RFP ratios for single and simultaneous illumination, point towards a validation of the theory in Appendix 2A. This indicates that Eq. 2.4 can be used to correct for the crosstalk between the channels in the case of simultaneous illumination, although the correct α and β have still to be determined for experimentally used RFP. However, because of two reasons, we decided to use sequential imaging in our proof-of-principle. In the first place, the processes we studied are on longer time scales (measurement frequency 1 Hz), so sequential imaging will most likely hardly interfere with colocalisation studies (this has to be validated for the biological relevant – not proof-of-principle – experiments), and data processing would be more direct because it does not require crosstalk compensation. In the second place, the GFP fluorescence signal had a higher intensity than the fluorescence detected from the RFP, so RFP fluorescence detection could be performed more sensitively (with a higher EM-gain) when GFP was not emitting during RFP detection. Although higher excitation power (with 568 nm light) would also increase the RFP signal, this has the disadvantage of increased photobleaching. Therefore, the dual colour imaging proof-of-principle experiments presented in chapter 5 were performed using sequential imaging, in which case RFP fluorescence detection on the green camera can be ignored. For future experiments, especially on fast processes, we recommend simultaneous excitation and detection. Then, Eq. 2.4 can address the measured crosstalk.

3.2.5 Computer control - experiments

The positioning of the lenses is crucial for the alignment of the trap. Perfect alignment of all lenses would provide only lateral or axial movement of the trap upon moving the scanning mirror or scanning lens (respectively). We tested the alignment of the lenses by trapping a polystyrene bead and moving the trapped bead using the LabVIEW program. Lateral displacement of the bead in purely x and y was possible in the field of view. However, moving the trapped bead in the axial direction resulted in a lateral movement as well, most likely caused by improper alignment of the lenses in the OT optical path. Since it appeared difficult to correct this by alignment of the lenses, we addressed the issue with the computer controlled steering. We measured the misalignment for several displacements in the axial

direction by determining the lateral position of the trapped bead. From these measurements, we deduced the general behaviour of lateral movement for a bead trapped at (x,y=0,0) upon axial displacement, which was x=-1.12z and y=-1.96z. The LabVIEW VI managing the OT position was corrected for this displacement.

3.2.6 Surface functionalization

For the cell-substrate proof-of-principle experiments described in this chapter, we used a three step coating protocol. First, goat-anti-human-fc (gαHu-fc) antibodies were adsorbed to a microscope glass. Second, the remaining area of the glass was blocked using bovine serum albumin. Third, human-CD6-fc was incubated on the slide, which binds to the gαHu-fc antibodies. To optimize the protocol, we performed a titration experiment on both the concentration of gαHu-fc and CD6-fc, the latter using a concentration of gαHu-fc of 10 μg/ml. After incubation, we stained the gαHu-fc antibody and the CD6-fc with, respectively, rabbit-anti-goat-Alexa488 or mouse-anti-CD6 and goat-anti-mouse-Alexa 647. Then, we measured the total fluorescence intensity in the field of view for the various concentrations using confocal microscopy (LSM510, Zeiss). Fig. 3.1 shows the sum intensity versus the concentration of gαHu-fc antibody (Fig. 3.1A) and

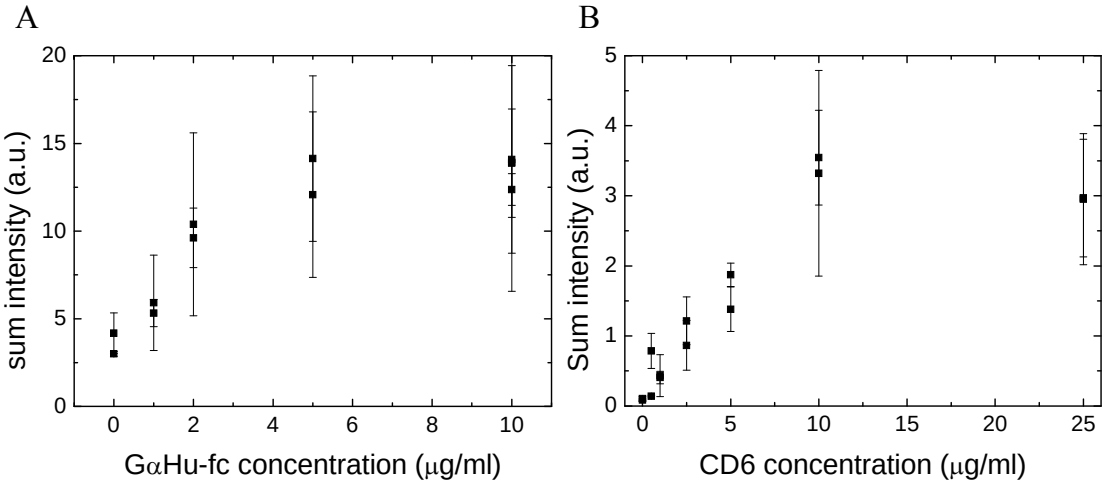

Fig. 3.1 Surface functionalization optimisation The sum intensity of fluorescently stained functionalized glass surfaces versus the incubation concentration. Per concentration 2 samples were made and each sample was measured at ~7 spots. The intensities per sample were averaged and the graphs show the mean and standard deviation. A. average sum intensity versus gαHu-fc antibody concentration. B. average sum intensity versus CD6-fc concentration.

CD6-fc (Fig. 3.1B) averaged over various points per sample. That the curves do not go through the origin is due to the gain settings of the microscope. For both situations, a concentration of 10 μg/ml is optimal. This is the concentration used in the experiments in section 3.4.

3.2.7 Image segmentation – testing

We used isodata-thresholding to segment the images. To test the influence of intensity fluctuations in the fluorescence images on the segmentation, we used test images. These images were computer generated, and contained a large gray sphere mimicking a cell in a black background, with high intensity spots inside the cell. The segmentation of these images revealed that the intensity of the cell does not influence the segmentation. For our fluorescence measurements, this implies that photobleaching does not influence segmentation (as was confirmed by segmentation of a time series of images in which the fluorescence is subject to strong photobleaching). However, when the cell contains many high intensity spots, this does influence the segmentation (the object becomes too small compared to manual segmentation), especially for larger differences between cell and background intensities. This can be understood in view of the initial assumption of the isodata thresholding, namely that the intensity histogram shows a bimodal distribution, whereas with high intensity spots within the object it is more a trimodal distribution. This should be considered when the fluorescence images show high intensity spots, instead of a more homogenous distribution. In these cases, the use of a fixed threshold might be more appropriate.

Furthermore, we examined whether our image display a bimodal distribution. Fig. 3.2A shows the histogram of an intensity distribution for a K562-ALCAM-GFP cell on CD6 functionalized glass (measurements are explained in detail later in this chapter). As can be seen, indeed a bimodal distribution is observed, and the isodata-thresholding determines the first threshold value at 175 (depicted by the arrow). The corresponding fluorescence image is shown in Fig. 3.2B, where the red line shows the segmentation of the cell body from the background (first thresholding), and the green line the segmentation of the clusters (second thresholding). From Fig. 3.2, it can be concluded that isodata-thresholding is valid and applicable on the recorded TIRF images. After thresholding, the data is

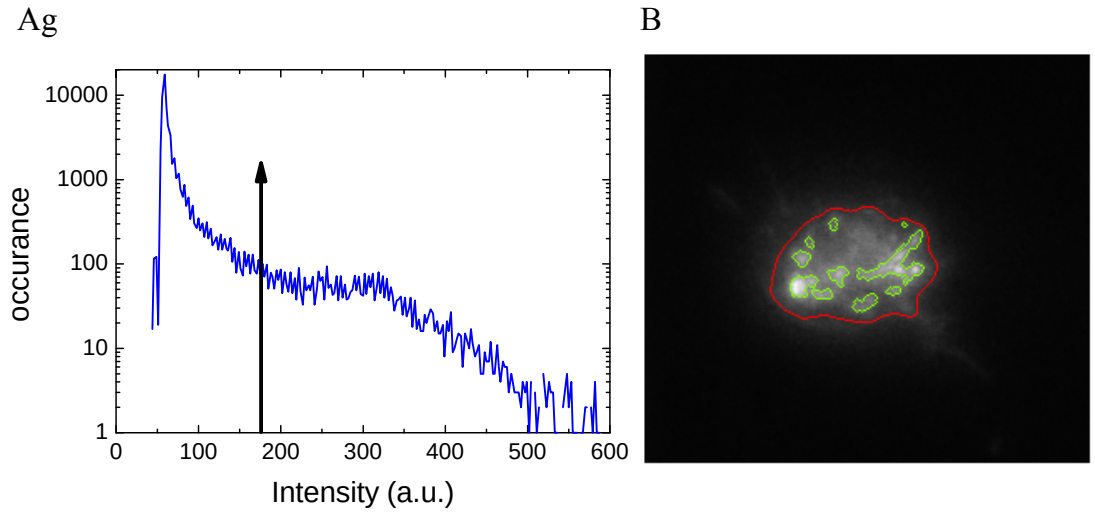

Fig. 3.2 Image segmentation A. Histogram of the intensity distribution in a TIRF image of K562-ALCAM-GFP cells on CD6 functionalized glass. The arrow indicates the position of the first threshold determined by isodata-thresholding, segmenting the cell body from the background. B. TIRF image corresponding to the histogram in (A), with the red line depicting the contour of the cell body and the green line the contour of the clusters (image size ~30x30 μm).

processed further, to obtain the contact area as a function of time and the homogeneity of the ALCAM distribution at the contact site, which is described next.

3.2.8 Homogeneity

We were motivated to investigate the homogeneity, because of the distribution of ALCAM observed with confocal microscopy on K562-ALCAM-GFP cells. Fig. 3.3A shows a projection of a 3D image of two interacting K562-ALCAM-GFP cells. The original images were recorded as a z-stack with steps of 0.35 μm in the *z*-direction. As can be seen, the ALCAM-GFP is organized in a clustered manner, while at the interaction site the distribution is more homogeneously distributed. This motivated us to quantify the distribution at the interaction site over time. Therefore, as explained in section 2.7.2, we segmented the cell body by a second isodata-thresholding, to determine whether high intensity spots were present. Then, we tried various measures for the homogeneity of the cell body: the sum intensity in the spots compared to the sum intensity in the rest of the cell body, the ratio between the total size of the spots and the size of the cell body,

the roundness of the spots, and the number of spots. The measure should show a change upon contact initiation, for ALCAM specific interaction, but not for aspecific cell interactions (corresponding to detection by eye). This revealed that the measure 'number of spots divided by the contact size' was the most relevant measure during the experiments of chapter 3. Test experiments of the cells on poly-L-lysine coated substrates, on which no ALCAM specific redistribution was observed, revealed that this measure was constant over time, indicating that it is sensitive to fluorescence redistribution towards a more homogenous ALCAM-GFP distribution.

Furthermore, the confocal microscopy experiments (Fig. 3.3A) showed that almost all cells expressed ALCAM-GFP and this ALCAM-GFP is expressed at the cell membrane. This was supported by flow cytometry experiments, where the ALCAM on the outside of the cell was stained with an anti-ALCAM antibody. Therefore, we assume all fluorescence is from the membrane at the contact site, not from within the cell.

Finally, test measurements were performed in which the outer cell membrane was stained with DiI (following the protocol of the manufacturer, Invitrogen). Fig. 3.3B shows an overlay of DiI and ALCAM-GFP fluorescence images, measured by TIRF microscopy. The intensity distribution of DiI was, in

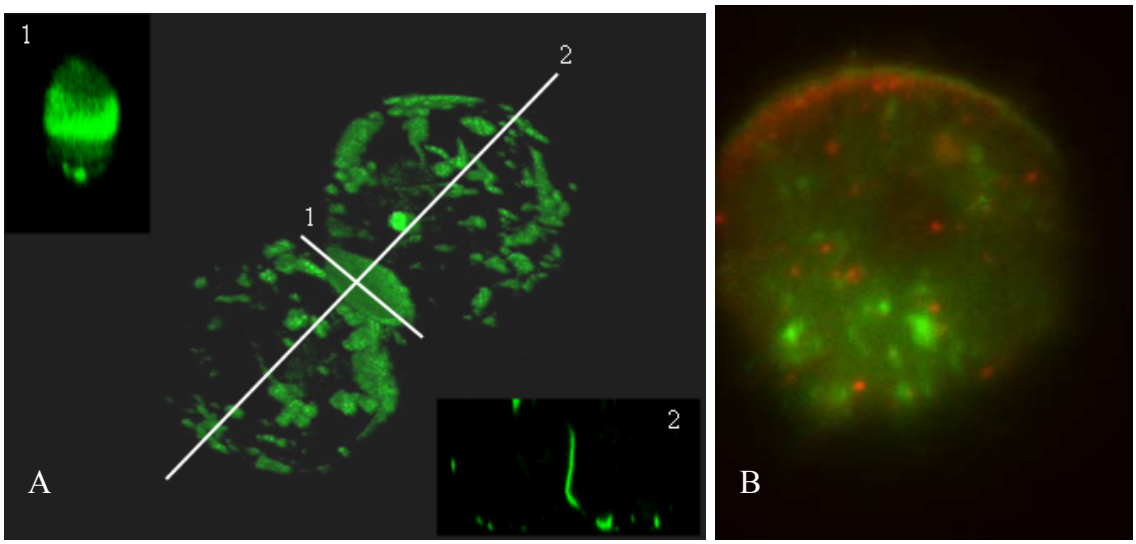

Fig. 3.3 Testing for homogeneity A. Projection of 3D image of two interacting K562-ALCAM-GFP cells, calculated from a z-stack measured by confocal microscopy, with two cross-sections along the depicted lines. B. Dual colour image of K562-ALCAM-GFP cell with membrane stained with DiI (image ~ 32*25 μm).

general, homogenous, indicating that the distance of the membrane to the surface is constant across the cell-surface contact area. The image, furthermore, shows a different fluorescence distribution for GFP and DiI, which demonstrates that the measured ALCAM-GFP distribution is not an artefact of the sensitivity of TIRF microscopy for the distance to the surface. Therefore, the intensity distribution of ALCAM-GFP can be used to measure the ALCAM-GFP spatial distribution at the contact site.

3.2.9 Image alignment of the two cameras

In dual colour experiments, images are collected by two cameras. To produce a perfect overlay of the image obtained by both cameras, offline processing was used as described in section 2.7.3. We used a test slide to calibrate the overlay. This slide contained many 100 nm fluorescent beads, detected on both cameras. Before translation of the image of camera 2 (depicted in red in Fig. 3.4A), the overlay was not perfect. However, after using *fmmatch* and *find_affine_trans* (two DIPimage functions), the images were nicely overlapping (Fig. 3.4B). Since no red and green edges were detected around the yellow coloured beads in the image, the overlay has a pixel accuracy. Since colocalisation measurements (chapter 5) are done on a pixel bases, this pixel accuracy is sufficient. Translation characteristic corresponding to

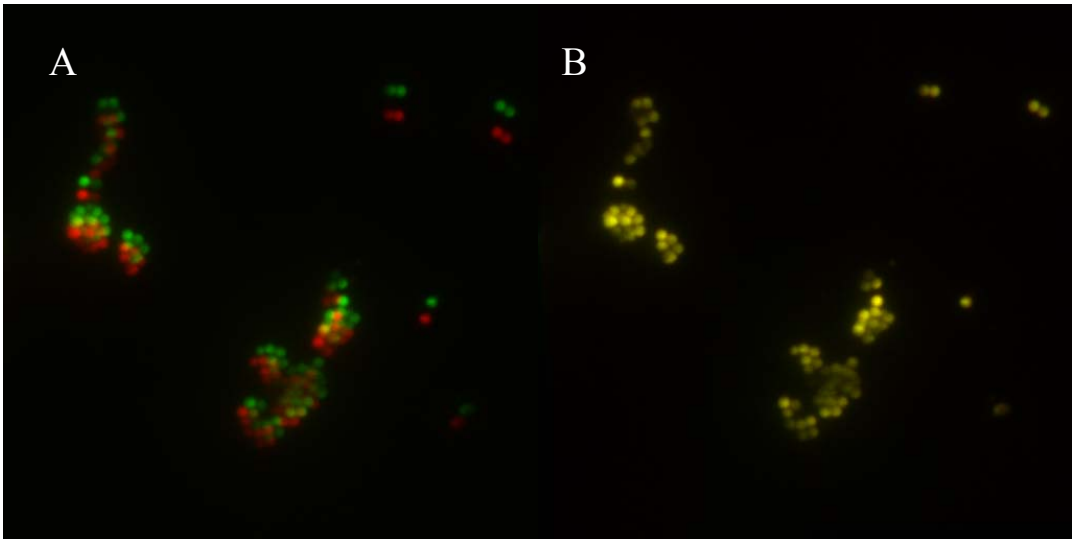

Fig. 3.4 Dual colour imaging Overlay of images of two cameras, one detecting wavelengths below 560 nm (in green), on detecting wavelengths above 560 nm (in red). A. overlay before shifting, rotating and changing the magnification of the red image, B. overlay after translation of the red image.

these images are: 1.006 (horizontal magnification), 1.04 (vertical magnification), -4.79 pixels (horizontal shift), 13.7 pixels (vertical shift) and -0.024 rad (rotation). The origin of the difference in horizontal and vertical magnification is unknown. The translation matrix obtained for the images in Fig. 3.4 was used to overlay all dual colour images.

3.2.10 Summary characterisation – specifications

Having characterized the hybrid TIRF-OT microscopy method, here we summarize the specifications relevant for and used in cell-substrate and cell-cell experiments (Table 3-3).

Table 3.3 Specification TIRF-OT microscopy method

	Numerical specification	*Comment*
Excitation wavelengths	488 nm, and 532 nm or 568 nm simultaneously	532 nm not used in this thesis
Emission wavelength peaks	514 nm (GFP) or 525 nm (GFP/YFP), and 593 nm or 610 nm (RFP)	Simultaneous dual colour detection
Trapping laser	1064 nm; ~500 mW	
TIRF angle	~60-70 deg	
Field of view EMCCD or ICCD camera	512*512 pixels ~50*50 μm	~100 nm/pixel
OT displacement	*x,y*: ± 40 μm *z*: ± 15 μm	larger displacements unverified
OT resolution	*x,y*: 10 nm; *z*: 60 pm *x,y,z* (with cell trapped): ~ 1 μm	
OT speed	*x,y*: ~ 60 μm/s *z*: ~ 0.5 μm/s	
OT exerted force	~ 30 pN for cells	
Flowcell thickness	~ 80-100 μm	
Prism material	Glass, *n*=1.51	
Temperature during experiments	~23 ºC or 37 ºC	
Throughput	1 cell/measurement duration	In practise ~2 cells/h
Measurement frequency	Up to 35 Hz full frame	

3.3 Materials and methods cell-substrate experiments

3.3.1 Substrates

Microscope slides for cell-substrate interaction experiments were cleaned with 70% ethanol before coating. CD6 coated surfaces were prepared using a three step method. First, the glass was incubated for 1 hour at 37˚C with 10 μg/ml goat anti human-Fc (Jackson ImmunoResearch, West Grove, PA) in TSM (20 mM Tris-HCl (pH 8.0), 150 mM NaCl, 1 mM $CaCl_2$, 2 mM $MgCl_2$). After washing with TSM, the uncovered glass surface was blocked with TSM containing 1% bovine serum albumin (BSA), incubated for 30 min. at 37˚C, again followed by washing with TSM. Finally, the glass surface was incubated with 10 μg/ml recombinant human CD6/Fc (R&D systems, Minneapolis, MN) in TSM. For checking the surface distribution, mouse anti-CD6 (BD Pharmingen, San Diego, CA) was used.

BSA coated microscope coverslip glasses were prepared by incubation with a 1% BSA in TSM solution for at least 30 minutes. After incubation the slides were washed extensively with TSM.

The working distance of the objective limits the sample thickness from the coverslip to the side of excitation to ~70 μm. Therefore, the (coated) microscope slide at the top of the sample was separated from the (BSA coated) coverslip using two small strips of Parafilm M (Alcan Packaging, Neenah, WI) as a spacer, creating a channel with a fixed depth. After briefly heating, the Parafilm firmly attached to the glass surfaces, creating a tightly fixed cuvette. Shortly before the measurement, the cell suspension was introduced into the channel by capillary forces.

3.3.2 Cells

K562 cells stably expressing green fluorescent protein (GFP) tagged ALCAM (Nelissen *et al.*, 2000) were cultured in Iscove's Modified Dulbecco's Medium (IMDM) (Cambrex, Verviers, Belgium) containing 10% fetal calf serum (Invitrogen, Carlsbad, CA), 1% antibiotics/antimycotics (Invitrogen), and G418 (Gibco Invitrogen) as a selection medium. For checking the ALCAM expression, the mouse anti-ALCAM antibody AZN-L50 (van Kempen et al., 2001) was used.

Before measurements, the cells were washed and dissolved in serum-free, phenol-red free IMDM, at a concentration of $\sim 1 \times 10^6$ cells/ml.

3.3.3 Cell attachment procedure

K562 cells expressing ALCAM-GFP were used as a model system. The cell suspension was loaded in the home made cuvette. The sample was positioned on the microscope equipped with a stage and objective heater in order to keep the cells at a constant temperature of 37˚C. No CO_2 was provided during the experiment. The prism was placed on top of the cuvette. A drop of non-fluorescent matching oil between the prism and the cuvette prevented total internal reflection between the prism and the microscope glass. The laser light from the Ar^+ laser was directed at the glass-water interface with an angle $\theta = 63°$ and illuminated a circular area of diameter 60 μm, corresponding to the field of view of the CCD camera. The average intensity of the illuminated spot was 80 W/cm^2. Next, a cell was trapped with the OT well below the microscope slide. Then, the cell was raised using the OT till the cell reaches the surface. After attachment of the cell to the CD6 coated surface, the OT were turned off.

This procedure was repeated several times to measure multiple cells. A single sample was measured for maximum of two hours.

3.3.4 Data acquisition and analysis

Fluorescent images were recorded over time by taking an image every 1, 2 or 5 second(s). The exposure time was 100 ms. The recorded fluorescence time lapse images are captured with a 12 bit CCD camera and stored in 16 bit TIFF-format. Images were typical taken with a field of view of 512x512 pixels with a pixel size of 116 nm. In most cases we acquired 500-1000 time frames. The processing was done by custom written software in DIPimage (Delft University of Technology, The Netherlands, www.diplib.org), a scientific image processing toolbox for Matlab (The MathWorks, Natick, MA).

We run the software in fully automated offline batch processing mode after image acquisition. In a first step the cell body is segmented from the background. To suppress noise we smooth the image series with a x,y,t Gaussian filter (Young and van Vliet, 1995) (σ of 2 pixels) as a pre-processing step. This ensures in most

cases the segmentation of one connected cell body. The cell, given by the total fluorescence signal, is located in each time frame by an isodata threshold (Ridler and Calvard, 1978). This method automatically finds a threshold as the weighted mean of a bimodal intensity distribution. This assumption is generally fulfilled for one bright object on a darker background. Because this approach does not use one fixed threshold for all time frames, variations in the background and/or signal do not negatively influence the quality of the segmentation. The contact area is calculated as the surface area of the cell body by counting the pixels of this cell body, which is then converted into μm^2. Once the cell body is identified, we distinguish clusters of fluorophores (i.e. ALCAM-GFP clusters) within that area. To this end, we enhance the blob-like clusters by a top hat filter, given by a subtraction of a grey-level opening from the original image (Soille, 1999), with elliptical structuring element of size 11 pixels. By applying a new isodata threshold on the processed image within the previously identified area, we segment the clusters. From the number of clusters we compute a homogeneity measure defined by the spatial density of clusters: the number of clusters divided by the cell contact area.

3.4 Results cell-substrate experiments

We have studied the interaction of ALCAM expressing cells with a CD6 coated surface using the hybrid TIRF-OT microscope to quantify the effect of redistribution of the ALCAM on the cell membrane upon contact initiation as described by (Zimmerman et al., 2006). In Fig. 3.5 we show the general scheme of the method developed and the obtained images. With optical tweezers a cell is trapped (Fig. 3.5a-I) and moved towards the CD6-coated upper surface (Fig. 3.5a-II) of a cuvette. Simultaneously, an evanescent field is generated at the water-surface interface that allows continuous imaging of the fluorescently labelled membrane proteins. As soon as the cell membrane is within the evanescent field, fluorescent signals are recorded (Fig. 3.5a-III and 3.7b-0). The time at which the first fluorescent signals are observed is defined as $t = 0$ s. This means that in the image a pattern can be detected with a signal-to-noise ratio >1 in a non-patterned background. We assume this corresponds with the first contact of the cell with the coated surface. Due to the limited depth of the evanescent field, no fluorescent signals from the ALCAM-GFP are detected for $t < 0$ s. The uncertainty in the

contact time is determined by the speed with which the cell is moved to the glass. The OT are moved upwards in steps of 1 μm, with a speed of ~ 0.5 μm/s (section 3.2.1). This causes an uncertainty in the first contact time of ~ 2 s. Currently, the speed is restricted by the speed of the actuator that controls the scanning lens. The contact time uncertainty can be further decreased by increasing the speed of the scanning lens.

When the OT are switched off, a short while after the cell is brought into contact with the surface (Fig. 3.5a-IV), the cell remained at the surface confirming stable contact between cell and surface. The dynamics of the cell and the membrane proteins are 'continuously' monitored by TIRF microscopy (Fig. 3.5b-30/100/300/1000). Control experiments with K562 cells without ALCAM-GFP expression showed no autofluorescence of the cells, so all detected light is

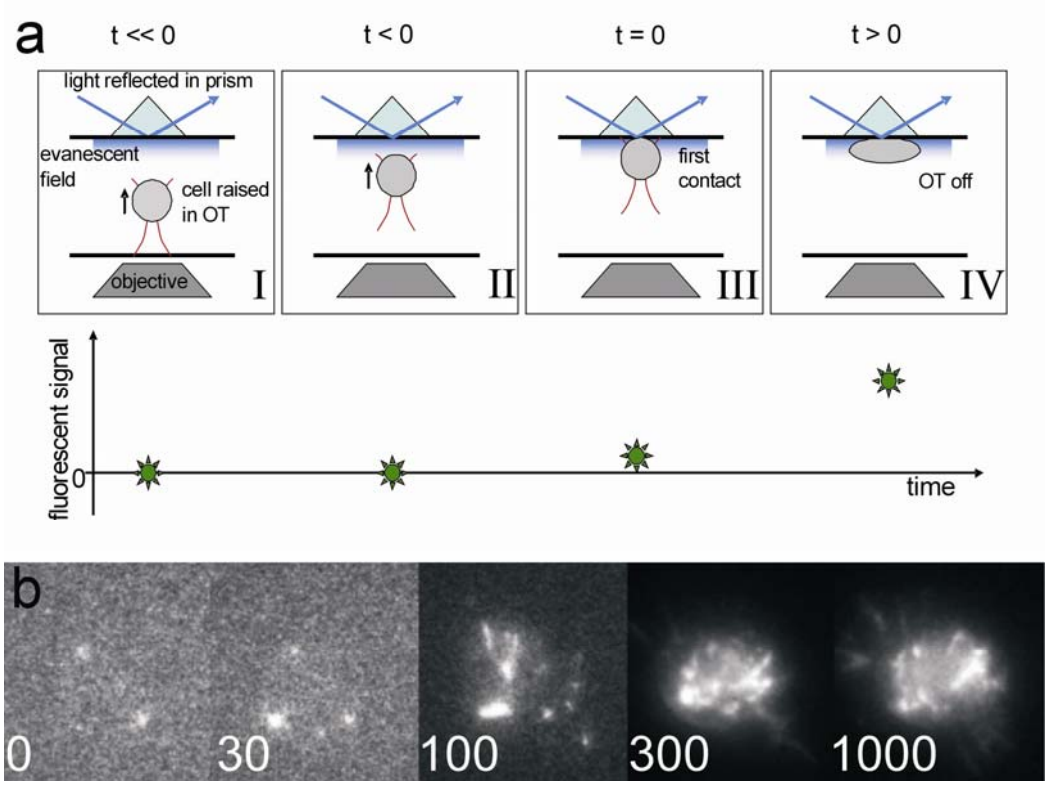

Fig. 3.5 OT-based cell trapping and adhesion a) Schematic of the method a-I) A cell is trapped far below the upper surface of a cuvette. Prism-based TIRF is used to record fluorescence from fluorescently tagged membrane proteins. a-II) Cell is moved upwards, but is still not in the evanescent field, so the detected fluorescent signal is zero. a-III) Cell in first contact: t = 0 s, a fluorescent signal is detected. a-IV) OT are turned off and the cell is spreading on the surface. b) Timeseries of fluorescent images: K562-ALCAM-GFP in contact with a CD6 coated surface. Images are 22 x 22 μm and auto scaled, time is in seconds. t = 0 s determines point of the first contact.

associated with ALCAM-GFP (data not shown). Because low laser intensity was used, photobleaching appeared to be negligible. Furthermore, no fluorescence by two-photon excitation of the 1064 nm trapping laser was observed (data not shown). Cell viability before and after trapping with OT was tested using trypan blue staining, pH measurements and light microscopy to observe possible morphological changes; this revealed no damage to the cells caused by the OT (data not shown).

3.4.1 Contact area

Fig. 3.6 shows the contact area of the cell with the microscope slide as a function of time measured for several cells in contact with a CD6 coated surface. The TIRF-OT method allows accurate determination of the time of first contact and therefore allows us to average data obtained for many different cells. As an example, Fig. 3.6 shows the contact area curve calculated as the average of 13 measured cells. Such averaging allows more accurate determination of the temporal evolution of relevant cell-surface contact characteristics and demonstrates one of the main advantages of combining OT with (in our case) TIRF microscopy.

Chamaraux et al. (2005) describe the kinetics of cell spreading. They associate stress at the margin of the contact area with actin polymerization, postulating that cell spreading is controlled by membrane-cytoskeleton attachment. Based on this, they present an analytical model for the development of the contact area over time:

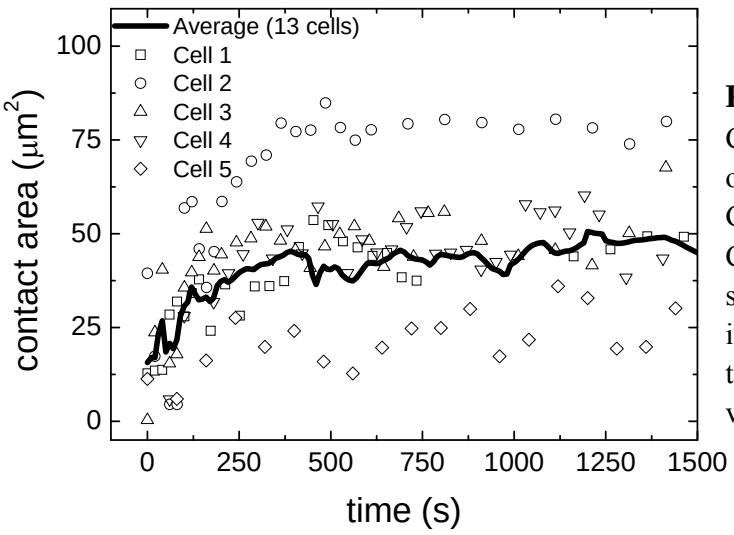

Fig. 3.6 Contact area Contact area as a function of time for K562-ALCAM-GFP cells in contact with a CD6 coated surface. After a short period (~ 30 s) the cell is stretching on the surface till it reaches a steady state value (at ~ 350 s).

$$\frac{S(t)}{S_\infty} \approx \tanh(\alpha t) \qquad \text{Eq. 3.3}$$

where *S(t)* denotes the surface contact area as a function of time *t*, S_∞ gives the maximum contact area for $t \rightarrow \infty$, and in which α^{-1} is a characteristic time, determined by the shear stress, Young modulus, actin polymerization speed and other cell characteristics. To account for the variation in the initial contact size, we added a constant S_0 to the expression for *S(t)* (Eq. 1) resulting in:

$$S(t) = S_0 + (S_\infty - S_0)\tanh(\alpha t) \qquad \text{Eq. 3.4}$$

The OT do not influence the size of the initial contact area (section 3.2.3). The variation in the initial contact size can be understood, however, by realizing that the position of the cell with respect to the position of the optical trap is unknown. Usually, the ability to trap a cell relies on trapping a small organelle inside the cell. The position of the cell membrane with respect to the trapped organelle gives an uncertainty in the order of the diameter of the cell (~ 15 μm). In addition, the membrane bound ALCAM-GFP that is already within the evanescent field, but not yet in contact with the surface, is already detected by TIRF. The influence of the extent of the evanescent field (defined as the distance from the surface at which fluorophores are still detectably exited and recognized as cell – not to be confused with the penetration depth) can be estimated assuming a spherical cell with homogenous distribution of the fluorescence at the membrane surface, using $S=\pi d_e(2R_{cell}-d)$; where *S* is the appeared contact area, d_e is the extent of the evanescent field and R_{cell} is the radius of the cell. For example, a cell with a radius of 7.5 μm and an extent of the evanescent field of 100 nm or 300 nm gives a calculated offset in the contact area of ~ 5 μm^2 or ~ 14 μm^2 respectively, the latter is comparable to the value found experimentally. It should be noted that this offset caused by the extent of the evanescent field is most likely time dependent as the curvature of the cell membrane changes with increasing contact area. As a first approach this is not included in the model. Fitting the measured contact area curves of individual cells (Fig. 3.6) using Eq. 3.4 failed because the traces are too noisy. However, the variation between the traces of the different individual cells appears to arise mainly from the offset and final contact area and to a much lesser extent to the characteristic time $1/\alpha$. Therefore, it is reasonable to fit Eq. 3.4 to the averaged data.

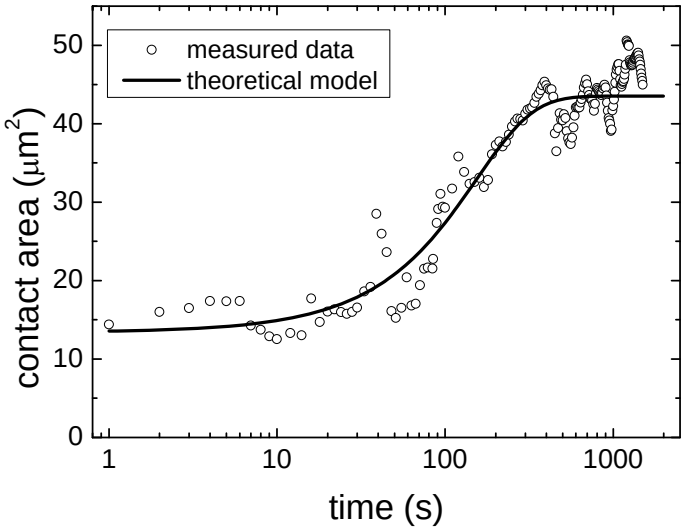

Fig. 3.7 Average contact area over time Averaged (over 13 cells; circles) and fitted (solid line) contact area over time for K562-ALCAM-GFP cells in contact with a CD6 coated surface. Fit is according to Eq. 3.4.

Fig. 3.7 shows the result of fitting Eq. 3.4 to the averaged experimental data of Fig. 3.6. The model shows a good correlation with the data. This result supports the assumption that the characteristic time $1/\alpha$ does not vary much from cell to cell. From the fit we find $S_{fit} = S_\infty - S_0 = 30 \pm 0.76$ μm^2; $S_0 = 13 \pm 0.74$ μm^2; $\alpha = 0.005 \pm 0.0003$ s^{-1}. To compare these values with values for individual cells, we calculated the standard deviation for S_∞ and S_0 for each measured individual cell. Because fitting was not feasible, values of S_0 were obtained by averaging the contact area between time $t = 0$ s and $t = 10$ s, values of S_∞ by averaging the contact area between $t = 1000$ s and $t = 1500$ s, and values for α by a linear fit between $t = 0$ s and $t = 200$ s divided by $(S_\infty - S_0)$ (since for small t the slope of Eq. 3.4 can be approached by $\alpha(S_\infty - S_0)$). From this we obtained a standard deviation of S_∞ of 19 μm^2, a standard deviation of S_0 of 11 μm^2 and a standard deviation of α of 0.003 s^{-1}, confirming the large cell-to-cell variations. The mean values for $(S_\infty - S_0)$ and α, however, were similar to the ones for the averaged curve, confirming the feasibility of averaging.

3.4.2 Homogeneity

A more thorough analysis within the cell contact area reveals the dynamics of the distribution of the ALCAM-GFP molecules at the contact site. Within the determined cell surface, we segment the spots as described above to discriminate between clustered molecules (with a high total fluorescent intensity) and non- or less-clustered molecules (see also Fig. 3.2B). CSLM measurements confirmed

saturation and homogeneity of the CD6 coated surfaces, by staining the surface with anti-CD6 antibodies (section 3.2.6). Therefore, we believe that the CD6 distribution is not causing the clustering at the surface. Furthermore, staining the outer cell membrane with DiI showed a homogenous intensity distribution indicating that the distance of the membrane to the surface is constant across the cell-surface contact area (Fig. 3.3B). As a consequence the measured spatial intensity distribution of ALCAM-GFP at the contact area directly reflects the distribution of ALCAM-GFP in the contact area. The average cluster size is 0.5 μm^2 with a standard deviation of 0.4 μm^2, although also much larger clusters are observed. There was no significant change in the cluster size over time. In Fig. 3.8, we show the cluster density of the ALCAM-GFP distribution at the interaction site, measured as the number of clusters per square micrometer. Clearly, a fast 5-fold decrease in the number of high density spots (ALCAM clusters) per square micrometer is observed, indicating an active transition from an inhomogeneous ALCAM distribution towards a much more homogeneous distribution upon ligand binding during the first few minutes after contact initiation. Curve fitting with an exponential decay function shows a characteristic time for this transition of 35 ± 3 s. Fitting individual cell curves (when possible) revealed a mean transition time in the same order of magnitude with a standard deviation of 20 s.

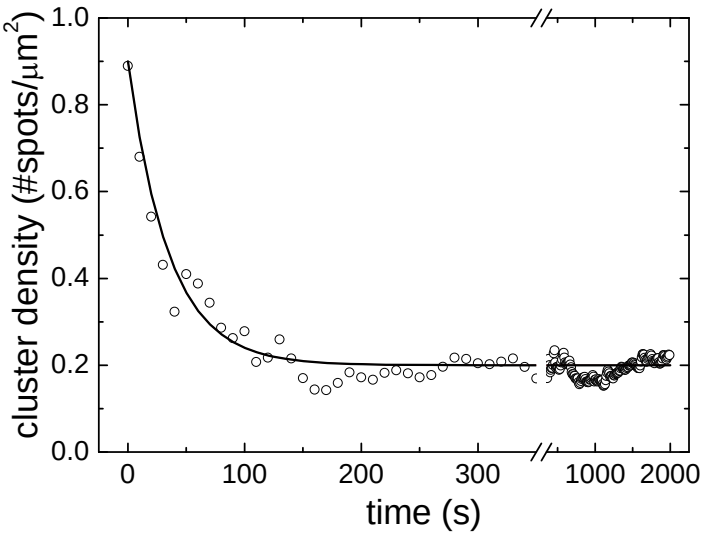

Fig. 3.8 Homogeneity Cluster density at the contact site (as a measure for ALCAM distribution), measured in number of spots per μm^2. The circles are averaged data over 13 cells; the line is a first order exponential decay.

3.5 Conclusions and discussion

We developed a hybrid microscopy technique by combining total internal reflection fluorescence microscopy with optical tweezers to accurately (both in lateral position and time) initiate and monitor cell substrate interactions. We are able to determine the onset ($t = 0 \pm 2$ s) of interaction, which enables us to synchronize experiments and therefore to average the temporal dynamics of the interaction for different cells. The observed time scale for interaction in the studied system shows that this error of 2 s in the onset is an order of magnitude lower than the observed redistribution dynamics (~30 s) and is thus acceptable. Therefore, the addition of OT to control the onset enables the determination of interaction dynamics with improved accuracy. We observed an offset in the contact area of 15 μm^2 (see Fig. 3.7). The offset was explained by both the extent of the evanescent field and the position of the cell with respect the focus of the OT. In order to reduce this offset, the penetration depth of the evanescent field could be reduced by increasing the angle of incidence θ. It should be noted, however, that beside the penetration depth of the evanescent field also the sensitivity of the fluorescence detection and the threshold in the data analysis procedure are contributing to the extent of the evanescent field. Furthermore, a rigorous data analysis method was developed for quantitative image processing. Key parameters like contact area and cluster density of membrane proteins were determined. The method was applied to measuring interactions of K562-ALCAM-GFP cells with CD6 coated surfaces. In the quantitative analysis the assumption was made that binding of the cell to the CD6 coated surface is only mediated by ALCAM-CD6 interaction. Therefore, the cell was regarded to be in contact with the surface only at those positions where ALCAM-GFP was observed.

To quantify the observed cell spreading and redistribution process, we fitted the averaged curves with a model predicted in literature (Chamaraux et al., 2005) and an exponential decay. Variables of the method influencing the variation between individual cell traces are laser power, penetration depth of the evanescent field and signal-to-background ratios. Since these values are kept constant over the experiments, these will not dramatically influence the result. In contrast to this, however, the expression level and pattern of ALCAM-GFP on the cell membrane

vary for different cells. Although it is not possible to perform several experiments on the same cell to validate this, we assume based on the aforementioned arguments that cell-to-cell variations are the main cause of the variations in individual traces. Besides that, fitting individual curves with the models appeared to be difficult, because of the 'noisy' traces of these curves. This directly shows one of the main advantages of the described method, namely: to be able to average the data over different cells because t=0 s is well-defined. This enables fitting the data and therefore quantifying the observed processes, which would otherwise be difficult. The values obtained for cell spreading using the analysis method developed in this work were in good agreement with existing models (Chamaraux et al., 2005). Furthermore, the redistribution of the ALCAM-GFP indicates an active process starting upon interaction with the CD6 surface. As can be seen comparing Fig. 3.7 and 3.10, the redistribution of ALCAM (characteristic time ~35 s) is significantly faster than the cell spreading (characteristic time (=1/α) ~330 s). Therefore, it can be concluded that the increase in homogeneity is not a direct consequence of the increase in cell contact area. The average mean intensity within the cell contact area shows no significant change over time, indicating no active recruitment of more ALCAM-GFP molecules to the contact area takes place. Elucidation of the details of the mechanisms (redistribution, recruitment, or combinations of both) will require, for example, experiments where the cytoskeleton is influenced. Most likely, both cell spreading and active redistribution of ALCAM on the cell surface are dictated by actin cytoskeleton dynamics since ALCAM-mediated adhesion is regulated through the actin cytoskeleton (Nelissen et al., 2000) and ALCAM can bind to β-actin (te Riet et al., 2007).

All experiments shown here are performed on a saturated CD6 coated surface. The final concentration might therefore be different from that found on CD6 expressing cells. Additionally, it should be noted that CD6 proteins on the substrate are immobile in contrast to membrane bound CD6. Obviously, these two constraints hamper the biological interpretation of the current data. To overcome these limitations we are currently adapting our method for the study of cell-cell interactions. Since TIRF might be difficult for studying cell-cell interactions, as a result of the thickness of the cell adhering to the glass, alternative fluorescent detection schemes could be applied in combination with OT. For example, if

processes are studied in which fast dynamics or high depth resolutions (the advantages of TIRF) are less important, CSLM can be an option.

The method developed here is, however, not limited to the study of membrane protein dynamics. The current method is suitable for studying many near-membrane processes such as near-membrane cytoskeleton dynamics, signalling, but also processes that involve dynamics of the membrane itself like the forming of podosomes. All these processes can be studied systematically in cells interacting with other cells or with e.g. structured surfaces or bi-layers (for example mimicking the proteins of the immunological synapse).

The advantage of combining OT with (TIRF) microscopy over simple settling down of the cells on a surface lies in the spatial and temporal control that is enabled by using OT. OT enable the selection of cells exhibiting specific properties (for example, bright fluorescence), and precise control of the position of the interaction (for example, at a specific place on a patterned surface) to enable optimal imaging conditions and interaction with the surface. In particular if one is interested in fast dynamics of membrane molecules, it is essential to choose a limited field of view, so that the number of pixels per image that need to be read out from the CCD camera can be kept to a minimum. However, this approach is only feasible if the cell-surface interaction takes place precisely within this small field of view, a condition that can be readily achieved using the approach described here. Alternative methods for temporal control are the use of micropipettes or cantilevers. However, those methods all rely on the previous attachment of the cell to either the micropipette or the cantilever, which may already induce a reaction of the cell. These approaches contrast with OT, where the cell can be brought into contact without physically touching the cell; after contact initiation, the OT can be easily turned off. We conclude that the combination of TIRF with OT-based cell manipulation provides a novel and powerful tool to yield precisely timed information on cell-substrate interactions. The unique ability to control the exact time and position of the interaction is a versatile approach in cell biology and immunology.

References

CAMBI, A., JOOSTEN, B., KOOPMAN, M., DE LANGE, F., BEEREN, I., TORENSMA, R., FRANSEN, J. A., GARCIA-PARAJO, M., VAN LEEUWEN, F. N. & FIGDOR, C. G. 2006. Organization of the integrin LFA-1 in nanoclusters regulates its activity. *Molecular Biology Of The Cell,* 17, 4270-4281.

CHAMARAUX, F., FACHE, S., BRUCKERT, F. & FOURCADE, B. 2005. Kinetics of Cell Spreading. *Physical Review Letters,* 94, 158102.

DISCHER, D. E., JANMEY, P. & WANG, Y. L. 2005. Tissue cells feel and respond to the stiffness of their substrate. *Science,* 310, 1139-1143.

GRAKOUI, A., BROMLEY, S. K., SUMEN, C., DAVIS, M. M., SHAW, A. S., ALLEN, P. M. & DUSTIN, M. L. 1999. The immunological synapse: A molecular machine controlling T cell activation. *Science,* 285, 221-227.

KUSUMI, A., IKE, H., NAKADA, C., MURASE, K. & FUJIWARA, T. 2005. Single-molecule tracking of membrane molecules: plasma membrane compartmentalization and dynamic assembly of raft-philic signaling molecules. *Semin Immunol,* 17, 3-21.

LEE, W. M., REECE, P. J., MARCHINGTON, R. F., METZGER, N. K. & DHOLAKIA, K. 2007. Construction and calibration of an optical trap on a fluorescence optical microscope. *Nat Protoc,* 2, 3226-38.

NELISSEN, J. M. D. T., PETERS, I. M., DE GROOTH, B. G., VAN KOOYK, Y. & FIGDOR, C. G. 2000. Dynamic regulation of activated leukocyte cell adhesion molecule-mediated homotypic cell adhesion through the actin cytoskeleton. *Molecular Biology of the Cell,* 11, 2057-2068.

RAMSER, K. & HANSTORP, D. 2010. Optical manipulation for single-cell studies. *Journal of Biophotonics,* 3, 187-206.

RIDLER, T. W. & CALVARD, S. 1978. Picture Thresholding Using an Iterative Selection Method. *Ieee Transactions on Systems Man and Cybernetics,* 8, 630-632.

SCHNECKENBURGER, H., HENDINGER, A., SAILER, R., GSCHWEND, M. H., STRAUSS, W. S. L., BAUER, M. & SCHUTZE, K. 2000. Cell viability in optical tweezers: high power red laser diode versus Nd : YAG laser. *Journal of Biomedical Optics,* 5, 40-44.

SHEETZ, M. P. (ed.) 1998. *Laser Tweezers in Cell Biology,* San Diego: Academic Press.

SOILLE, P. 1999. *Morphological Image Analysis. Principles and Applications,* Berlin, Springer-Verlag.

SVOBODA, K. & BLOCK, S. M. 1994. Biological Applications of Optical Forces. *Annual Review of Biophysics and Biomolecular Structure,* 23, 247-285.

TE RIET, J., ZIMMERMAN, A. W., CAMBI, A., JOOSTEN, B., SPELLER, S., TORENSMA, R., VAN LEEUWEN, F. N., FIGDOR, C. G. & DE LANGE, F. 2007. Distinct kinetic and mechanical properties govern ALCAM-mediated interactions as shown by single-molecule force spectroscopy. *J Cell Sci,* 120, 3965-3976.

VAN KEMPEN, L., NELISSEN, J., DEGEN, W. G. J., TORENSMA, R., WEIDLE, U. H., BLOEMERS, H. P. J., FIGDOR, C. G. & SWART, G. W. M. 2001. Molecular basis for the hemophilic activated leukocyte cell adhesion molecule (ALCAM)-ALCAM interaction. *Journal Of Biological Chemistry,* 276, 25783-25790.

YOUNG, I. T. & VAN VLIET, L. J. 1995. Recursive Implementation of the Gaussian Filter. *Signal Processing,* 44, 139-151.

ZIMMERMAN, A. W., JOOSTEN, B., TORENSMA, R., PARNES, J. R., VAN LEEUWEN, F. N. & FIGDOR, C. G. 2006. Long-term engagement of CD6 and ALCAM is essential for T-cell proliferation induced by dendritic cells. *Blood,* 107, 3212-20.

Chapter 4 –

Application of TIRF-OT method to study CD6 dynamics in cell-substrate interactions

4.1 Introduction

Dendritic cells and T-cells play an important role in the adaptive immune response against pathogens. Dendritic cells encounter the specific pathogen, degrade it, and present peptides of this pathogen to T-cells to induce an immune response aimed at defence of the host. The peptides are presented on the major histocompatibility complex (MHC) molecule, which interacts with the T-cell receptor (TCR) on the T-cell membrane. Together with many other membrane molecules that are involved in contact stabilization and costimulation, the MHC and TCR are ordered in a so-called supramolecular activation cluster (SMAC) (Janeway Jr. et al., 2005). In the central SMAC on T-cells, CD3 and CD6 are associated with the T-cell receptor (Gimferrer et al., 2004). CD3 forms a complex with the TCR molecule and is required for TCR induced signalling (Janeway Jr. et al., 2005). CD6 is a ligand for the activated leukocyte cell adhesion molecule (ALCAM) expressed on dendritic cells; together, ALCAM and CD6 are involved in contact stabilisation and costimulation (Zimmerman et al., 2006). Since CD3 stimulation induces tyrosine phosphorylation of CD6 (Wee et al., 1993), CD6 might be activated upon CD3 ligation. Furthermore, CD6 has a long cytoplasmic tail that might be involved in the recruitment of signalling molecules (Kobarg et al., 1997). A potential candidate for this role is Syntenin-1, a molecule that interacts with CD6 (Gimferrer

et al., 2005). Syntenin-1 has PDZ[5] domains, which are protein-interaction modules that can interact with phosphoinositide (PIP) molecules, which are, amongst others, involved in cytoskeleton remodelling (Zimmermann, 2006).

It has been reported that the spatial distribution of membrane molecules (like the TCR in the central SMAC) plays an essential role in T-cell signalling (Grakoui et al., 1999, Mossman et al., 2005). For example, the distribution of CD2 in microdomains induces and enhances T-cell signalling (Kaizuka et al., 2009). Zimmerman et al. (2006) have shown that CD6 is recruited to the central SMAC and involved in costimulation, however, the process by which this recruitment happens remains unclear. The interaction of CD6 with Syntenin-1 suggests involvement of the cytoskeleton, but the influence of the cytoskeleton on CD6 interaction dynamics has not been described. Furthermore, the influence of CD3 stimulation on CD6 dynamics is not well described. Because of these findings (the dynamics and distribution of membrane molecules is important for T-cell signalling and CD6 is involved in costimulation), we were motivated to study the dynamics and distribution of CD6 at the contact site upon cell interaction, as this has not been described and might have a role in how CD6 exerts its function. In this process, we also study the role of the actin cytoskeleton. We investigated the dynamics of CD6 by stimulation of a cell with a surface that is functionalized with antibodies. To monitor CD6 dynamics, Jurkat T-cells were stably transfected with CD6-RFP (Meddens, 2009). We used optical tweezers (OT) to bring a Jurkat-CD6-RFP cell in contact with a functionalized surface, to precisely control the onset of interaction, and monitored the cell-surface interaction with total internal reflection fluorescence (TIRF) microscopy, as described in chapter 3.

In this chapter, we address three main topics. First, we describe the spreading behaviour of Jurkat-CD6-RFP cells interacting with functionalized surfaces. To study whether only stimulation of CD6 already induces a cellular response, we use CD6-specifc (anti-CD6) and aspecific (anti-CD3 and anti-β1-integrin) stimulation of the cell. Since β1-integrin is involved in cell adhesion (Janeway Jr. et al., 2005), we expect cell spreading for this condition. Anti-CD3

[5] The acronym *PDZ* is based on the first letters of the three proteins the domain was first discovered in: post synaptic density protein (PSD95), Drosophila disc large tumor suppressor (DlgA), and zonula occludens-1 protein (ZO-1)

surfaces are investigated because of the described relationship between CD6 and CD3 (Wee et al., 1993). Spreading of Jurkat cells on anti-CD3 has been described, with a role for the actin cytoskeleton (Bunnell et al., 2001, Parsey and Lewis, 1993). Second, we focus on the role of the actin cytoskeleton of cells in contact with functionalized surfaces by visualizing and disrupting the cytoskeleton. Finally, we study the dynamics of the CD6 distribution on the cell surface. We quantitatively measured the recruitment of CD6 to the interaction site over time by monitoring the fluorescence intensity, in situations with intact or disrupted cytoskeleton.

4.2 Materials and Methods

4.2.1 Surface functionalization

TIRF-OT experiments were performed in flowcells constructed with a functionalized glass microscope slide. The design of the flowcell was described in section 2.6.3. The procedure for preparing the antibody coated glass was as follows. First, the microscope slide (and the associated tubing) was rinsed with 100% ethanol and blow dried in a stream of N_2. Second, a frame-shaped piece of double sided tape (3M, Zoeterwoude, The Netherlands) was placed on the glass. A hydrophobic boundary for the antibody incubation fluid was drawn with a DAKO pen (Dako, Heverlee, Belgium), so only the area of need was incubated. Third, the glass was incubated with 10 μg/ml antibody (see table 4-1 for details) in PBS in an incubator at 37 ºC for 1h. Fourth, after washing with PBS (150mM NaCl, 10 mM PO_4^{3-}, pH 7.4), the remaining glass surface was blocked with 1% bovine serum albumin (BSA) in PBS for 30 min at 37 ºC in the incubator. Fifth, after washing with PBS, a coverslide rinsed with 70% ethanol was put on the microscope slide, using a second frame-shaped sheet of double sided tape (with a channel). Then, the flowcell with functionalized microscope slide was ready to be used.

Table 4-1. Antibodies used for surface functionalization

Antibody	*name*	*manufacturer*
Anti-CD6	αHu-CD6	BD Pharmingen
Anti-CD3	OKT3 or T3B	TIL, NCMLS Nijmegen
Anti-β1-integrin	TS2/16	TIL, NCMLS Nijmegen

Poly-L-lysine (PLL; Sigma-Aldrich, St. Louis, MO) coated microscope slides used for supported cell spreading experiments were prepared on cleaned microscope glasses with a circular boundary drawn by a DAKO pen. Slides were incubated with 0.01% PLL in PBS at 37 ºC in the incubator for at least 30 min. After washing with PBS, the microscope slides were either ready for use (bare PLL) or a second step followed for antibody coating. In the latter case, 10 μg/ml anti-CD6 antibody solution (see table 4-1) was incubated on the slide for 1h at 37 ºC in the incubator. After washing with PBS the microscope slide could be used for cell adhesion.

4.2.2 Cell preparation

Jurkat T-cells were stably transfected with CD6-RFP as described by Meddens (Meddens, 2009). Materials were bought from Invitrogen (Carlsbad, CA), unless stated otherwise. Jurkat cells and Jurkat-CD6-RFP cells were cultured in RPMI-1640 medium with phenol-red supplemented with 10% fetal bovine serum (FBS) and 1% antibioticum-antimyoticum (AA), at 37 ºC in an incubator with 5% CO_2. G418 was added to the Jurkat-CD6-RFP cell culture as a selection medium. Cells were counted and seeded at $4x10^5$ cells/ml in phenol-red free RPMI-1640 24h prior to the experiment. Before the experiment, cells were sorted with a FACS ARIA II (BD, Franklin Lakes, NJ), to select a population of cells that show high expression levels of CD6-RFP (approximately 5%). Cells with low expression levels did not show enough fluorescence for detailed imaging (data not shown). After sorting, the cells were incubated in an incubator in serum free RPMI-1640 (without phenol-red) with 1% AA and 25 mM Hepes, to buffer the CO_2 concentration in the medium. When stated in the experiment, dimethylsulfoxide (DMSO; Sigma) or Cytochalasin D (CytD) in DMSO was added to the cells at least 30 min prior to the experiment. Two different stock solutions of CytD were made. Experiments on anti-CD3 coated surfaces were performed with 5 μM CytD (1:1000 dilution of first stock solution), and on anti-CD6 coated surfaces 10 μM CytD (1:2000 dilution of second stock solution) was used.

4.2.3 Supported spreading assay and actin staining

To measure cell spreading in a supported spreading configuration and actin distribution in spread cells, we used the following protocol. First, cells were incubated for 5, 30 or 45 min on functionalized microscope glasses (section 4.2.1) in the incubator. All further steps were done at room temperature. After incubation, the samples were washed with PBS and the cells were fixed by incubation with a 3.7 % formaldehyde (Sigma) solution for 10 min. After washing with PBS the samples were either sealed or, in case of actin staining, permeabilized with 1% Triton X-100 (Sigma) in PBS for 5 min and washed again afterwards. Samples were stained with rhodamine phalloidin (Molecular Probes, Invitrogen) with a concentration of 5 µl à 6 µM in 200 µl PBS per coverslip for 20 min as described by the manufacturer. After washing, a droplet of MilliQ was placed on the sample and the sample was sealed with a coverslide and nail polish.

4.2.4 TIRF-OT Microscopy

The hybrid TIRF-OT setup described in chapter 2 was used to measure time series of cells adhering to a functionalized surface. Single images of fixed samples were taken with the TIRF microscope without using OT. Table 4-2 gives the main settings for the described experiments. The protocol for TIRF-OT experiments was as follows. First, the flowcell was prepared as described in section 4.2.1, and a syringe was connected to the inlet tube of the flowcell with a needle and an outlet tube was connected. Then, medium was flown with the syringe into the flowcell to fill it followed by medium with cells in volumes of ~ 50 µl each time. A cell was trapped with the OT (1064 nm; Millennia IR, SpectraPhysics, Newport, Irvine, CA) and lowered in the optical trap. Then, the objective was focussed onto the functionalized microscope slide and the TIRF illumination beam (ArKr, Coherent Inc., Santa Clara, CA) aligned parallel to the focal plane of the objective. Next, acquisition of the time series of images was started and the trapped cell was moved upwards to the glass surface, in steps of 1 µm and with a speed of ~0.5 µm/s. When the cell was in stable contact with the glass surface the trap was kept constant for 1-2 min before it was turned off. Cell contact was observed for ~ 1000 s, for untreated Jurkat-CD6-RFP cells, but for ~ 600 s for pre-treated Jurkat-CD6-RFP cells.

Table 4-2. Settings for TIRF-OT experiments

Setting	*Value*	*Remark*
568 nm laser intensity	~150 W/cm^2	Average intensity illuminated spot
1064 nm laser intensity	~500 mW	At back aperture of objective
Temperature stage	37 ºC	
Temperature objective	38.5 ºC	Not always connected
Angle of incidence	63.5 deg.	
Illumination time	100 ms	
EM gain RFP channel	250	REALgain
Measurement frequency	10, 1 or 0.33 Hz	1 Hz on default
Filters	Notch 568, 560 dichroic mirror, 593/40 band pass, 700 short pass	

4.2.5 FRAP measurements

Fluorescence recovery after photobleaching experiments were performed on a confocal microscope (Zeiss, Oberkochen, Germany), using the following protocol. Chambered cover glasses (Labtec, Thermo Fisher Scientific, Waltham, MA) were coated with either anti-CD6 or anti-β1-integrin as described in section 4.2.1. Jurkat-CD6-RFP cells were incubated on the functionalized surfaces in serum free medium for 30 min in the incubator and then positioned on the microscope. An objective heater (38.5 ºC) on a plan-apochromat 63x oil immersion objective (NA 1.4) was used, together with a heated stage (37.5 ºC; Harvard Instruments, Holliston, MA). Images (512*512 pixels) were acquired with 543 nm Helium-Neon laser (5 mW, Lasos Lasertechnik, Jena, Germany) light illumination using 20% illumination intensity, 1.6 μs/pixel and 1 images/s. Bleaching was done for ~30 s at full 543 nm intensity, after 5 images. Time series were analysed in ImageJ (http://rsbweb.nih.gov/ij/), setting a region of interest at the bleached area, at the background and one within the contact site at a non-bleached area. Further data processing was done using Origin (OriginLab, Northampton, MA). First, the fluorescence intensity at the bleached region of interest was background corrected. Then, the intensity at the non-bleached region of interest was used to correct for photobleaching. The method of Kapitza, as described by Erbe (Erbe, 2007), was used to fit the recovery curve. This was done by calculating $F_{inv} = F_0 - F(t)$, and then fitting F_{inv} with $A\left(1 - e^{\tau / t}\right) + B$, where F_0 is the measured fluorescence

intensity before bleaching, *F(t)* is the measured fluorescence over time (background and photobleaching corrected), τ is the characteristic diffusion time, and *A* and *B* are related to the mobile (x_m) and immobile fractions. The mobile fraction ($x_m = A/(A+B)$) and the diffusion constant ($D = w^2/4\tau$) were calculated, where *w* is the radius of the bleached area.

4.2.6 Data analysis TIRF images

TIRF images were analysed using DIPimage, a Matlab toolbox. The fluorescence images were segmented with isodata thresholding (as described in section 2.7), defining the contact site. Then, the contact size and the mean pixel intensity within the contact site were calculated. Since the program is forced to find a contact site, even before the Jurkat-CD6-RFP cell is in contact with the surface, the mean pixel intensity is giving approximately the background signal value in these timeframes. The time t = 0 s was determined as the time point where a step in mean intensity was observed, indicating a fluorescence signal was detected. The given mean intensity is background corrected and (if stated) normalized to the value at t = 0 s. If stated, correction for photobleaching of CD6-RFP was performed as described in Box 4.3.

4.3 Results and Discussion – Cell spreading

4.3.1 Cell spreading over time with TIRF-OT microscopy

We imaged the interaction of Jurkat-CD6-RFP cells with various functionalized surfaces. We used TIRF microscopy after bringing the cells in contact with the surface with OT to control the onset of interaction, as described in the Materials and Methods section. Fig. 4.1A shows TIRF images of CD6-RFP distributions at different time points after initiation of contact, measured at 1 Hz for 300 s and then at 0.33 Hz. After 1-2 min the OT were turned off; this did not result in visible decrease of contact size for cells in stable contact with the surface. The initial contact size of the cells for the three different coatings is similar. Over time, however, we see a difference in cell spreading: cells on anti-CD6 spread the most, but on anti-CD3 only little spreading can be observed. Since the transfected Jurkat-

CD6-RFP cells have very low CD3 expression (Box 4-4), this low spreading on anti-CD3 is probably caused by insufficient adhesion possibilities. On anti-β1-integrin functionalized surfaces we observe spreading, as described in reviews by (Hynes, 2002, van der Flier and Sonnenberg, 2001).

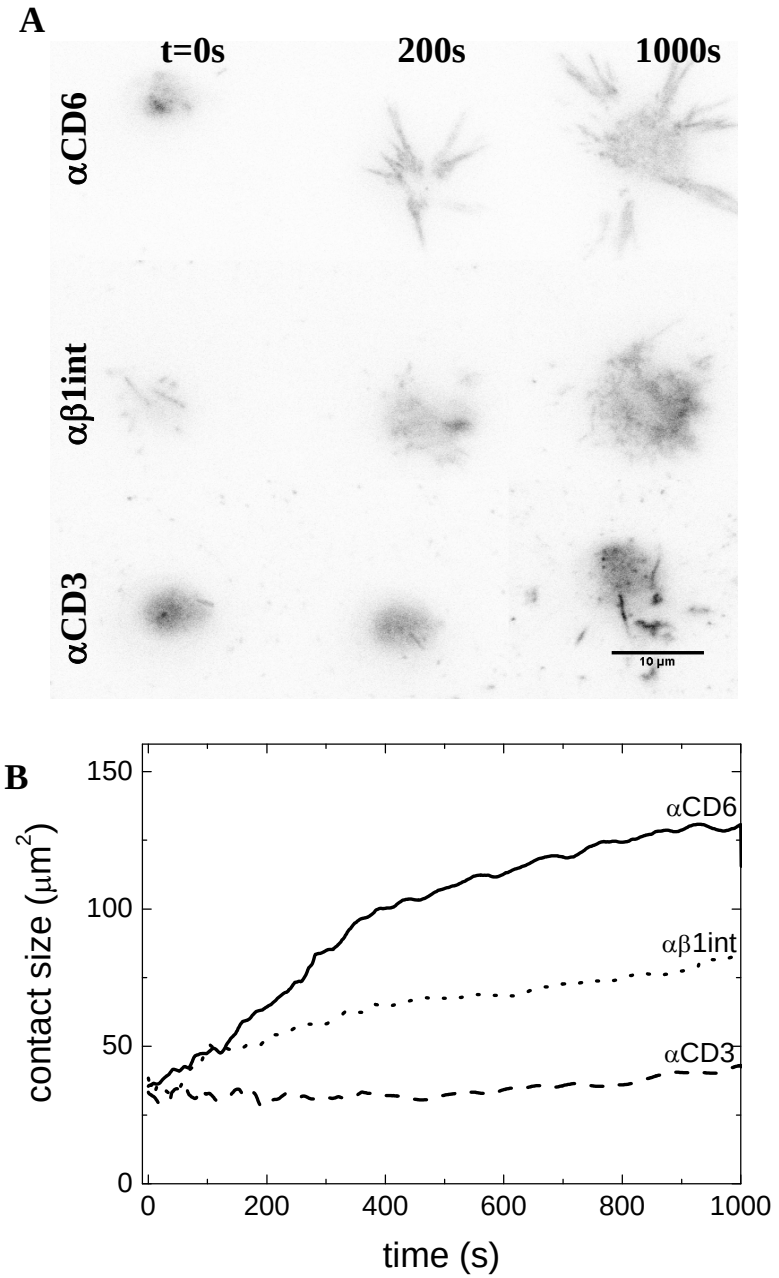

Fig. 4.1 Cell spreading over time of Jurkat-CD6-RFP cells on functionalized surfaces induced and observed by TIRF-OT microscopy
A. TIRF images at various time points after interaction with three different antibody coated surfaces, scale bar 10 µm, B. Contact size versus time for the three antibody functionalized substrates. Every curve represents an average of several cells (8 for anti(α)–CD6, 8 for anti-β1-integrin and 9 for anti-CD3).

Box 4-1. Validation CD6-RFP as contact size marker

To test whether CD6-RFP can be used as a valid marker of the contact size on non-anti-CD6 coated surfaces, we measured cell spreading on anti-CD3 with cells with an F18 membrane stain.

Materials and Methods

Jurkat-CD6-RFP cells were stained with F18 (Fluorescein isothiocyanate + octadecylamine; (Keller et al., 1977)). F18 was prepared as described by Keller. The working concentration should have an OD of 0.085, which we measured to be fulfilled for a stock solution, used 1:500 diluted. The concentration of this stock solution was calculated to be ~ 1 mM. Cells were incubated for app. 1h at 37 ºC and afterwards washed and put in serum-free RPMI-1640 medium (with 1% antibioticum-antimyoticum and 25 mM Hepes). Cell measurement with TIRF-OT was performed as described in section 4.2.4. Intensity of the 488 nm laser (Ar; SpectraPhysics, Newport) light for F18 illumination was ~ 30 W/cm^2, a 488 nm Notch filter and a 525/50 band pass filter were positioned in the detection path. Illumination of the RFP by 568 nm and the F18 by 488 nm was performed sequential to minimize crosstalk.

Results

Fig. B4-1 shows the contact size over time after data analysis of fluorescence TIRF images of CD6-RFP and F18. Here, t=0 s is the start of the experiment, the onset of interaction is a few seconds later. Both curves show a similar behaviour. Before the cell is in contact, there is a difference between the curves caused by the analysis software that is forced to find a cell (even when there is none). At t = 90 s and t=200 s the OT were turned off, which resulted in this case in cell loss and a difference in the measured contact size. Therefore, the OT were turned on again. The peak at t = 140 s is a result of refocusing. From the small difference between the contact size determined for both fluorescence markers, we can conclude that the RFP signal is a valid marker for the cell contact size.

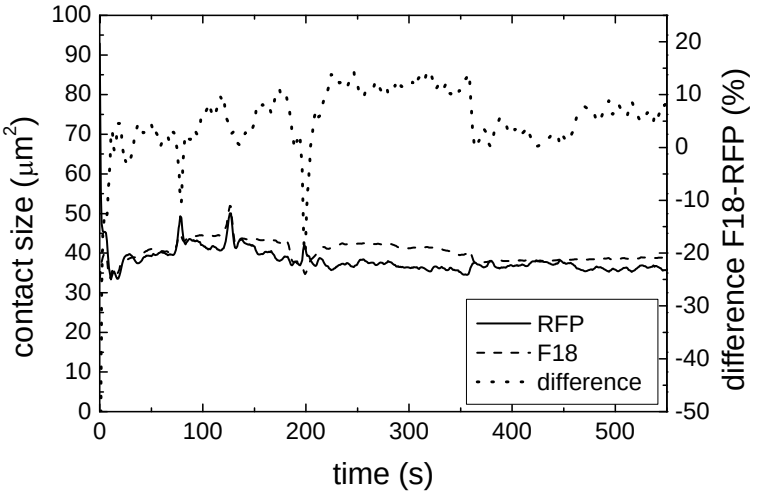

Fig. B4-1. Measured contact size of Jurkat-CD6-RFP cells on anti-CD3 using RFP and F18 fluorescence signals as a measure (left axis) and the difference between the determined contact sizes of both fluorescence signals (right axis).

To quantify cell spreading, we used the data analysis method described in section 2.7. Fig. 4.1B shows the contact size as a function of time after averaging over 8-9 cells per condition, as a quantitative measure for cell spreading dynamics. In Box 4-1 we show, using an independent membrane stain, that CD6-RFP fluorescence is a valid measure for contact size, even on non-CD6 coated surfaces. The increase in contact size over time demonstrates clearly that stimulation of CD6 results in spreading of Jurkat-CD6-RFP cells. Since the size of the stable contact site formed is much smaller than the total surface of the cell (which is ~ 800 μm^2 (Appendix B)), the measured contact size is realistic. Stimulation of CD3 does not lead to cell spreading in our experiments, and reveals a curve similar to that obtained for aspecific binding to BSA (Appendix C). Since cells do not know in advance what surface they will encounter, the initial contact size for all three surfaces is similar, indicating a correct data processing and segmentation of the fluorescence images. The spreading behaviour has a hyperbolic tangent shape, as described by Chamaraux et al. (2005) for spreading driven by actin polymerization (Box 4-2). This indicates that the actin cytoskeleton is involved in CD6 dynamics and spreading.

4.3.2 Actin cytoskeleton involvement in cell spreading

4.3.2.1 Distribution of the actin cytoskeleton in cell-surface interactions

To visualize the cytoskeleton, we stained the actin with rhodamine phalloidin and imaged the fluorescent actin with TIRF microscopy. Although the fluorescence of the rhodamine signal spectrally overlaps with the CD6-RFP signal, a large difference in signal intensity was observed. CD6-RFP was not visible without using the EM-gain of the CCD camera, in contrast to rhodamine fluorescence. Therefore, in samples stained with rhodamine, the CD6-RFP fluorescence can be neglected.

Fig. 4.2 shows TIRF images of fluorescent actin for different functionalized surfaces, taken at two different time points after initial contact. The images show that at the end stage (30+ min) the actin is polarized at the cell periphery, except on PLL coated glass slides where adhesion is mainly due to electrostatic interaction

Box 4-2. Cell spreading - fit

As described by Chamaraux (Chamaraux et al., 2005) cell spreading can be described with an hyperbolic tangent. The contact size (S) in Fig. 4.1B is fitted by $S = S_0 + (S_{end} - S_0)\tanh(\alpha t)$, with S_0 the contact size at t=0 s, and S_{end} the contact size when the cells are fully stretched. Fig. B4-2 shows the contact size over time on anti-CD6 (squares) and the fit to this data (line). The inset plots the data in a different manner, to demonstrate the validity of the fit ($T = \tanh^{-1}\left(\frac{S - S_0}{S_{end} - S_0}\right) = \alpha t$). From this figure we can conclude that the spreading behaviour of Jurkat-CD6-RFP cells on anti-CD6 can be described by a hyperbolic tangent. The fitted values are: S_0 = 26.7 ±0.5 μm^2; S_{end} = 125.7 ± 0.2 μm^2; α = 0.00229 ± 0.00002 s^{-1} (R^2 = 0.97047). This α corresponds to a characteristic time of ~ 435 s.

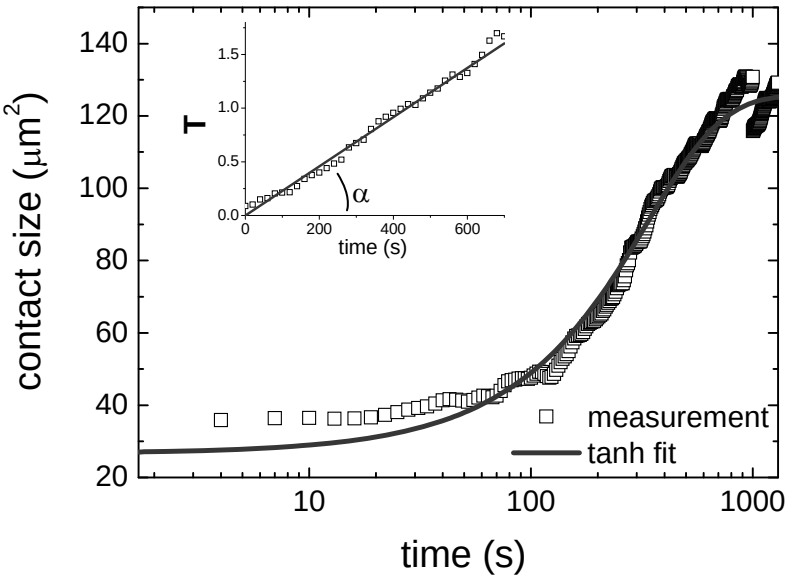

Fig. B4-2. Contact size over time for Jurkat-CD6-RFP cells (average of 8 cells) in contact with anti-CD6 functionalized surface, measurement (squares) and theoretical fit (line); inset: plot of T as a function of time, to demonstrate validity of fit

and not by active spreading due to cytoskeleton rearrangements. The images taken after 5 min show, however, a noticeable difference for an anti-CD6 coated surface compared to other surfaces: for anti-CD6 coated surfaces, we observe a clear actin polymerization process at the cell periphery. When we compare the last two conditions (PLL and PLL+anti-CD6), we see another difference after 30 min: on bare PLL there is a large contact site mainly due to electrostatic interactions (Hategan et al., 2004), but on anti-CD6 coated PLL the CD6 specific interactions, besides the electrostatic interactions, result in a different morphology and different actin distribution. Although, Bunnell *et al.* (2001) do not observe adhesion of Jurkat

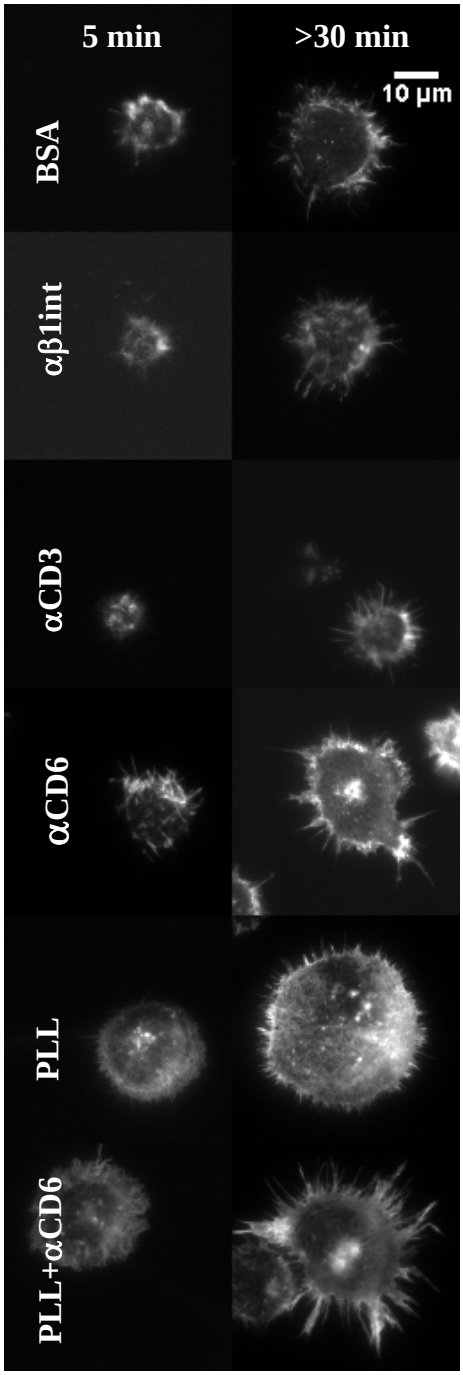

Fig. 4.2 Actin cytoskeleton in spreading Jurkat-CD6-RFP cells

TIRF images of fluorescently labelled actin in Jurkat-CD6-RFP cells that were fixed after 5 or 30-45 min in contact with a functionalized surface. Intensity scale varies between the images.

cells on PLL, our results are consistent with those of others (Marjolein Meddens, oral communication).

On anti-CD3 we even observe a smaller contact site than on BSA, where the diameter of the contact site is approximately the diameter of the cell. Possibly, this small contact site is caused by too few available binding sites on the cell, so the cell can not attach to the surface. On anti-CD3, a ring-shaped structure of actin at the cell periphery has been described (Bunnell *et al.,* 2001, and Parsey and Lewis, 1993), especially visible after 5 min of contact. Since we have low CD3 expression, we do not see the described ring of actin polymerization for cells on anti-CD3 surfaces. Using TIRF microscopy, we observe an actin reorganisation on anti-CD6 functionalized surfaces after 5 min, which might appear in widefield fluorescence microscopy as a ring structure.

Together, these images show that on anti-CD6 functionalized surfaces there is an active process of cytoskeleton rearrangements, starting at early time points after interaction, which is observed less on BSA, anti-β1-integrin or PLL.

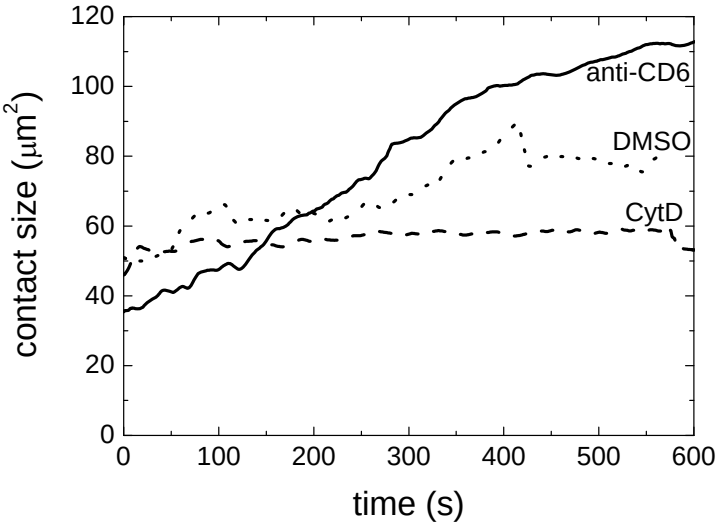

Fig. 4.3 Spreading dynamics upon cytoskeleton disruption Contact size versus time on anti-CD6, anti-CD6 with DMSO (control; solvent of CytD) and anti-CD6 with Cytochalasin D (averaged over 8, 5, and 9 cells respectively)

4.3.2.2 Effect of cytoskeleton disruption on cell spreading dynamics

To further investigate the involvement of the cytoskeleton, we disrupted the cytoskeleton with 10 μM Cytochalasin D (CytD) and monitored cell adhesion to functionalized surfaces over time with hybrid TIRF-OT microscopy. Fig. 4.3 shows the contact size over time for three different situations: on an anti-CD6 coated surface without cytoskeleton disruption, and on anti-CD6 with DMSO, on anti-CD6 with CytD.

The measurement on anti-CD6 with DMSO is a control experiment, since CytD is dissolved in DMSO. Although we observe a smaller spreading for the DMSO treated cells than for the non-treated cells, the characteristic time after fitting the cell spreading of DMSO pre-treated cells with a hyperbolic tangent (not shown) is similar to the untreated cells. Furthermore, the concentration of DMSO used is well described in literature and (to the best of our knowledge) does not influence cell proliferation, adhesion and actin polymerization. We assume that the decrease in cell spreading is due to (small) changes in the cell condition after DMSO treatment in combination with the forces on the cell in our hanging measurement configuration, as will be subject to more extensive analysis in the next section. Focussing on the CytD treated cells on anti-CD6, we can clearly observe that disruption of the cytoskeleton completely diminishes cell spreading, leading us to conclude that the actin cytoskeleton is involved in CD6-induced cell spreading.

4.3.3 Cell spreading in supported orientation

To compare our previous experiments with generally used measurement configurations and to quantify the influence of DMSO treatment of the cells more extensively, we let cells settle (by gravity) on a functionalized microscope glass in an incubator. After 45 min, cells were fixed and afterwards imaged with TIRF microscopy. Fig. 4.4 shows TIRF images of fixed non-treated and pre-treated Jurkat-CD6-RFP cells in contact with various coated surfaces for 45 min. Cells clearly spread best on an anti-CD6 coated surface, as expected from our TIRF-OT experiments. The cells hardly stick on anti-CD3, which results in visualisation of only few cells with small contact sites. Furthermore, pre-treatment with DMSO does not show a clear effect on cell morphology and spreading, as opposed to pre-treatment with Cytochalasin D. The observed protrusions from the cells that were treated with CytD have been described as arborisation, characterized by the appearance of multiple, thin, branch-like projections emanating from a retracting pseudopod (Parsey and Lewis, 1993).

In Fig. 4.5, we show the average final contact size for various cell conditions and functionalized surfaces in a supported and a hanging measurement configuration. A large cell-to-cell variation is observed; the error bars give the standard deviation. Three differences due to the measurement orientation can be

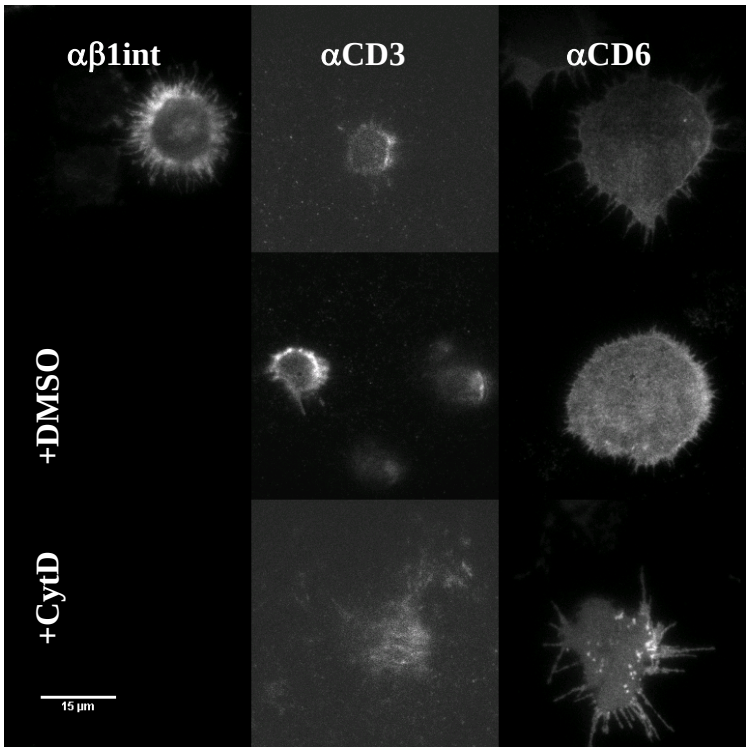

Fig. 4.4 Spreading of Jurkat-CD6-RFP cells in a supported configuration
TIRF images of Jurkat-CD6-RFP cells fixed after 45 min of contact in a supported configuration. The intensity scales vary between the images.

observed. In the first place, the overall contact size is much smaller in the hanging situation. This is most likely caused by the gravitational force on the cells. In the second place, when we compare relative numbers (right axis, dashed bars), the decrease in contact size for cytoskeleton disruption on anti-CD6 is more profound in the hanging than in the supported orientation. Disruption of the cytoskeleton on anti-CD3 even gives an increase in contact size in the supported orientation. This last observation can be understood by the fact that the cytoskeleton gives the cell its shape, and disruption of the cytoskeleton makes the cell less stiff, so that it sags on the glass surface. Finally, we note that in the supported, conventional situation we observe no effect of DMSO, in complete agreement with the literature. However, for the hanging measurement orientation, we do see a decrease in the contact size, caused by cellular changes in combination with the forces exerted on the cell in the hanging configuration.

Together, these observations show that our hanging measurement configuration is more sensitive to cellular changes than conventional microscopy

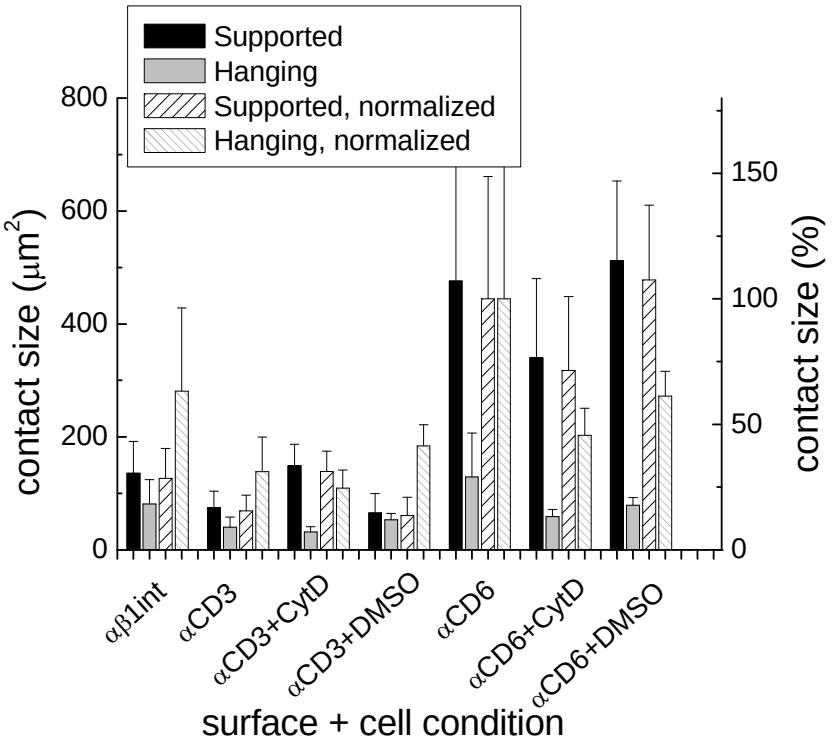

Fig. 4.5 Supported versus hanging spreading
Contact size (mean and standard deviation) of cells in stable contact with various functionalized surfaces and for different conditions. The solid bars show the contact size in μm^2 (left axis) for the supported and hanging situation as an average over different cells, whereas the dashed bars give the relative contact size compared to an anti-CD6 surface (100%) on the right axis.

One-way ANOVA analysis was used to compare the different experimental settings. This revealed that the following populations are statistically significantly ($p \leq 0.05$) and very significantly (**, $p \leq 0.01$) different from each other:
- Supported: αCD3 vs αCD6 (**), αCD3 vs αβ1int, αCD3 vs αCD3+CytD(**), αCD6 vs αβ1int
- Hanging: αCD3 vs αCD6 (**), αCD3 vs αβ1int, αCD6 vs αCD6+CytD

measurement configurations. This results in a different spreading behaviour for DMSO pre-treated cells.

4.3.4 Conclusions and Discussion – Cell spreading

In the previous sections, we have investigated the role of CD6 in cell spreading and the influence of the cytoskeleton on this spreading. We can conclude that stimulation of CD6 induces cell spreading (Fig. 4.1). The spreading on anti-CD6 is larger than on anti-β1-integrin, a molecule involved in cell adhesion, which we included as a positive control for cell spreading. Although the absolute size of the contact sites might be influenced by the surface concentration of the antibody coatings and number of CD6 and β1-integrin on the cell membrane, the large spreading on anti-CD6 points towards a strong cellular response upon CD6 stimulation, to increase and stabilize the contact size. Combining this with the notion that CD6 has a contact stabilizing function (Zimmerman et al., 2006), we hypothesize that CD6 exert this function by expanding the number of CD6-ligand-bindings, for example by increasing the size of the contact site.

The characteristic time of spreading, calculated with the model of Chamaraux et al. (2005), is 435 s (Box 4-2), which is on the same order of magnitude as the characteristic time of K562-ALCAM-GFP cells on CD6 (chapter 3). Since the characteristic time is influenced by many variable, including the type of substrate and cell, the number of interacting molecules and the forces on the cell influencing the actin polymerization speed (Li et al., 2010), it is difficult to draw conclusions based on the absolute magnitude of the characteristic time. However, the characteristic time can be used to compare different experimental situations, like the hanging versus the supported configuration and, in this case, K562-ALCAM-GFP cells on CD6 or Jurkat-CD6-RFP cells on anti-CD6. The similarity in characteristic time observed here might indicate that similar processes play a role in both cells, which in cell-cell interactions might result in the growing of the contact site at similar speeds as for cell-surface interactions. This hypothesis would be interesting to examine in cell-cell interaction experiments. Furthermore, we observe a redistribution of the actin cytoskeleton upon CD6 stimulation (Fig. 4.2). Together with the finding that cytoskeleton disruption impairs cell spreading (Fig. 4.3), this demonstrates that the actin cytoskeleton is involved in CD6-induced cell spreading.

The mechanism may be mediated by the previously described interaction of CD6 with Syntenin-1, which is able to bind cytoskeletal proteins (Gimferrer et al., 2005), although from the results presented here, we cannot conclude anything on the existence of a physical linkage between CD6 and the cytoskeleton.

In order to explain the influence of DMSO treatment on the spreading of cells, we showed that our hanging measurement configuration is more sensitive to cellular changes than the generally used supported configuration. Therefore, we measured smaller contact sizes and larger relative changes upon cytoskeleton disruption (Fig. 4.5). The reason for this higher sensitivity to cellular changes lies in the direction of the forces, as depicted in Fig. 4.6. For the normal, supported configuration, the gravitational force is in the direction of the binding surface. For the hanging configuration (which is the case for TIRF-OT measurements), the gravitational force is in the direction opposite to the binding surface. Although in the latter configuration the force of the OT is also present, this will usually not (totally) compensate for the gravitational force for two reasons. First, F_{OT} can point in the opposite direction, but also in the same direction as F_g. And, second, the optical trap force acts only on a particle in the cell, while F_g acts on the whole cell. The optical force will therefore only be able to hold a part of the cell connected to the glass surface. Once this part of the cell is stably attached, the optical trapping

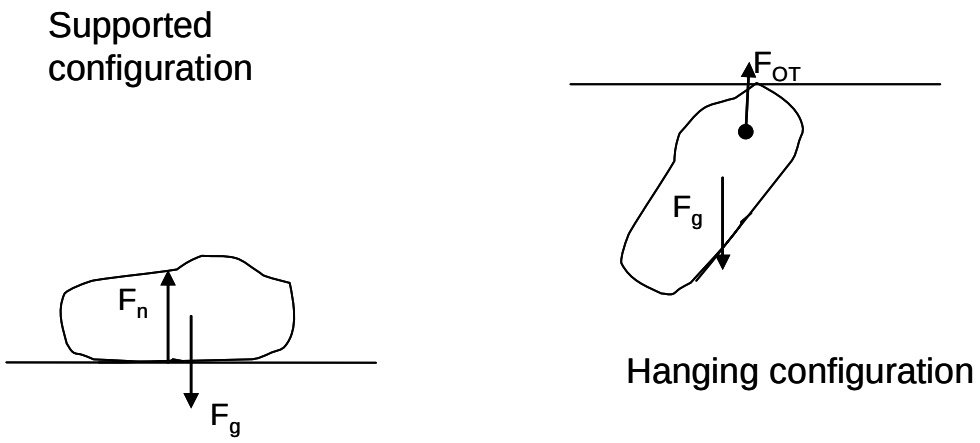

Fig. 4.6 Configurations of cell spreading

Forces on cells in the supported and hanging configuration and B, at t=0s. In the supported configuration, F_n and F_g have the same size, but opposite direction, resulting in a net force F = 0 N. In the hanging configuration, the direction of F_{OT} can be either upwards or downwards, acting on a 'particle' in the cell. Therefore, a net force will be generally directed downwards. In the hanging configuration the spreading occurs under external loading of the cell.

force does not add to the contact stability anymore. Therefore, turning the OT off after 1-2 min does not influence the contact size anymore.

A situation in which the higher sensitivity to cellular changes of the hanging configuration results in additional information is demonstrated in the control measurement with DMSO pre-treated cells. In the supported configuration, no effect of DMSO could be observed, but in the hanging configuration a smaller spreading was observed. Since DMSO influences the stability of membrane pores (Notman et al., 2006), a possible explanation is that the cell is less able or willing to spread while being hindered by the gravitational force. The observation that cell spreading is strongly reduced can also be caused by the reduced recruitment as observed in the next section. When this DMSO effect is CD6-specific, this might hint towards a possible role for membrane lipid composition on CD6 related processes. It is also possible that the DMSO effect is a general phenomenon (not specific for CD6 stimulation). In that case, one should be very careful in concluding that DMSO has no effect on cells. Obviously, the effect of DMSO on cells will be concentration dependent, however, for the supported experiments we used a generally used concentration of 0.1% and we did not observe an effect, whereas for hanging configuration we used a lower concentration (0.05%) and did observe an effect of DMSO.

4.4 Results and Discussion – CD6 recruitment

To quantify CD6 distribution, we monitored the fluorescence intensity of CD6-RFP in the TIRF images. The fluorescence signal intensity at a position ($I_{fl}(x,y)$) depends on many different factors, like excitation intensity (I_{exc}), exposure time (t_{exp}), protein concentration in the measurement volume (n) and, in case of TIRF illumination, distance between surface and proteins (z) and the penetration depth (d_p); $I_{fl}(x,y) \propto I_{exc} t_{exp} n \cdot e^{-\frac{z}{d_p}}$. In order to draw conclusions on the CD6 concentration and distribution at the contact site for different surface functionalization and cell treatments, we kept all the mentioned factors constant throughout the experiments. Here, we describe CD6 distribution and recruitment based on the CD6-RFP signal intensity at the contact site.

4.4.1 Recruitment of CD6 in Jurkat-CD6-RFP cells on anti-CD6

We measured the mean fluorescence intensity per unit area at the contact site of Jurkat-CD6-RFP cells in contact with an anti-CD6 coated surface, as described in section 4.2.6. The intensities are background corrected and averaged over multiple cells per condition. Furthermore, we assumed that a CD6-RFP molecule at the contact site of the cell will interact with an anti-CD6 molecule and will stay at the contact site. Therefore, this CD6-RFP molecule will be subject to photobleaching. Photobleaching of RFP in Jurkat-CD6-RFP was measured on poly-L-lysine adhered cells in a final stage, as described in Box 4-3. We corrected for this photobleaching, and finally normalized the curves to the t = 0 s point. Fig. 4.7A shows the resulting normalized mean fluorescence intensity curves over time, for untreated and pre-treated (DMSO or DMSO+CytD) Jurkat-CD6-RFP cells in contact with anti-CD6 (same data set as Fig. 4.3). No effect of turning of the OT after 1-2 min could be observed. For untreated Jurkat-CD6-RFP cells, a linear increase in average intensity can be observed. This demonstrates that on anti-CD6 substrates the CD6-RFP is recruited towards the contact site. After 500 s the CD6-RFP density (the amount of molecules per unit area) at the contact is ~18 times higher. When the cytoskeleton is disrupted with CytD, this recruitment is completely abolished, indicating that the

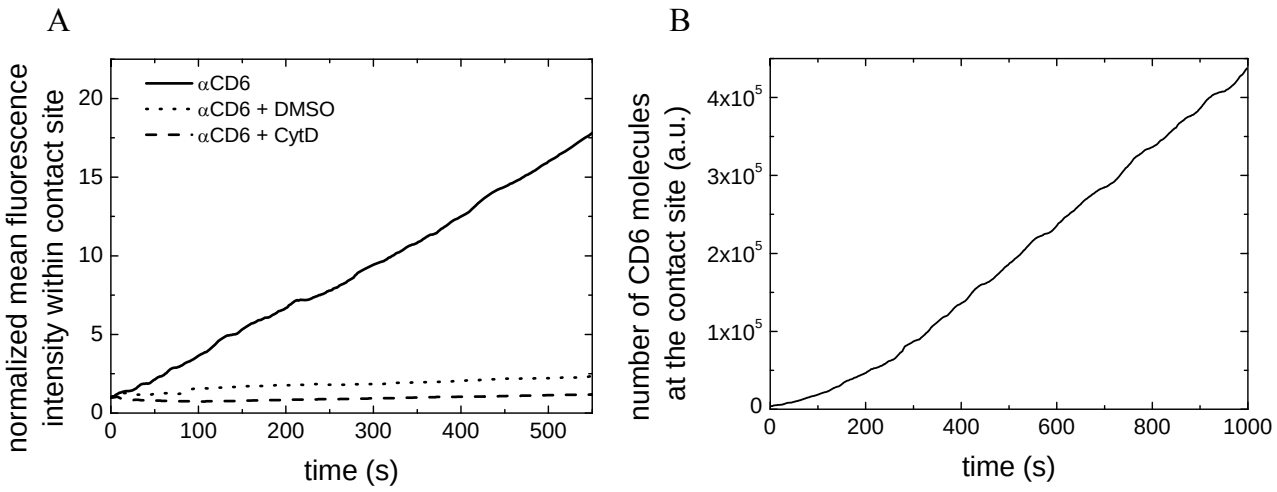

Fig. 4.7 CD6-RFP recruitment on anti-CD6
Jurkat-CD6-RFP cells on anti-CD6, A. mean fluorescence intensity of untreated and pre-treated cells, as a measure for CD6-RFP recruitment; B. total fluorescence intensity at the contact site as a measure for the number of molecules therein.

Box 4-3. RFP bleaching correction

To measure the bleaching characteristics of CD6-RFP in our experiments, we performed an experiment on PLL.

Materials and Methods

A microscope glass was incubated with PLL for 20 min in the incubator. After washing with PBS Jurkat-CD6-RFP cells were added on the functionalized glass surface. After 5 min in the incubator the samples were washed with PBS and a coverslip was added, using double sided tape with a channel cut out of it as a spacer. Measurements were performed on the TIRF microscope with the settings as described in Table 4-2, in frame transfer mode (10 Hz) and on room temperature. Hardly any mobility of the fluorescent CD6 was observed. The images were segmented as described in section 4.2.5. The mean fluorescence intensity was corrected for the background and normalized to the first point.

Results

The background-corrected and normalized mean intensity data points of 13 cells were averaged; this average is shown in Fig. B4-3. Photobleaching can be characterized with a exponential decay (Axelrod et al., 1976), therefore we fitted an exponential decay to the data, as is also shown in Fig. B4-3. A double exponential fitted well to the data, indicating that we have at least two populations of mRFP in our sample. We used the obtained bleaching characteristic to compensate the mean fluorescence intensity data from the contact site and calculated the recruitment of CD6-RFP to the contact site in an iterative manner. We assumed that diffusion out of the contact site can be neglected, based on the size of contact site compared to the diffusion constant (~0.1 $\mu m^2/s$. section 4.4.2), then $r(i) = I(t_i) - I(t_{i-1}) \cdot \beta$, where *r(i)* is the recruitment in the period Δt ($=t_i-t_{i-1}$), *i* the frame number of the recorded image, and β is the non-bleached fraction in a period Δt (based on Fig. B4-3 determined to be 0.995). The total recruitment (*R*) over time is then given by

$$R(t) = \sum_{i=0}^{t_i} r(i).$$

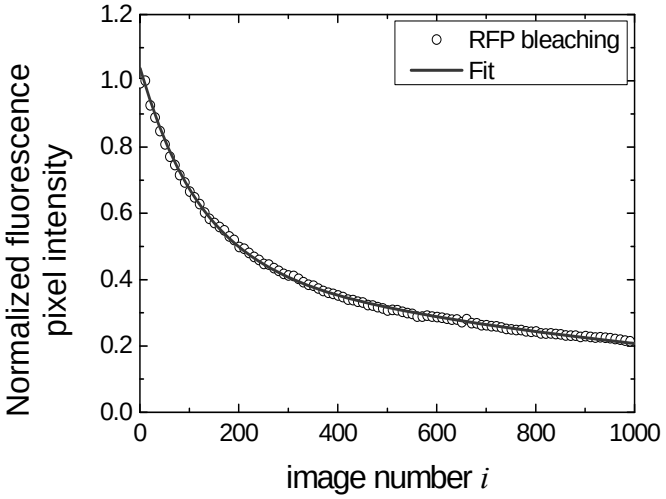

Fig. B4-3.
Fluorescence intensity versus number of collected images, experimental data (circles) and fit (line).
Fit with y=A1*exp(-x/t1)+ A2*exp(-x/t2), which gave A1=0.586±0.003, t1=119±1, A2=0.457±0.003,t2=1267±15 (with R^2= 0.99785)

cytoskeleton is involved in CD6-RFP recruitment. However, the control experiments of cells pre-treated with DMSO also show a much lower recruitment. Therefore, it is currently impossible to distinguish between the effect of DMSO and CytD treatment. A possible reason for this lower recruitment in the case of DMSO treatment can be the disturbance of the membrane integrity, as is also described in section 4.3.4 for cellular spreading. Since no spreading and recruitment was observed during the measurements with DMSO and CytD pre-treated cells, these experiments were only performed till ~550 s, whereas undisturbed cells were monitored for ~1000s. For DMSO or CytD pre-treated cells on anti-CD3, similar results were obtained (data not shown).

Fig. 4.7B shows the total number of CD6-RFP molecules at the contact site for untreated cells, calculated by multiplying CD6-RFP density (Fig. 4.7A) with cell spreading (Fig. 4.1B). This graph shows that on short timescales recruitment has a more pronounced effect on increasing the total number of CD6-RFP molecules in the contact site than cell spreading. Furthermore, the number of CD6-RFP molecules is increasing for the whole period of the measurement, although spreading is mainly observed in the first ~500 s (Fig. 4.1B). However, on longer timescales, possible effects like overcorrection for photobleaching result in a lower accuracy in these data points.

Since the data of CD6 recruitment upon cytoskeleton disruption was inconclusive, we investigated whether the recruitment was an active process with a second method. This method investigated whether the observed CD6-RFP recruitment is limited by the number of available binding sites of anti-CD6 on the glass surface compared to the number of CD6 proteins on the cell. Both numbers were determined quantitatively. First, quantitative FACS experiments determined the number of CD6 proteins on Jurkat-CD6-RFP cells (Box 4-4). This measurement revealed a CD6-RFP expression on the cell surface of ~14 molecules/μm^2, assuming all CD6 proteins at the cell surface bound one antibody; this is in the same order of magnitude to the described expression of the membrane molecule CD2 (60-120 molecules/μm^2, (Zhu et al., 2007)). Second, we measured the amount of anti-CD6 at the surface by interferometry (Box 4-5). This revealed an anti-CD6 coverage of the microscope glass of ~7 x 10^1 molecules/μm^2, which is difficult to compare to other situations since this parameter is usually not described; however,

Box 4-4. CD3 and CD6 labelled FACS experiments

To measure and count the CD6 and CD3 expression of the cells, flow cytometry experiments were performed on stained samples.

Materials and Methods

All steps below were performed on ice. Cells were washed twice with PBA (1% BSA in PBS) and distributed in tubes with $1x10^6$ cells/100 μl in PBA. As required by the manufacturer, we added 20 μl of stained antibody solution per tube for 30 min (see table 4B-4 for details of the antibodies). The cells were washed twice with PBS and resuspended in 0.5 ml PBA. Afterwards, they were analyzed directly by flow cytometry with the FACS ARIA II (BD).

Antibody	*type*	*Manufacturer*
Anti-CD6-FITC	mIgG1, clone M-T605	BD Pharmingen
mIgG1-FITC	Isotype control	BD Pharmingen
Anti-CD3-FITC	mIgG2a, clone HIT3a	BioLegend, San Diego, CA

Table B4-4. Antibodies used in cell labelling for FACS analysis

Results

Fig. B4-4 shows a histogram of the fluorescence intensity in the FITC channel for untransfected Jurkat cells (A) and transfected Jurkat-CD6-RFP cells (B) stained for CD3. As can be seen, the majority (~ 70 %) of untransfected Jurkat cells is CD3 positive. However, for the transfected cells CD3 expression diminishes to (almost) zero. With quantitative statistical analysis on the FITC stained cells, based on calibration described in App. 4A, we were able to calculate that the average number of CD3 (and below CD6) molecules on a cell surface, assuming that all molecules of interest were bound to exactly one antibody. For untransfected CD3-positive Jurkat cells, this was ~$1.0\ x10^4$; while for the Jurkat-CD6-RFP population that is sorted for TIRF-OT experiments, the expression goes down to ~$1.4x10^2$ CD3 molecules per cell. Since no isotype control was available, we measured three different types of antibodies on two different days to confirm the result (data not shown).

Furthermore, Fig. B4-4 shows a histogram of the fluorescence intensity for unstained cells, the isotype control and the CD6-FITC staining for both the untransfected (C) and transfected (D) Jurkat cells. Afterwards, this was quantified based on the calibration described in App. 4A. Four interesting conclusions were drawn based on these CD6-measurements:

- Transfection with CD6-RFP increases CD6 expression. A 15-fold increase of CD6 expression at Jurkat-CD6-RFP cells was detected compared to untransfected Jurkat cells ($7.7x10^2$ vs. $1.1x10^4$ molecules/cell).
- All Jurkat cells express CD6, as opposed to the CD3 expression.
- The distribution in the amount of CD6 on sorted Jurkat-CD6-RFP cells compared to all Jurkat-CD6-RFP cells is similar (data not shown). This indicates that upon increased CD6-RFP expression the expression of endogenous CD6 lowers, so CD6-RFP replaces CD6.
- We have ~$1.1x10^4$ molecules/Jurkat-CD6-RFP cell, which corresponds to (using a measured cell size of 16 μm, App. 4B) ~14 molecules/μm^2 on the cell membrane.

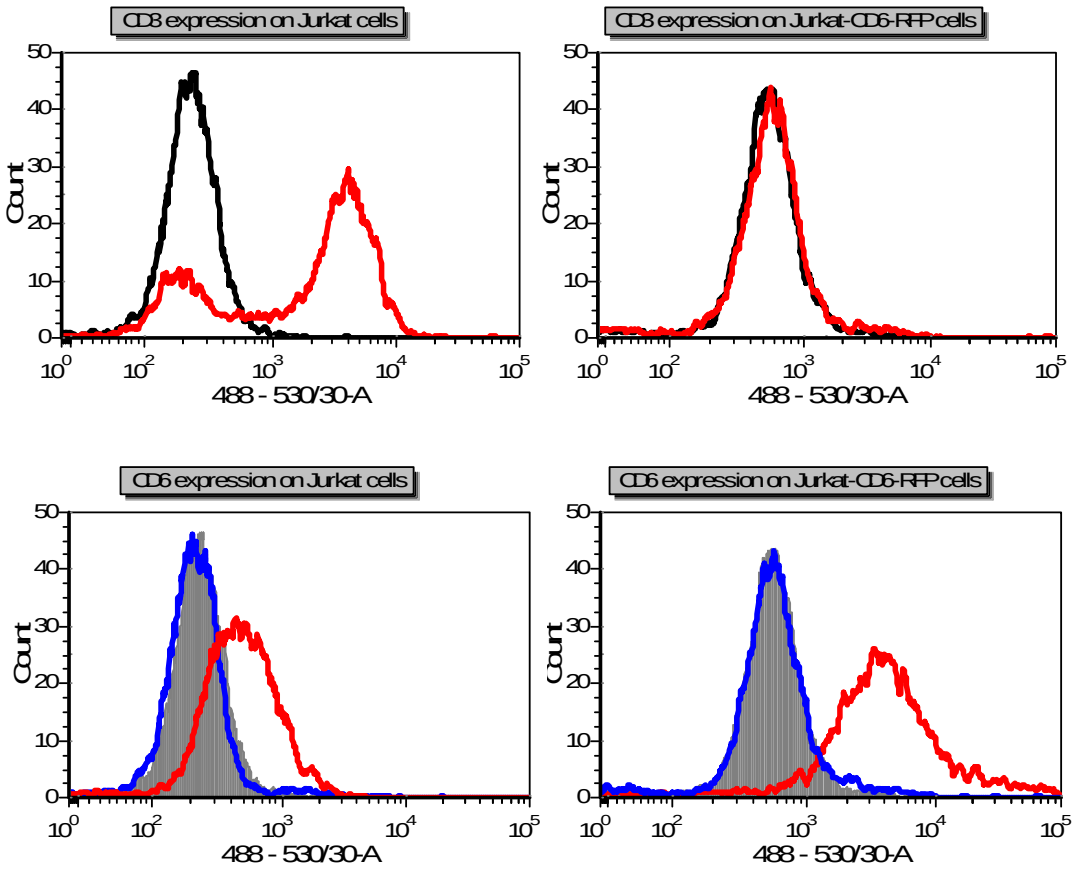

Fig. B4-4. Histogram of fluorescence intensity distribution on transfected and untransfected Jurkat cells. A+B: fluorescence of the unstained sample (black), and fluorescence signal of the sample stained with a FITC anti-CD3 antibody (red). C+D: fluorescence of the unstained sample (gray fill), the isotype control (blue) and sample stained with a FITC anti-CD6 antibody (red).

the method is sound and the result is therefore most likely in the right order of magnitude. A strong recruitment (>5-fold increase) of CD6 might therefore result in unbound CD6-RFP at the contact site. Since we observe > 5-fold increase in CD6-RFP concentration (Fig. 4.7A), this indicates that the recruitment of CD6 is not limited by the amount of available binding sites at the surface. Only when the antibody coverage on the glass slide is more than four times larger than measured, is it likely that the observed recruitment of CD6-RFP on anti-CD6 (Fig. 4.7A) could be caused by a passive process like diffusion. However, the data points towards an active process.

4.4.2 Diffusion of CD6-RFP

Recruitment of CD6 may not only be due to active processes in which the cytoskeleton is involved, but might also be influenced by CD6-RFP diffusion on the cell membrane. We used fluorescence recovery after photobleaching (FRAP) experiments to determine the diffusion of CD6-RFP on the cell membrane. In a FRAP experiment, a region of interest on the cell is illuminated with high intensity laser power to photobleach the fluorophores in this region. The recovery of

Box 4-5. Measuring surface functionalization with interferometry

A Young interferometer experiment was performed to measure the surface coverage by the antibody. Binding of molecules to the sensor surface results in a change in refractive index. Assuming a single uniform layer and using know bulk characteristics of molecules, the measured phase change in the interferometer can be converted via a refractive index change into a number of molecules bound to the sensor surface.

Materials and Methods

We used $S_{13}N_4$ waveguides on a home built Young interferometer (Ymeti, 2004). Antibody incubation with 10 μg/ml anti-CD6 (BD Pharmingen) was at room temperature under low flow (32 μl/min) for ~30 min. Before and after incubation and in the control channels PBS solution was flown. All solutions were degassed.

Results

Fig. 4C shows the phase change measured by the interferometer due to adhesion of anti-CD6 on the sensor surface corrected for the drift in the measurement channel. The measured phase change due to adhesion of anti-CD6 is 0.07 fringes.

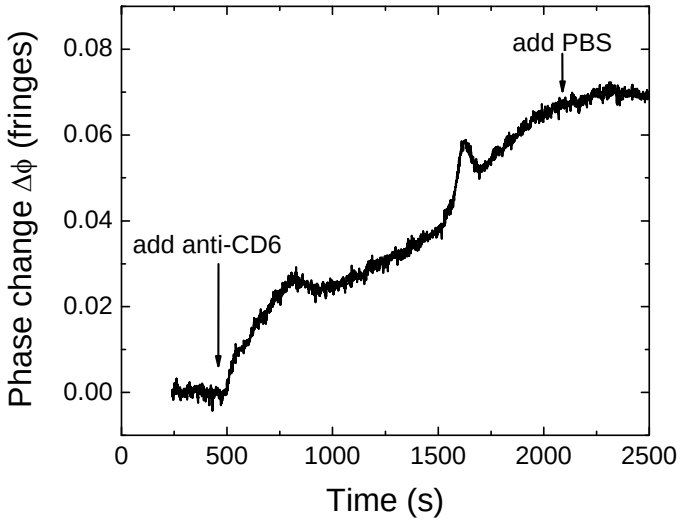

Fig. B4-5. Phase change in interferometer due to antibody binding to sensor surface. Measured $\Delta\Phi_{anti\text{-}CD6} = 7 \times 10^{-2}$ fringes

Using Eq. B4-5a and B4-5b, this can be converted to number of molecules per surface area (Ymeti, 2004).

$$\frac{\Delta m}{A}\left(\frac{ng}{mm^2}\right) = 0.6 \cdot \Delta d_l(nm) \qquad \text{Eq. B4-5a}$$

$$\Delta d_l = \frac{\lambda}{l}\left(\frac{\partial N_{eff}}{\partial d_l}\right)^{-1} \cdot \Delta\varphi \qquad \text{Eq. B4-5b}$$

Where l is channel length ($4*10^{-3}$ m), λ is the wavelength of the used laser light (647 nm), $\Delta\varphi$ is the measured phase change caused by layer formation (in fringes), and $\left(\frac{\partial N_{eff}}{\partial d_l}\right)^{-1}$ is the sensitivity coefficient of the effective refractive index of the waveguide with respect to the thickness of the layer grown on the sensor surface (based on (Ymeti, 2004) estimated at $(\sim 2.45*10^{-3})^{-1}$).

Since the measured phase change is 7 x 10^{-2} fringes, we have a surface coverage of ~7 x 10^{1} molecules/μm^2.

To test the functionality of the antibodies on the surface, we blocked the surface for aspecific interaction with a 1% BSA solution after antibody coating, and then added a cell lysate of Jurkat-CD6-RFP cells (lysis performed with 1% Igepal CA630, Sigma). From the measured phase change due to the adhesion of molecules in this cell lysate solution, we calculated the number of CD6-RFP molecules bound. Assuming only CD6-RFP molecules bound to antibody functionalized surface, this gave a similar surface coverage of CD6-RFP molecules as for anti-CD6 molecules (data not shown).

fluorescence intensity within the spot is measured and analysed to calculate the diffusion constant and mobile fraction by fitting of the data as described in section 4.2.5. Fig. 4.8 shows the fluorescence intensity in the region of interest for a Jurkat-CD6-RFP cell on anti-CD6 or on anti-β1-integrin. Bleaching was done from t = 5 s to t = 35 s, so total bleaching time is 30s, which resulted in a bleaching of 50% of the fluorescence. We corrected the data for the background signal and photobleaching. Fitting, as described in the materials and methods, revealed the following mobile fractions (x_m) and diffusion constants (D), averaged for 2 cells each:

anti-CD6	x_m = 94±6 %	D = 0.025±0.006 μm^2/s
anti-β1-integrin	x_m = 55±10 %,	D = 0.12±0.01 μm^2/s

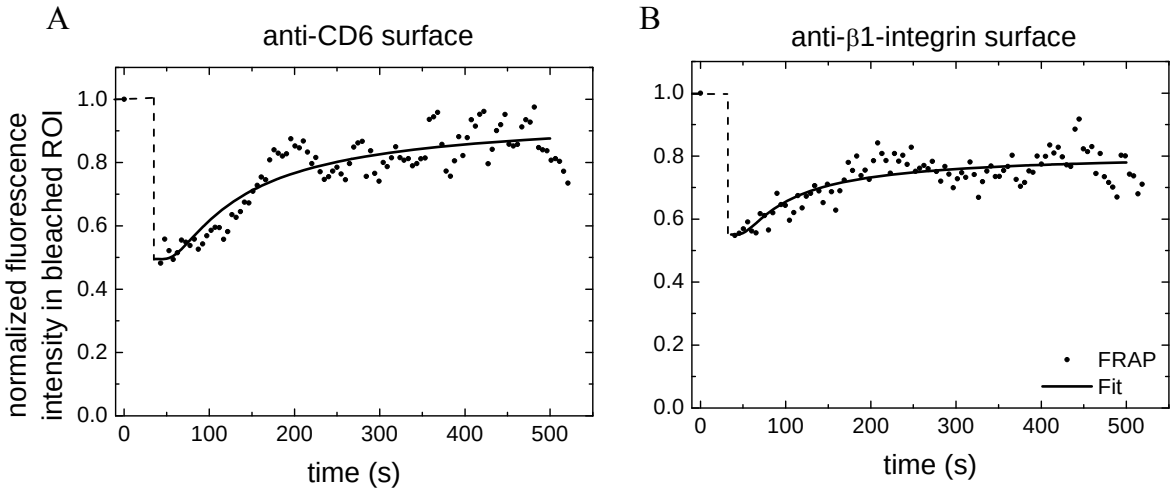

Fig. 4.8 FRAP experiment to determine CD6-RFP diffusion
Fluorescence signal of CD6-RFP in the region of interest at the contact site pre- and post-bleaching, on anti-CD6 (A) or on anti-β1-integrin (B). Signal is fitted with an exponential function as described in section 4.2.5.

Although we measured only on two cells per substrate, the diffusion constants of CD6-RFP are in the same order of magnitude as for other membrane molecules like LFA-1 (Diez-Ahedo et al., 2009), supporting the credibility of our results.

The mobile fraction on anti-CD6 suggests, assuming a stable, high affinity bond between CD6 and anti-CD6, that an excess of CD6-RFP is recruited towards the contact site, and that the number of bound CD6 proteins can be neglected with respect to the number of available unbound molecules. Since we have shown that the number of CD6 and anti-CD6 molecules are on the same order of magnitude (Box 4-4 and 4-5), and the recruitment of CD6 towards the contact site is significant (Fig. 4.7), this result supports the notion that CD6 recruitment is an active process.

4.4.3 CD6 recruitment on non-CD6 specific functionalized surfaces

To investigate the specificity of CD6 recruitment, we measured the fluorescence intensity over time for Jurkat-CD6-RFP cells in contact with three different functionalized surfaces, similar to the experiment described in section 4.4.1. Fig. 4.9 shows the mean fluorescence intensity per unit area over time, for anti-CD6, anti-CD3 and anti-β1-integrin surfaces. The anti-β1-integrin surface coating was chosen, because no relation has been described between β1-integrin

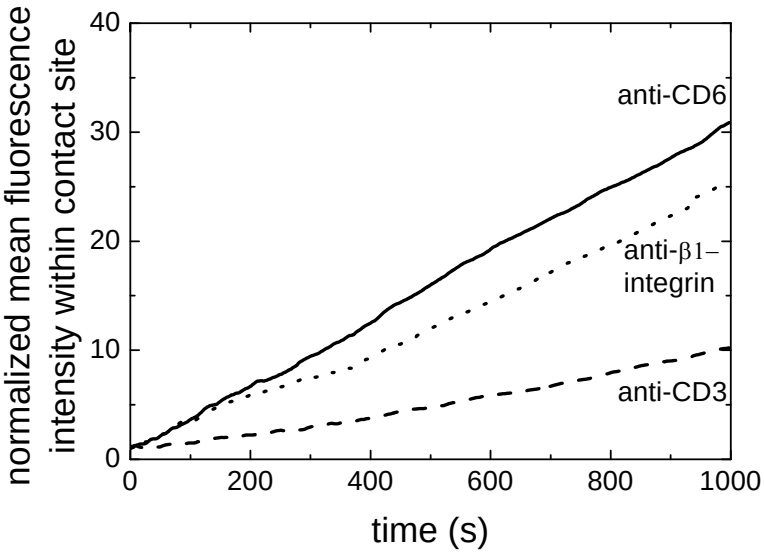

Fig. 4.9 CD6 recruitment and the actin cytoskeleton
Mean fluorescence intensity at the contact site over time as a measure for CD6-RFP recruitment in untreated Jurkat-CD6-RFP cells on various surfaces.

and CD6, so we hypothesized that recruitment would be unlikely in this situation. The curves are corrected for the background. Bleaching is corrected for as described in Box 4.3. After correction for photobleaching, curves were normalized to $I(t=0)$. As can be seen in Fig. 4.9, CD6-RFP is recruited towards the contact site at all three functionalized surfaces. Although on anti-CD3 recruitment is low (possibly because of the low CD3 expression on the cells, see Box 4-4), CD3 stimulation appears to induce CD6 recruitment. However, since also on anti-β1-integrin recruitment is observed, we can not conclude that the recruitment of CD6 towards the contact site is specific upon CD3 or CD6 stimulation. Assuming the recruitment is specific, the recruitment on anti-β1-integrin indicates that there is a relation between CD6 and β1-integrin. However, it is also possible that CD6 is aspecifically recruited towards the contact site upon cell-surface interaction, that is, CD6 comes along upon recruitment of the actin cytoskeleton or some other molecule (like CD5, considering the described relation between CD5 and CD6 (Gimferrer et al., 2003)).

4.4.4 Conclusions and Discussion – CD6 recruitment

CD6 is recruited towards the contact site on anti-CD6, anti-CD3 and anti-β1-integrin functionalized surfaces (Fig. 4.7A and 4.9). Experiments on cytoskeleton disruption to reveal the role of the actin cytoskeleton in this recruitment were inconclusive. Although disrupting the cytoskeleton revealed impaired recruitment (Fig. 4.7B), DMSO treatment also showed a similar effect on recruitment.

Therefore, more research is necessary to discriminate between membrane (affected by DMSO alone) and cytoskeleton effects. However, the measured surface coverage of the antibodies and the membrane expression of CD6, together with the mobility of CD6 in the contact site (Fig. 4.8), point towards an active recruitment process in stead of recruitment by diffusion.

Recruitment of CD6-RFP on anti-β1-integrin suggests that CD6 might be aspecifically recruited (that is, accompanying other molecules) towards the contact site. Therefore, a more detailed study should elaborate on the mechanisms of recruitment. For example, the possible role of the cytoskeleton can be investigated by impairing syntenin-1, the potential linker of CD6-cytoskeleton interaction. If CD6 would then still be recruited, other possibilities like different linker molecules, chaperoning molecules, or a role for membrane domains could be investigated. A possible chaperoning molecule could be CD5, since Gimferrer et al. (2003) showed by co-immunoprecipitation experiments that CD5 and CD6 are physically associated. It is furthermore recommended to measure CD5 expression on Jurkat-CD6-RFP cells. When there is low CD5 and high CD6 expression, for example, this would hint that CD5 is not the primarily recruited molecule, chaperoned by CD6, but that CD6 is recruited independently of CD5.

To study the influence of diffusion on the recruitment, we performed FRAP experiments. These experiments revealed mobile CD6-RFP at the contact site of anti-CD6 and anti-β1-integrin coated surfaces (Fig. 4.8). This can be caused by the excess of CD6-RFP at the contact site compared to anti-CD6 on the glass surface (comparing recruitment data (Fig. 4.7) with the ratio between surface coverage of the glass and the cell (Box 4-4 and 4-5)). Furthermore, the observed mobility on anti-β1-integrin functionalized surfaces suggests that CD6-RFP can move on the cell surface. We do not observe passive recruitment by diffusion of CD6-RFP towards the contact site on anti-CD6 coated surfaces for Jurkat-CD6-RFP cells pre-treated with DMSO or CytD. Although mobility of CD6-RFP on the non-contact side of the cell and for DMSO or CytD pre-treated cells has to be validated, increased mobility has been described upon CytD treatment for other molecules, like ALCAM and ALCAM-GPI (anchored in lipid membrane) (Nelissen et al., 2000), suggesting that diffusion does not play a role in CD6 recruitment. This validation could be done, for example, by more FRAP experiments.

4.5 General conclusions and outlook

In this chapter, we set out to measure the dynamics of CD6 in various situations and the possible role of the actin cytoskeleton in this dynamics. We showed that Jurkat T-cells stably expressing CD6-RFP spread on anti-CD6 functionalized surfaces and that disruption of the cytoskeleton impairs this spreading. Furthermore, we demonstrated that conventional spreading assays, performed in a supported configuration, positively influence the spreading abilities of cells, whereas our hanging configuration is more sensitive to cellular changes, for example by DMSO, and shows larger variations in spreading upon cellular treatment. Finally, we investigated the recruitment of CD6 to the contact site and showed that the recruitment is stronger upon CD6 stimulation, but also visible upon non-CD6 specific cell adhesion.

The results presented give rise to the model presented in Fig. 4.10. Before a Jurkat-CD6-RFP cell contacts the surface, CD6-RFP might be homogenously distributed at the cell surface and the actin cytoskeleton maintains the spherical shape of the cell (Fig. 4.10A). Upon interaction with a surface, the actin cytoskeleton is polymerized towards the site of interaction, possibly delivering or taking along CD6, which results in CD6 accumulation at the contact site (Fig. 4.10B); actin polymerization could be the active recruitment process mentioned in section 4.4. When the interaction continues, the actin polymerization induces cell spreading when the cell is able to bind to the surface; that is, when there are binding sites available at the glass surface and membrane molecules on the cell surface (Fig. 4.10C); based on the impaired spreading upon cytoskeleton disruption on anti-CD6, and the non-spreading on anti-CD3. After initial recruitment of CD6 and stretching of the cell on the surface, the process of actin polymerisation and CD6 recruitment still continues, but spreading is slower (Fig. 4.10D); based Fig. 4.7A and Fig. 4.1B.

The research described in this chapter highlights the need for more in-depth research on the relation between CD6 and the cytoskeleton, CD6 recruitment and the cytoskeleton, CD6 and the cell membrane. Although, we showed the influence on recruitment and spreading of cytoskeleton disruption, we also observed an influence by DMSO pre-treatment. This DMSO influence will at least be partly due to the hanging measurement configuration, which is sensitive to small cellular changes; however, other experiments are required to quantify the effect of DMSO

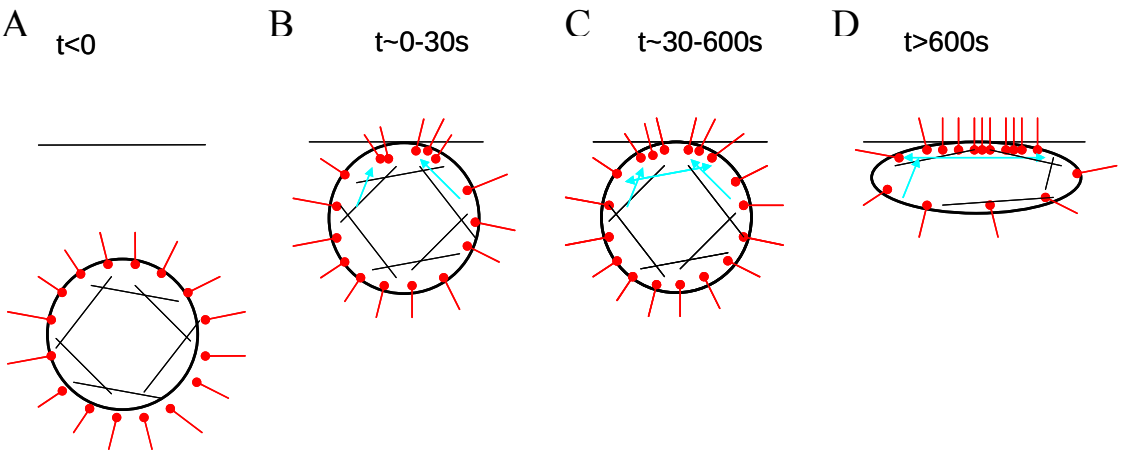

Fig. 4.10 Proposed model for CD6 dynamics upon cell-surface interaction
Legend: CD6-RFP molecules in red, black lines are actin polymers, blue arrows are actin polymerization in the direction of the arrow. (A) Before a Jurkat-CD6-RFP cell contacts the surface, CD6-RFP is homogenously distributed at the cell surface and the actin cytoskeleton maintains the spherical shape of the cell. (B) Upon interaction with a surface, the actin cytoskeleton is polymerized towards the site of interaction, delivering or taking along CD6, which results in CD6 accumulation at the contact site. (C) When the interaction continues, the actin polymerization induces cell spreading, when the cell is able to bind to the surface; that is, when there are binding sites available at the glass surface and membrane molecules on the cell surface. (D) After initial recruitment of CD6 and stretching of the cell on the surface, the process of actin polymerisation and CD6 recruitment still continues, but spreading is slower.

treatment on CD6 dynamics. Therefore, we recommend further investigations to discriminate between cytoskeleton and membrane effects. This can be done, for example, by using a cytoskeleton disruption reagent not dissolved in DMSO, colocalisation studies of CD6-RFP with actin-GFP or certain membrane lipids stained with GFP, blocking CD6-cytoskeleton (signalling) pathways or membrane disturbing reagents. These experiments might also reveal whether CD6 is specifically recruited towards the contact site or aspecifically by recruitment of other molecules. In the latter case, this might indicate that the role of ALCAM-CD6 interactions in contact stabilisation in the SMAC is a useful by-product of actin polymerisation towards the contact site, but not the main target.

As stated, we performed experiments on a unique set of cells that have high CD6 and low CD3 expression, enabling us to study CD6 induced processes with little or no CD3 intervention. Due to this low CD3 expression, we did not observe

cell spreading on anti-CD3 functionalized surfaces in our experiments, in contrast to that this effect has been described before by others (Parsey and Lewis, 1993) This could be caused by too few available binding sites at the cell surface, supporting the model as depicted in Fig. 4.10C. It would be interesting to investigate the influence of CD3 expression at the membrane surface on cell spreading and CD6 recruitment. This approach could test the model and investigate the relation between CD3 stimulation and CD6 dynamics in more depth.

Furthermore, it would be interesting to study the dynamics of CD6-RFP at smaller timescales. Since for CD2 a clustering in microdomains and movement of these microdomains has been described (Kaizuka et al., 2009), measuring faster and with shorter exposure times might reveal if CD6 conducts a similar behaviour. This can probably best be done using functionalized lipid bilayers, since on glass the antibody concentration might not be dense enough and the movement of the microclusters will most likely be hindered. If movement of microclusters is observed on functionalized glass, this would reveal new information on CD6 dynamics (for example, binding and unbinding kinetics and a possible stick-slip connection to the cytoskeleton (DeMond et al., 2008)) and immunological synapse formation.

Although, the presented model (Fig. 4.10) is based on cell-surface experiments, it could be valid for cell-cell interactions as well. The reported undisturbed cell spreading on anti-CD6 coated surfaces has a similar characteristic time as ALCAM expressing cells on CD6 functionalized substrates, as described in chapter 3. If ALCAM would be recruited towards the contact site upon interaction, similar to CD6, resulting in enough available binding sites, actin polymerization in both cells might result in an increasing contact site between cells, similar to cell-substrate interactions. However, cell-cell experiments might also reveal that cell spreading (increasing the contact site) is only observed in the specific situation of interaction with a functionalized substrate. A possible interesting experiment to test this might be monitoring whether cytoskeleton disruption of one cell impairs stable contact formation between cells.

References

AXELROD, D., KOPPEL, D. E., SCHLESSINGER, J., ELSON, E. & WEBB, W. W. 1976. Mobility Measurement by Analysis of Fluorescence Photobleaching Recovery Kinetics. *Biophysical Journal,* 16, 1055-1069.

BUNNELL, S. C., KAPOOR, V., TRIBLE, R. P., ZHANG, W. G. & SAMELSON, L. E. 2001. Dynamic actin polymerization drives T cell receptor-induced spreading: A role for the signal transduction adaptor LAT. *Immunity,* 14, 315-329.

CHAMARAUX, F., FACHE, S., BRUCKERT, F. & FOURCADE, B. 2005. Kinetics of Cell Spreading. *Physical Review Letters,* 94, 158102.

DEMOND, A. L., MOSSMAN, K. D., STARR, T., DUSTIN, M. L. & GROVES, J. T. 2008. T Cell Receptor Microcluster Transport through Molecular Mazes Reveals Mechanism of Translocation. *Biophys. J.,* 94, 3286-3292.

DIEZ-AHEDO, R., NORMANNO, D., ESTEBAN, O., BAKKER, G.-J., FIGDOR, C., G. , CAMBI, A. & GARCIA-PARAJO, M., F. 2009. Dynamic Re-organization of Individual Adhesion Nanoclusters in Living Cells by Ligand-Patterned Surfaces. *Small,* 5, 1258-1263.

ERBE, A. 2007. Calculation of the diffusion coefficient from FRAP (FPR) data. [Accessed 2010].

GIMFERRER, I., CALVO, M., MITTELBRUNN, M., FARNOS, M., SARRIAS, M. R., ENRICH, C., VIVES, J., SANCHEZ-MADRID, F. & LOZANO, F. 2004. Relevance of CD6-mediated interactions in T cell activation and proliferation. *Journal Of Immunology,* 173, 2262-2270.

GIMFERRER, I., FARNOS, M., CALVO, M., MITTELBRUNN, M., ENRICH, C., SANCHEZ-MADRID, F., VIVES, J. & LOZANO, F. 2003. The accessory molecules CD5 and CD6 associate on the membrane of lymphoid T cells. *Journal Of Biological Chemistry,* 278, 8564-8571.

GIMFERRER, I., IBANEZ, A., FARNOS, M., SARRIAS, M. R., FENUTRIA, R., ROSELLO, S., ZIMMERMANN, P., DAVID, G., VIVES, J., SERRA-PAGES, C. & LOZANO, F. 2005. The lymphocyte receptor CD6 interacts with syntenin-1, a scaffolding protein containing PDZ domains. *Journal of Immunology,* 175, 1406-1414.

GRAKOUI, A., BROMLEY, S. K., SUMEN, C., DAVIS, M. M., SHAW, A. S., ALLEN, P. M. & DUSTIN, M. L. 1999. The immunological synapse: A molecular machine controlling T cell activation. *Science,* 285, 221-227.

HATEGAN, A., SENGUPTA, K., KAHN, S., SACKMANN, E. & DISCHER, D. E. 2004. Topographical Pattern Dynamics in Passive Adhesion of Cell Membranes. *Biophys. J.,* 87, 3547-3560.

HYNES, R. O. 2002. Integrins: Bidirectional, Allosteric Signaling Machines. *Cell,* 110, 673-687.

JANEWAY JR., C. A., TRAVERS, P., WALPORT, M. & SHLOMCHIK, M. J. 2005. *Immunobiology*, Garland Science Publishing.

KAIZUKA, Y., DOUGLASS, A. D., VARDHANA, S., DUSTIN, M. L. & VALE, R. D. 2009. The coreceptor CD2 uses plasma membrane microdomains to transduce signals in T cells. *J Cell Biol*.

KELLER, P. M., PERSON, S. & SNIPES, W. 1977. Fluorescence Enhancement Assay of Cell-Fusion. *Journal of Cell Science,* 28, 167-177.

KOBARG, J., WHITNEY, G. S., PALMER, D., ARUFFO, A. & BOWEN, M. A. 1997. Analysis of the tyrosine phosphorylation and calcium fluxing of human CD6 isoforms with different cytoplasmatic domains. *European Journal of Immunology,* 27, 2971-2980.

LI, Y., XU, G. K., LI, B. & FENG, X. Q. 2010. A molecular mechanisms-based biophysical model for two-phase cell spreading. *Applied Physics Letters,* 96, -.

MEDDENS, M. 2009. *Microcontact printing to study the role of CD6 in T cell activation.* Master thesis, University of Twente.

MOSSMAN, K. D., CAMPI, G., GROVES, J. T. & DUSTIN, M. L. 2005. Altered TCR signaling from geometrically repatterned immunological synapses. *Science,* 310, 1191-1193.

NELISSEN, J. M. D. T., PETERS, I. M., DE GROOTH, B. G., VAN KOOYK, Y. & FIGDOR, C. G. 2000. Dynamic regulation of activated leukocyte cell adhesion molecule-mediated homotypic cell adhesion through the actin cytoskeleton. *Molecular Biology of the Cell,* 11, 2057-2068.

NOTMAN, R., NORO, M., O'MALLEY, B. & ANWAR, J. 2006. Molecular basis for dimethylsulfoxide (DMSO) action on lipid membranes. *Journal of the American Chemical Society,* 128, 13982-13983.

PARSEY, M. V. & LEWIS, G. K. 1993. Actin Polymerization and Pseudopod Reorganization Accompany Anti-Cd3-Induced Growth Arrest in Jurkat T-Cells. *Journal Of Immunology,* 151, 1881-1893.

VAN DER FLIER, A. & SONNENBERG, A. 2001. Function and interactions of integrins. *Cell and Tissue Research,* 305, 285-298.

WEE, S. F., SCHIEVEN, G. L., KIRIHARA, J. M., TSU, T. T., LEDBETTER, J. A. & ARUFFO, A. 1993. Tyrosine Phosphorylation of Cd6 by Stimulation of Cd3 - Augmentation by the Cd4 and Cd2 Coreceptors. *Journal of Experimental Medicine,* 177, 219-223.

YMETI, A. F. E. 2004. *Development of a multichannel integrated young interferometer immunosensor.* PhD Thesis, University of Twente.

ZHU, D.-M., DUSTIN, M. L., CAIRO, C. W. & GOLAN, D. E. 2007. Analysis of Two-Dimensional Dissociation Constant of Laterally Mobile Cell Adhesion Molecules. *Biophys. J.,* 92, 1022-1034.

ZIMMERMAN, A. W., JOOSTEN, B., TORENSMA, R., PARNES, J. R., VAN LEEUWEN, F. N. & FIGDOR, C. G. 2006. Long-term engagement of CD6 and ALCAM is essential for T-cell proliferation induced by dendritic cells. *Blood,* 107, 3212-20.

ZIMMERMANN, P. 2006. The prevalence and significance of PDZ domain-phosphoinositide interactions. *Biochimica Et Biophysica Acta-Molecular and Cell Biology of Lipids,* 1761, 947-956.

Appendix 4A. Calibration curve for FACS Aria II – FITC channel

To perform quantitative FACS experiments for the FITC-stained samples the flow cytometer was calibrated for that specific day and settings.

Materials and Methods

We calibrated the FACS Aria II (BD) with MESF-5 quantification beads (Bangs Laboratories, Fishers, IN). The standard protocol supplied by the manufacturer was used. Beads with 5 different fluorophore concentrations were dissolved in PBA (1% BSA in PBS). The bead population was selected in the forward-side-scatter plot. Then, in the FITC-channel the geometric mean of the 5 different intensity populations was determined.

Results

Fig. 4A shows the logarithmic values of the measured geo-mean as a function of the MESF value provided by the manufacturer. To these data, a linear function is fitted as described by BD in their protocol for quantification. This relation can be used to quantify the amount of FITC molecules at the specific day and settings for our cell samples.

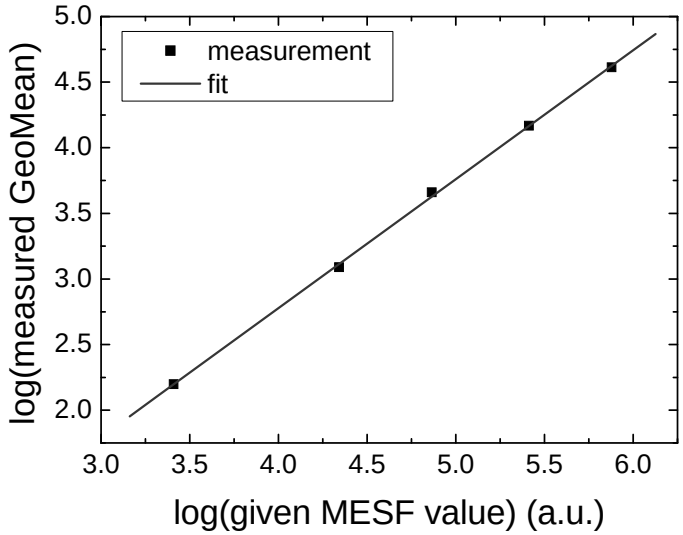

Fig. 4A. Calibration of FACS Aria II – FITC channel.
Fit by Y = A + B * X, where A = -1.15±0.06 and B = 0.98±0.01 (R=0.99975).

Appendix 4B. Cell diameter in various conditions

To measure the cell diameter, white light images were made of cells in the flow cell. Both cells that were trapped with the OT and cells that were on the bottom glass slide were imaged. Then, the cell diameter was measured as the distance between the cell borders, using ImageJ. Per condition 8-10 cells were measured. Fig. 4B shows the average cell diameter of Jurkat-CD6-RFP cells without or with (2 different concentrations of) DMSO. As can be seen, the average cell diameter is 16 μm, and DMSO seems to have no effect. A cell diameter of 16 μm corresponds to a cell surface size of ~800 μm^2. This cell diameter results in a maximum contact size of ~400 μm^2 when the cell is completely flat (like a pancake).

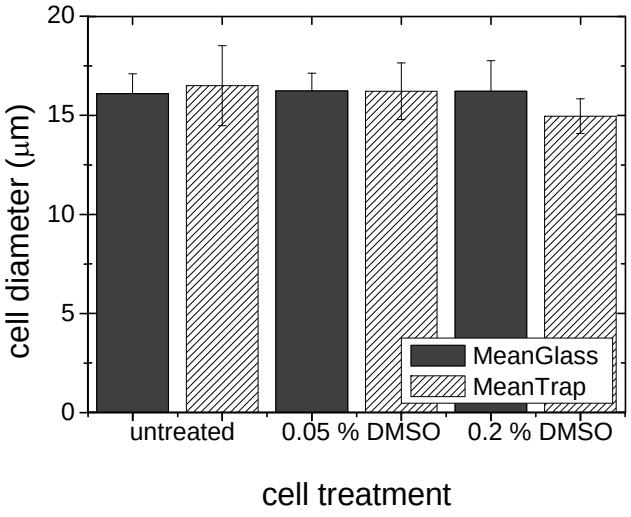

Fig. 4B. Diameter of Jurkat-CD6-RFP cells measured when held in the optical trap or lying on a glass surface, without or with DMSO pre-treatment.

Appendix 4C. Cell spreading and recruitment on BSA

We measured aspecific binding dynamics on BSA coated glass.

Materials and Methods

Flowcells were prepared as described in section 4.2.1, using only the BSA incubation step. Experiments were performed on the TIRF-OT setup, as described by the protocol in section 4.2.4. We used 3 different measurement frequencies: 0.1, 1 and 10 Hz.

Results

The solid line in Fig. 4C shows the contact size over time (left axis), an average over 7 cells. The dashed line shows the mean intensity over time (right axis) for the same cells. As can be seen, the cell does not spread and no recruitment of CD6-RFP is observed.

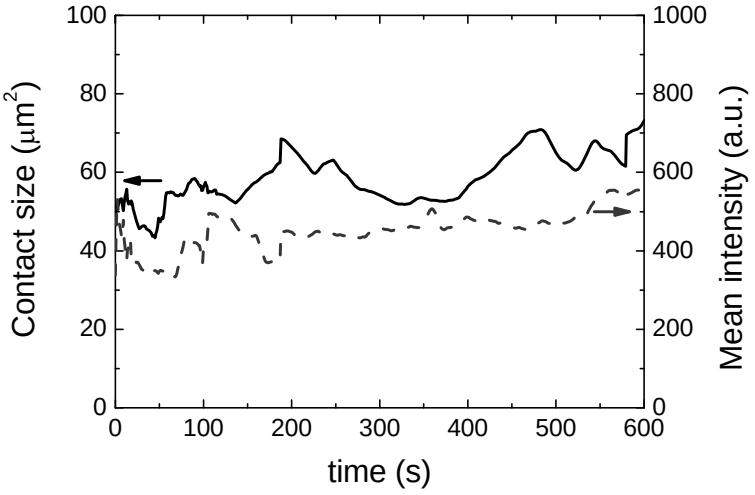

Fig. 4C. Jurkat-CD6-RFP cells brought in contact with a BSA functionalized surface, contact size and mean intensity within the contact site over time

Chapter 5 –

Cell-cell experiments

5.1 Introduction

Cell-cell interactions play an essential role in the working of an organism, and thus understanding these interactions is of paramount importance. An important method to study cells and processes within cells is microscopy. Microscopic imaging approaches have illuminated, for example, protein interactions, signalling cascades and plasma membrane domains involved in cell-cell interaction (Lidke and Wilson, 2009). The field of microscopy has evolved to give unprecedented insights into these cell-cell interactions. More specifically, fluorescence microscopy methods facilitate dynamic spatial and temporal imaging of molecular interactions, especially in *in-vitro* experiments. This is crucial, since not only the presence, but also the spatial organisation and dynamics of membrane molecules at the interaction sites of immune cells, appears to be critically important for communication between the cells (see section 1.5.2, and (Dustin, 2009, Kaizuka et al., 2007)). Therefore, precise imaging requires the interaction site to be visualized with high spatial and temporal resolution. Current methods face two main obstacles that reduce both spatial and temporal resolution, namely, a lack of resolution at the interaction site that is not (fully) in the focal plane, and the uncertainty in determining the temporal starting point of the interaction.

In time-lapse microscopy, quantification of dynamic processes is hampered because the starting point of interaction is undetermined. A common method of inducing cell-cell interactions is to pipet cells into the same volume. The interaction between cells is either expected to start at the moment of mixing, or at a later time point, when the researcher observes the cells to come in close vicinity (see for example, (Zimmerman et al., 2006)). However, in both cases the determination of

the onset of interaction is not precise, and the ability to monitor processes that happen during in the first few seconds to minutes is restricted, hampering the study of the first processes upon cell-cell interaction.

The spatial quantification of membrane molecules during cell-cell interaction is limited as a result of the measurement configuration. Upright and inverted microscopes both have a horizontal focal plane, whereas the interaction site between cells explores a much larger solid angle, and is often tilted towards the vertical plane. In order to image the whole interaction site, a stack of images, scanning through the z-direction, has to be made. This problem is faced in various manners, see for example Fig. 5.1. In Fig. 5.1A the interaction site (red) is situated as it naturally occurs for two cells pipetted into the same volume. The dynamics are monitored by focussing on the centre of the interaction site and measuring the appropriate signal over time at that spot (Zimmerman et al., 2006). This method is, however, unable to measure the spatial distribution of the membrane molecules at the contact site with high precision, for example the existence of a peripheral and central supramolecular activation cluster (SMAC; see section 1.3.2 and Fig. 1.5). Fig. 5.1B depicts the situation in which a monolayer of cells is grown on a substrate, and upon which the second cell is added. However, generally this method does not necessarily result in a single cell-cell interaction, since the second cell may land on and interact with multiple cells; this might influence the interaction. Furthermore, this situation still might face a tilt in the interaction plane (Alfsen et al., 2005). Another option is the use of a functionalized lipid bilayer instead of a second cell (Mossman et al., 2005, Groves and Dustin, 2003). The advantage of this system is that spatial resolution is indeed improved and the interaction site is fully

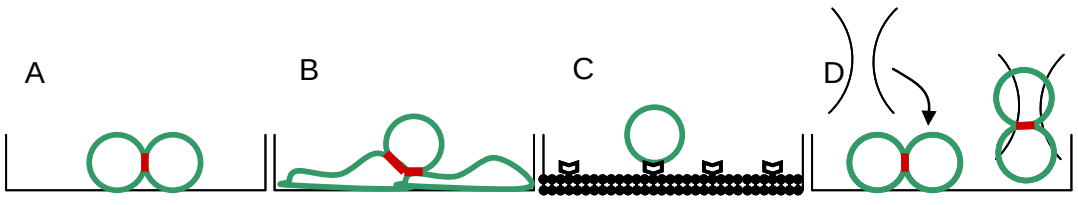

Fig. 5.1 Method to align contact site parallel to focal plane of the objective
(A) problem statement: vertical interaction site (red) while horizontal focal plane (objective below well, not in picture), (B) cell-cell interaction where one cell is grown as a monolayer on the coverglass surface, still not a fully horizontal contact site, (C) cell interacting with a functionalized bilayer, (D) cell-cell interaction, grabbed with optical tweezers to align the interaction site.

situated in the focal plane. However, although this bilayer enables the study of the molecules of interest, it is a simplified, artificial system, lacking other molecules having a role in the original cell-cell interaction and using GPI-anchored proteins instead of the original transmembrane proteins (Groves and Dustin, 2003). The fourth situation depicted (Fig. 5.1D), is described by Oddos et al. (2008). They use optical tweezers to trap an interacting cell pair, which will align in the trap and give a horizontal interaction plane. This last option solves the problem of spatial resolution; however, it does not solve the temporal issue.

Our aim is to develop a solution that solves both the temporal and spatial issues, in order to measure membrane protein dynamics of interacting cells. The onset of interaction can be controlled, for example, by holding a cell with optical tweezers or a micropipette and bringing it in contact with another cell. However, this implies sequential measuring of cell-cell interactions with low throughput, since only one cell at a time can be positioned as desired. Therefore, the theory section of this chapter also describes calculations on the probability of cell-cell interactions when cells are pipetted into the same volume, to test if this approach will give a higher throughput. To visualize the contact site, various microscopy methods are available: TIRF microscopy, epi-microscopy, highly inclined laminated optical sheet (HILO) microscopy, and confocal microscopy. In the theory section, the different illumination schemes are described with respect to the signal-to-background ratio of the fluorescence images of the contact site of two cells. The results section describes measurements on cell-cell interactions, with CD6-ALCAM and ALCAM-ALCAM interactions (chapter 1.3.3) as a model system, using both optical tweezers and micropipettes for manipulation.

5.2 Theory

5.2.1 Control of the onset and position of the interaction site

Random seeding

Cell-cell interactions can be induced by pipetting cells into the same volume. This opens up the possibility of visualizing many cell-cell interactions in the same

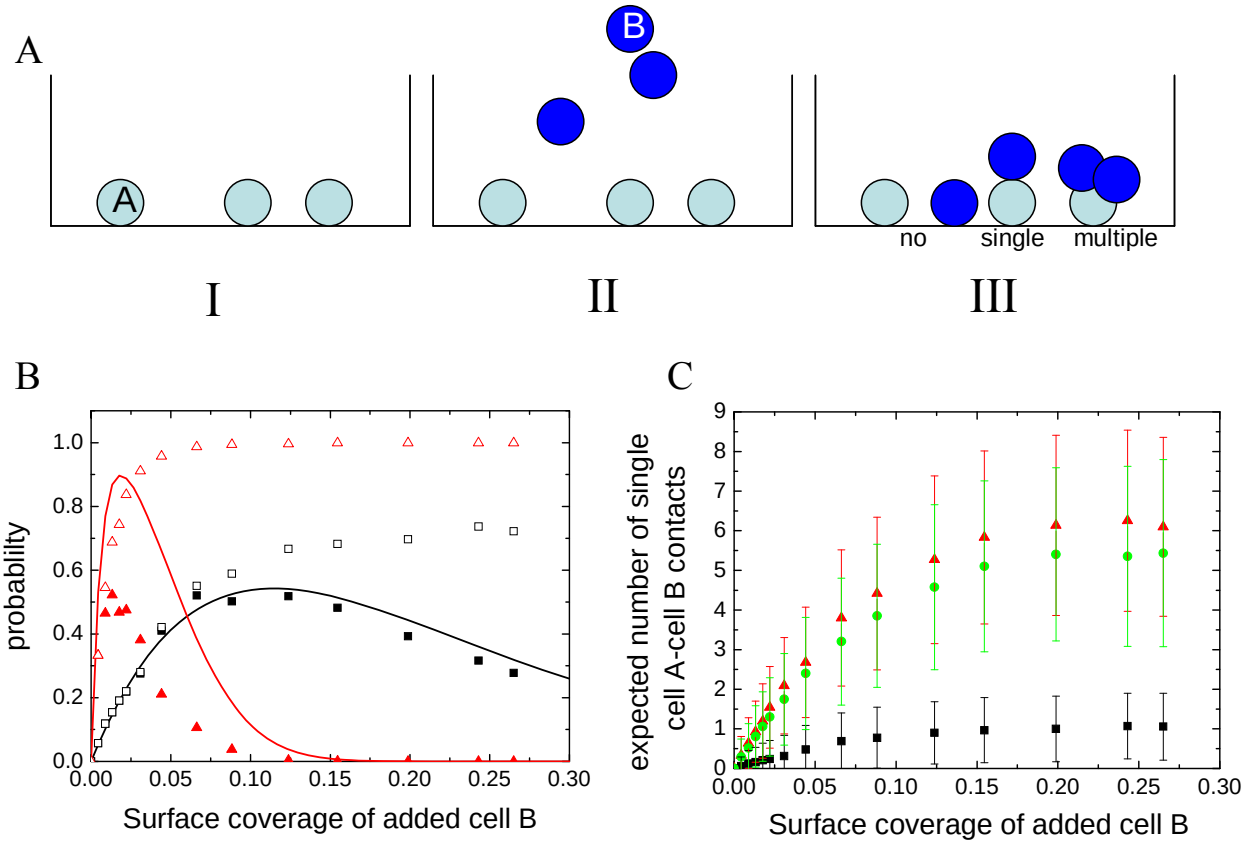

Fig. 5.2 Probability calculation and simulation (A) schematic representation of cell-cell interaction based on probability; A-I shows cells A present at the bottom of the well, A-II shows that cells B are added to the well, A-III shows the definition of no contact, single contact or multiple cell-cell contacts. (B) Probability of only single cell-cell interactions (solid lines and squares) or at least one single cell-cell interactions (open squares) as a function of the surface coverage by the added cells, for two different surface coatings by cells A in the well: 0.013 (black) and 0.13 (red). The lines represent the calculations based on Eq. 5.2; the squares are calculated from 1000 simulations of the specific situation. (C) The expected number of single cell A-cell B interactions in the field of view, based on simulations, as a functions of the surface coverage by the added cells, for three different surface coatings by cells A in the well (0.013 - black, 0.13 - red and 0.44 - green). Represented are the mean and standard deviation of the expected value.

field of view, giving a higher throughput and a corresponding increase in statistically relevant numbers of interactions than sequential methods based on OT or micropipettes. This section describes the calculation and simulation of the probability of cell-cell interactions induced in this manner, in order to investigate whether this method indeed gives a higher throughput.

Fig. 5.2A schematically represents the situation that is discussed in this section. Cells A are positioned at the bottom of a well (I), cells B are added to the

well (II), and sediment under gravity to the bottom of the well. The final situation gives single, multiple or no cell-cell contacts (III). If one adds a single cell B to a well with an area A_w that contains N_A cells of type A at the bottom of the well, the chance of this cell B to interact with a cell A, can be described by:

$$P_{N_A 1} = N_A \frac{4A_c}{A_w} \qquad \text{Eq. 5.1}$$

where $A_c = \pi R_c^2$ is the area covered by a cell A, with radius R_c. Cell A and cell B are in contact when the total distance between the cells is $<2R_c$. This can be accounted for in the calculations by doubling the radius of cell A and taking cell B as a point with no radius (assuming cell A and B are spheres with the same radius R_c), which results in the factor 4 in Eq. 5.1.

When N_B cells B are added, the chance of having only single cell A-cell B contacts is:

$$P_{N_A N_B} = \sum_{i=1}^{N_B (N_B \le N_A)} \left(\frac{4A_c}{A_w} \right)^i \left(1 - N_A \frac{4A_c}{A_w} \right)^{N_B - i} \frac{1}{i!} \frac{N_B!}{(N_B - i)!} \frac{N_A!}{(N_A - i)!}$$

Eq. 5.2

The solid lines in Fig. 5.2B give the probability of only single cell-cell interactions, calculated from Eq. 5.2, as a function of the surface coverage (Sc) of cells B ($Sc = N_B \pi R_c^2 / A_w$). Used parameters in the calculations: A_w=200*200 μm[6], *Sc* of cells = 0.013 (black) or 0.13 (red)[7], R_c = 7.5 μm (see Appendix 5A).

In addition to the calculations, a computer simulation was performed that simulated the specific situation 1000 times and calculated the probability based on these simulations. In the simulations cells A are randomly distributed in a well size A_w, giving N_A points with coordinates $(x_A,y_A)_i$, and similarly for cells B: N_B points $(x_B,y_B)_j$. Then, the distance between a cell A and a cell B is determined

[6] For a confocal microscope with a high NA objective (1.4, 63x oil immersion), a chosen pixel size slightly smaller than the diffraction limit (Chapter 1.2.1.2) for the highest spatial resolution, and a system that can scan maximum 1024*1024 pixels, the field of view will approximately be 200*200 μm.

[7] A surface coverage of 0.13 corresponds in this setting to N_A=30; this was chosen based on the requirement that single cell-cell interactions can only be arranged when the distance between two cells A >$2R_c$. This gives a maximum number N_A of ~ 40 ((well length/($4R_c$))^2)

($d = \sqrt{(x_A - x_B)^2 + (y_A - y_B)^2}$), for every cell A and cell B (i=1 to N_A and j=0 to N_B). When $d<2R_c$ and only one cell A is interacting with only one cell B, this is counted as a single cell-cell contact. When $d<2R_c$ and one cell A interacts with multiple cells B, or one cell B interacts with multiple cells A, the situation is counted as a multiple cell-cell contact. The closed squares (Fig. 5.2B) give the probability of having only single cell-cell interactions, which should follow the solid line, whereas the open squares give the probability of having at least one single cell-cell interaction. The difference between the calculations and simulations for N_A=30 (red colour) originates from the distance between cells of type A. Eq. 5.2 is based on the assumption that the initial distribution of cells of type A is such that the distance between the cells A is $>2R_c$. This is not a prerequisite in the simulations, which are corrected for the situation that one cell B interacts with two cells A. This results in a lower probability in the simulation than what is achievable theoretically. From Fig. 5.2B, it can be concluded that there is an optimal number of cells B to be added, depending on the concentration of cell A, if only single cell-cell contacts are required (solid lines and solid squares). In practice, however, the situation of having at least one single cell-cell interaction is more interesting (open squares), and this is less sensitive to the number of added cells B, especially for higher concentrations of cell A.

Since we set out, in this section, to determine the versatility of inducing cell-cell interactions by pipetting cells together in order to increase throughput, we determined the expected number of single cell A-cell B contacts in the field of view by simulations. The number of single cell-cell contacts was calculated simulating the specific situation 1000 times, while determining every time the number of single cell-cell contacts (so, how often $d<2R_c$ is true and only one cell A interacts with only one cell B). Then, the expected number of single cell-cell contacts was determined as the mean number of single cell-cell contacts over these 1000 times simulations. Fig. 5.2C shows the expected number of single cell-cell contacts in the well, with the standard deviation, as a function of the surface coverage of cells B, for three concentrations of cells A (Sc [of cells of type A] = 0.013, 0.13, or 0.44). As to be expected, the maximum number of single cell-cell interactions depends of both N_A and N_B, after which the expected number of single cell-cell interactions decreases. The mean expected value of single cell-cell interactions in the field of

view is maximally ~6, since both higher and lower surface coverage of cells A than 0.13 result in a lower maximum number of single cell contacts. This implies that the throughput is six times higher for the method of pipetting cells together, than when only one cell-cell interaction is monitored at a specific moment (like with optical tweezers- and micropipette-based methods).

From the calculations and simulations presented in this section, it can be concluded that the number of cells A and B can be optimized for having multiple single cell-cell contacts, when pipetting the cells into the same volume. However, the throughput will only increase by a factor of six. Furthermore, this method does not give control over the position of the interaction on the cell with respect to the nucleus and does not account for the alignment of the interaction site to the focal plane. In practice, therefore, the throughput of cell-cell interactions of interest with fully visualized contact sites will be even lower. Since the higher throughput was the main advantage of this method of inducing cell-cell interactions, the data presented in this section indicate that a more controlled manner of inducing cell-cell interactions than pipetting cells into the same volume is more advantageous.

Micropipette- and optical tweezers-based method for inducing cell-cell interactions

A more controlled manner of bringing two cells in contact with each other is the use of tools to grab one cell and move it towards another cells. Although this implies sequential measuring of single cell-cell interactions, the decrease in throughput is in fact not dramatic, as explained in the previous section. Two methods of inducing cell-cell interactions in a controlled manner are depicted in Fig. 5.3.

Optical tweezers can trap a cell B and bring it in contact with cell A at a surface (Fig. 5.3A). The advantage of OT is that they do not physically touch the cell and, with the right power settings of the laser, do not interfere with processes in the cell or with cell membrane dynamics. Furthermore, OT can be used in a closed flowcell system, as long as the material of the flowcell is optically transparent. Therefore, a cell can be flown in, trapped and positioned at the spot of interest, that is, at or upon the other cell in the focal plane of the microscope. The limitations of this method are mainly in the temporal and spatial positioning of the cell. As

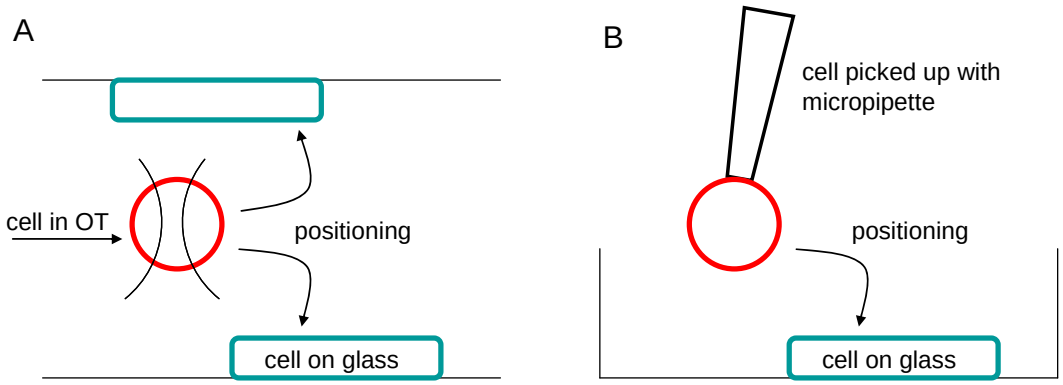

Fig. 5.3 Controlling position of cell-cell interaction (A) a cell (red) can be trapped with OT and positioned on a cell (green) at the top or bottom glass (B) a cell (red) can be picked up with a micropipette and positioned on a cell on the bottom glass

estimated in section 3.2.1, the accuracy of positioning a cell with the OT in the lateral direction is in the order of the cell radius, most likely ~ 1 μm, and the speed in the axial direction is ~ 0.5 μm/s.

A micropipette is also able to hold and position a cell (see Fig. 5.3B). This method can not be used in a closed system, such as the prism-based TIRF microscope described in this study. However, a micropipette can be relatively easily implemented on many microscopes of interest, like a confocal microscope. A disadvantage of this method can be that the micropipette physically touches the cell, inducing mechanical stress responses of the cell and limiting the spatial mobility of the membrane molecules. The main limitations for spatial and temporal positioning depend on the micromanipulator used, which in this study is ~ 1 μm lateral accuracy (data not shown).

5.2.2 Visualisation of the contact site

Calculations on widefield-HILO-TIRF illumination

Fluorescence excitation is possible with various illumination configurations. Fig. 5.4A schematically represents three possibilities where widefield detection is combined with either widefield-, HILO- or TIRF-illumination. Widefield illumination comprises all illumination techniques that expose the entire object,

which corresponds to low angles θ_i in Fig. 5.4A. Highly inclined and laminated optical sheet (HILO) microscopy uses a tilted beam to illuminate only a limited section in z (Tokunaga et al., 2008). This HILO illumination corresponds with angles θ_i in Fig. 5.4A close to the critical angle θ_c, with $\theta_c = \sin^{-1}\left(\frac{n_2}{n_1}\right)$. TIRF illumination by the evanescent field in the sample is obtained by total internal reflection of the excitation beam, that is, when $\theta_i > \theta_c$. Both TIRF and HILO give a higher signal-to-background ratio than widefield-illumination microscopy methods. In this section, we calculate the illumination intensities and signal-to-background ratios specific for cell-cell interactions, draw conclusions on the theoretical feasibility of widefield-, TIRF-, and HILO illumination, and give the requirements for optimal HILO illumination for measuring cell-cell interactions.

We assume illumination with an s-polarized Gaussian beam (width w), with intensity I_0, at an angle θ_i directed to $(x,y,z)=(0,0,0)$, with the centre of the contact site between the two cells at $(x,y,z) = (-z_1 \tan\theta_t, 0, z_1)$. The general expression for the intensity profile of a 2D Gaussian beam travelling in the z-direction is given by:

$$I(x,y) = \frac{P}{2\pi w_x w_y} e^{-\frac{x^2}{2w_x^2} - \frac{y^2}{2w_y^2}} \qquad \text{Eq. 5.3}$$

The term before the exponential term normalizes to a constant power (P) of the beam, since this power is independent of w. For a circular beam $w_x = w_y = w$. However, illumination under an angle, as depicted in Fig. 5.4A, gives an elliptical beam with $w_x = w\frac{\cos\theta_t}{\cos\theta_i}$ and $w_y = w$, where $\theta_t = \sin^{-1}\left(\frac{n_1}{n_2}\sin\theta_i\right)$. Furthermore, the transmission of the light is dependent on the angle of incidence θ_i. Therefore, for $\theta_i < \theta_c$ (widefield and HILO illumination), Eq. 5.3 should be corrected by $P_t = P_i T$, where P_t is the transmitted power, P_i is the incident power, and T is the transmittance (Hecht, 1987):

$$T = \frac{n_2}{n_1}\frac{\cos\theta_t}{\cos\theta_i} t_s^2 = \frac{n_2}{n_1}\frac{\cos\theta_t}{\cos\theta_i}\left(\frac{2n_1\cos\theta_i}{n_1\cos\theta_i + n_2\cos\theta_t}\right)^2 \qquad \text{Eq. 5.4}$$

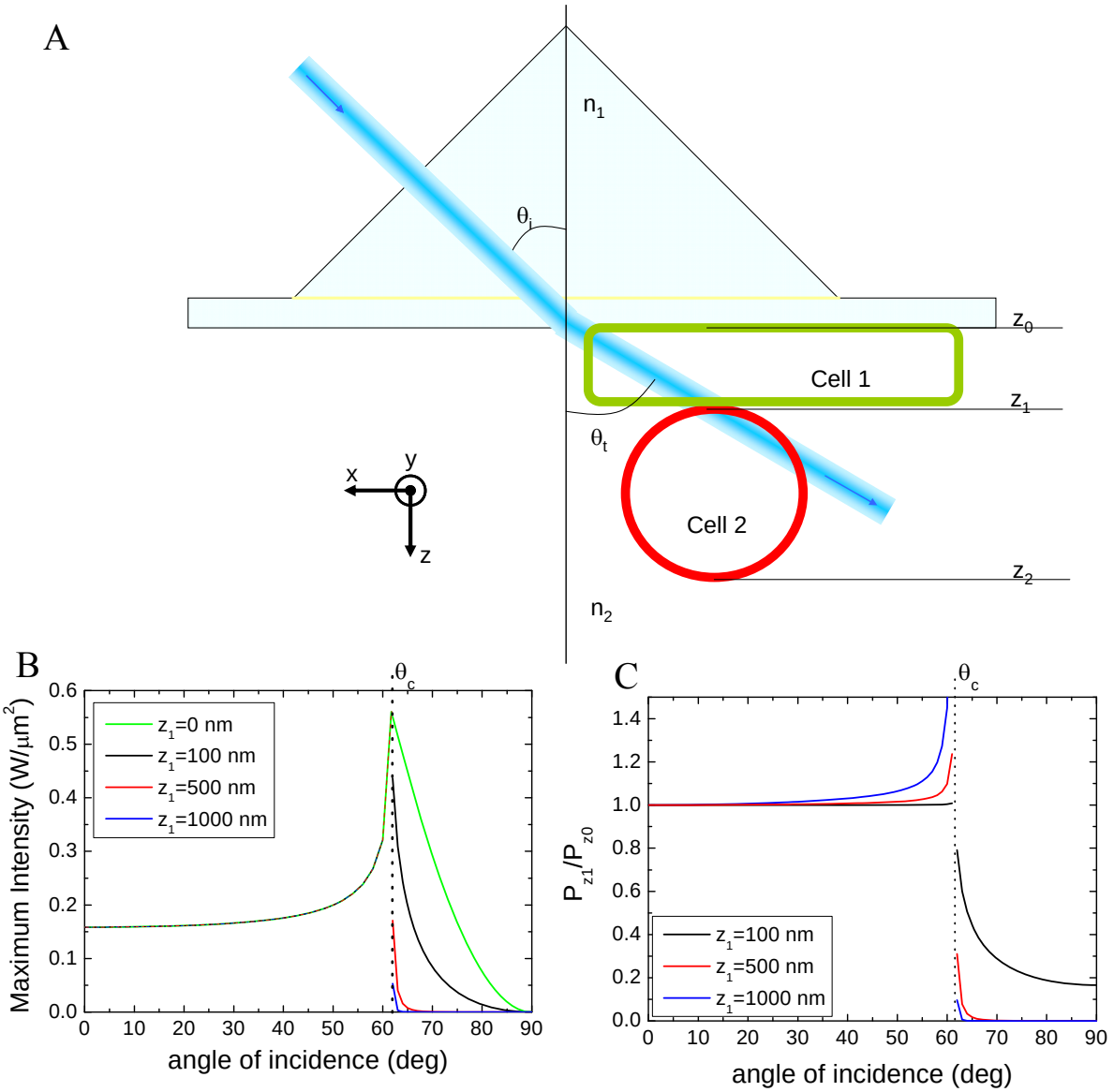

Fig. 5.4 Widefield-HILO-TIRF illumination (A) Schematic overview widefield (small θ_i) and HILO (larger θ_i) microscopy with the definition of coordinate system and depths as used in the calculations. θ_i is the angle of incidence and θ_t is the angle of transmission, n_1 is the refractive index of glass (1.51) and n_2 is the refractive index of the cells and their surrounding medium (~1.33). At z_0 z=0, at z_1 z=thickness cell 1, at z_2 z=thickness cell1+cell2. (B) Maximum intensity at various depths as a function of the angle of incidence; for $\theta_i << \theta_c$ widefield illumination, for $\theta_i < \theta_c$ HILO illumination (all lines on top of each other), and for $\theta_i > \theta_c$ (~60.5 deg) illumination by the evanescent field caused by total internal reflection of the incident Gaussian beam (w=1 μm). (C) Ratio between integrated intensities at depth z_1 and z_0: P_{z1}/P_{z0}, for various values of z_1, as a function of θ_i (w=3 μm, R=3 μm). (D) Ratio P_{z1}/P_{z0} as a function of the beam width w (z_1= 500 nm, R=3 μm, θ_i=60 deg)

Since the given expression for a Gaussian beam is only true for θ_i=0 deg, the formula has to be adapted for a rotation of the coordinate system around the *y*-axis with θ_t :

$$I(x,y) \propto e^{-\frac{x^2}{2w^2}-\frac{y^2}{2w^2}} \xrightarrow{rotation\_\theta_i} I(\theta_i,x,y,z) \propto e^{-\frac{(x\cdot\cos\theta_t+z\cdot\sin\theta_t)^2}{2w^2\cos^2\theta_t/\cos^2\theta_i}-\frac{y^2}{2w^2}}$$

Eq. 5.5

Combining Eq. 5.3-5.5 gives the intensity distribution in medium 2 for a Gaussian beam in the situation depicted in Fig. 5.4A, when $\theta_i<\theta_c$

$$I(\theta_i,w,x,y,z) = \frac{P_i}{2\pi w^2}\frac{n_2}{n_1}\left(\frac{2n_1\cos\theta_i}{n_1\cos\theta_i+n_2\cos\theta_t}\right)^2 e^{-\frac{(x\cdot\cos\theta_t+z\cdot\sin\theta_t)^2}{2w^2\cos^2\theta_t/\cos^2\theta_i}-\frac{y^2}{2w^2}}$$

Eq. 5.6

Where the previous equations were true for widefield and HILO illumination, in case of TIRF illumination, where $\theta_i>\theta_c$, the intensity distribution is that of an evanescent field with penetration depth d_p (Axelrod, 2007):

$$I(z) = I_i\frac{n_2}{n_1}I_{TIRF}e^{-\frac{z}{d_p}} \qquad \text{Eq. 5.7}$$

with $I_i\frac{n_2}{n_1}$ the incoming intensity of the tilted Gaussian beam corrected for the difference in refractive index of medium 1 and 2, and I_{TIRF} the evanescent intensity at the interface, which for *s*-polarized light is: $I_{TIRF} = \frac{4\cos^2\theta_i}{1-\left(\frac{n_2}{n_1}\right)^2}$ (Axelrod, 2007).

Combining Eq. 5.3, Eq. 5.5 and Eq. 5.7 gives:

$$I\ (\theta_i,w,x,y) = \frac{P_i}{2\pi w^2}\frac{n_2}{n_1}\frac{4\cos^2\theta_i}{1-\left(\frac{n_2}{n_1}\right)^2}e^{-\frac{(x\cdot\cos\theta_t+z\cdot\sin\theta_t)^2}{2w^2\cos^2\theta_t/\cos^2\theta_i}-\frac{y^2}{2w^2}}e^{\frac{-z}{d_p}} \qquad \text{Eq. 5.8}$$

Fig. 5.4B plots the maximum intensity (that is, using the peak value of the Gaussian beam) in the sample as a function of θ_i for P_i=1 W, w=1 μm^2, λ=500 nm, n_1=1.51, n_2=1.33, for four values of z. When $\theta_i<\theta_c$, light is transmitted and the

maximum intensity of the beam is independent of the depth z, however, when $\theta_i > \theta_c$ light is totally reflected at the surface and the evanescent field is dependent on z.

In the experimental situation, assuming only fluorescence from the cell membranes, the ratio between the intensities at the different surfaces z_0 (z=0 nm), z_1 (the thickness of cell 1) and z_2 (the thickness of cell 2) is important, because these ratios are related to how well fluorescence at the contact site can be discriminated from the fluorescence at other sites. However, before calculating the ratios, first the depth of focus (DOF) of the objective should be considered. The DOF defines what range of z is in focus on the camera; the intensity projection on the camera from out-of-focus light is dependent on the distance to the focus. The DOF is given by (Pawley, 1990):

$$DOF = 2\frac{\lambda n}{(NA)^2} \qquad \text{Eq. 5.9}$$

where λ is the wavelength (~500nm), n is the refractive index of the medium (1.33), and NA is the numerical aperture of the objective (1.2). This gives $DOF \approx 0.9$ μm, therefore everything in the range z_{focus}+0.9 μm to z_{focus}-0.9 μm of the focus of the objective is imaged with constant efficiency on the camera (z_{focus} is the depth where the object is focused on). Therefore, with the focus at z_1, which will be relatively close to the microscope glass (for thin adherent cells, like for example dendritic cells), z_0 will be in focus, but $z_2 \approx 15$ μm will not. Experimentally, it was measured that fluorescent light coming from more than 4 μm of the focal plane, is not contributing to the intensity signal (data not shown). Therefore, the ratio P_{z2} / P_{z1} is not calculated.

The ratio P_{z1} / P_{z0} is a measure for the signal (that is, fluorescence at the contact site) to background (that is, fluorescence from the membrane adhered to the microscope glass) ratio. A ratio of one means that fluorophores at z_0 and z_1 contribute equally to the detected fluorescence intensity. This ratio should preferably be as large as possible to discriminate between contact site (at z_1) and non-contact site (at z_0) membrane molecules. Fig. 5.4C shows the ratio of integrated intensity values P_{z1} / P_{z0} over θ_i, for a square contact site centred at $(x,y,z) = (-z_1 \tan\theta_t, 0, z_1)$, radius R=3 μm, with w=3 μm, and three different values of z, that is:

$$\frac{P_{z1}}{P_{z0}} = \frac{\int_{y=-R}^{R} \int_{x=-R-z\tan\theta_t}^{R-z\tan\theta_t} I(\theta_i, w, x, y, z_1)\,dydx}{\int_{y=-R}^{R} \int_{x=-R-z\tan\theta_t}^{R-z\tan\theta_t} I(\theta_i, w, x, y, z_0)\,dydx} \qquad \text{Eq. 5.10}$$

Clearly, for small θ_i and for $\theta_i > \theta_c$ the depicted ratio indicates that widefield and TIRF illumination are not beneficial to monitor the fluorescence at the contact site with high selectivity; the fluorescence at z_0 will always be more pronounced visible than the fluorescence for z_1. TIRF excitation for cell-cell experiments will, therefore, not be advantageous in this respect, when substantial fluorescence form the membrane at z_0 is expected. TIRF illumination will only limit the contribution of out-of-focus light from the second cell. However, Fig. 5.4C demonstrates that fluorescence excitation with HILO illumination (θ_i~50-60 deg) enables discrimination between the contact site and the microscope slide side of the cell with a ratio >1, especially for higher values of z_1. Furthermore, Fig. 5.4D shows the ratio P_{z1} / P_{z0} as a function of the beam width w, and demonstrates that HILO illumination is especially advantageous for smaller beam width. HILO illumination will, therefore, be a versatile approach for cell-cell measurements, especially when the settings are optimized. This optimisation includes the following points:

- An angle of incidence θ_i close to the critical angle θ_c
- A small beam width (defined by the full width half maximum (FWHM) of the beam is $FWHM = 2\sqrt{2\ln 2}w$), that still should be able to illuminate the whole contact site. That is, in x the minimum beam width should be $w \geq R/\sqrt{2\ln 2}\cos\theta_t$ and in y $w \geq R/\sqrt{2\ln 2}$, the latter being a more stringent criterion.
- The beam should be aligned with respect to the contact site, such that the centre of the contact site is situated at the centre of the beam, that is (x,y,z) =($-z_1\tan\theta_t$, 0, z_1).

Confocal microscopy

A limitation in conventional widefield microscopy methods is the resolution and detection from out-of-focus fluorescence. Confocal microscopy provides a mean to address these issues, especially the out-of-focus blur. Fig. 5.5 shows schematically the principle of confocal microscopy. A pinhole is positioned in the conjugate plane of the objective lens. Therefore, only light that is in the focus of the objective lens will be in focus in the plane where the pinhole is positioned, and can pass the hole to be collected on a photosensitive element (green rays). Out-of-focus light will be blocked by this pinhole (red rays). Illumination is performed by scanning a laser beam over the sample with 2 scanning mirrors (blue rays), hence the name of the instrument is confocal laser scanning microscope (CLSM). The laser beam is expanded to fill the back aperture of the objective in order to create an illumination spot at the sample as small as possible (laterally). Both lateral and axial resolutions of the confocal microscope are higher than those for a conventional microscope (Olympus, 2010), as shown in Table 5-1.

A major drawback of the classical confocal microscope is the low scanning speed of the mirrors, which limits the measurement frequency. This has been addressed by the development of a spinning disk confocal microscope, in which the mirrors are replaced with a spinning disk with holes in it (Nakano, 2002). Rotation of the disk enables fast scanning over the sample, and the collected light can be projected on a CCD camera.

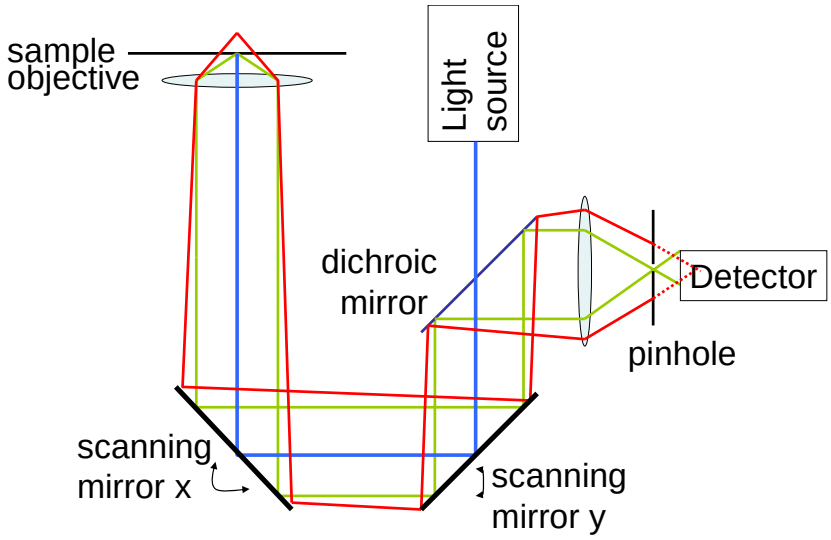

Fig. 5.5 Confocal microscopy principle Out of focus light (red lines) is blocked by the pinhole, while light from the focus of the objective (green lines) is reaching the detector

Table 5-1. Resolution of a microscope

	Conventional microscope	*Confocal microscope*
Lateral	Diffraction limit $d = 0.61\lambda / NA$	Resolution $r = 0.4\lambda / NA$
Axial	Depth of focus $DOF = 2\frac{\lambda n}{(NA)^2}$	Resolution $r = 1.4\frac{\lambda n}{(NA)^2}$

5.3 Materials and Methods

5.3.1 Cell culture and preparation

RAW 264.7 cells[8] were cultured in RPMI-1640 medium containing phenol-red (Invitrogen) with 10% FBS (Invitrogen) and 1% AA (Invitrogen). Cells were transfected with ALCAM-GFP using FuGENE HD (Roche) and a stable cell line was obtained with G418 as a selection medium. Cells were seeded on a microscope glass 24 h. prior to the experiment in phenol-red free RPMI-1640 medium in a specified area surrounded by a hydrophobic barrier (made using a DAKO Pen, DAKO). The density was ~$7x10^3$ cells/cm^2, and ~200 ml medium covered the cells in the incubator. Staining of the membrane of RAW cells was done by incubating with ~0.025 mg/ml DiI (Invitrogen) in Iscove's modified Dulbecco's medium (IMDM, Invitrogen) for 30 min. at 37 ºC, and afterwards washing with PBS.

Jurkat-CD6-RFP cells (Meddens, 2009) were cultured in the same medium as RAW cells, with G418 as a selection medium. Cells were seeded 24h before the experiment at a concentration of $4x10^5$ cells/ml in phenol-red free RPMI medium. Prior to the experiment, 5% of the cells with highest fluorescence intensity were sorted with a FACS ARIA II flow cytometer (BD) and suspended in serum-free RPMI medium at a concentration of $1x10^6$ cells/ml with 25mM Hepes (Invitrogen).

[8] Endogenous ALCAM expression on RAW 264.7 cells is low and can be ignored; experiment by Inge Beeren (NCMLS).

K562 cells were stably transfected with ALCAM-GFP (Nelissen et al., 2000), and cultured in IMDM (Invitrogen) with 10% FBS, 1% AA and G418 as a selection medium. Cells were seeded 24h prior to the experiment at a concentration of $4x10^5$ cells/ml. Experiments were performed in phenol-red free, serum-free RMPI-1640.

5.3.2 AFM experiments

RAW cells were seeded on microscope slides cleaned with 70% ethanol, and incubated overnight, as described in section 5.2.1. Atomic force microscopy (AFM) experiments were performed at room temperature, using tapping mode AFM in fluid on a Bioscope I microscope (Veeco) with a MSCT-Au tip F cantilever (f_{res} ~ 130 kHz, k = 0.5 N/m). Data was analysed using SPIP (Image Metrology).

5.3.3 TIRF and HILO-OT experiments

The hybrid TIRF-OT setup described in chapter 2 was used to record single fluorescence images of RAW cells adhered to the microscope glass, with a DiI stained membrane, or covered with fluorescent beads. Table 5-2 gives the main settings for the described experiments. First, the RAW cells were incubated on the microscope glass. Then, a coverglass was positioned on the microscope glass, using a double layer of double-sided tape as a spacer at the long sides of the coverglass, inducing a channelled structure with the cells in medium.

The microscopy setup used for TIRF-OT experiments was also used for HILO-OT experiments. This time, the angle of incidence was set slightly smaller than the critical angle. The protocol for HILO-OT cell-cell experiments was as follows. First, RAW-ALCAM-GFP cells were incubated on a microscope slide primed for flowcells (section 2.6); one layer of double-sided 3M tape with a channel cut into it was attached to the microscope slide. A DAKO Pen was used to make a hydrophobic barrier between the medium with the cells and the double-sided tape. Second, a coverglass was cleaned with 70% ethanol and a layer of double-sided tape (with a channel) was attached to it. Third, the excess of medium on the microscope slide was removed, the coverglass was attached to the microscope slide (tape on tape), a syringe with a needle was connected to the inlet tube of the flowcell, and an outlet tube was connected. Fourth, medium was injected with a

syringe into the flowcell to fill it, after which medium with Jurkat-CD6-RFP cells in small aliquots of ~ 50 µl each were injected into the flowcell. A Jurkat-CD6-RFP cell was trapped with the OT (1064 nm; Millennia IR, SpectraPhysics, Newport). Before focussing the objective onto the dorsal side of the RAW-ALCAM-GFP cell and inducing direct cell-cell contact by this focussing, the Jurkat-CD6-RFP cell was first lowered in the optical trap. Then, the objective was focussed onto the dorsal side of the RAW-ALCAM-GFP cell and the TIRF illumination beam (Ar and ArKr, Coherent Inc.) aligned parallel to the focal plane of the objective. Next, acquisition of a time series of images was started and the trapped Jurkat-CD6-RFP cell was moved upwards to the RAW-ALCAM-GFP cell, in steps of 1 µm and with a speed of ~0.5 µm/s. The GFP was excited with 488 nm laser light, while the CD6-RFP was excited with 568 nm laser light. In order to minimize crosstalk between the GFP and RFP images, acquisition was done sequentially: first 568 nm, then 488 nm illumination. When the Jurkat-CD6-RFP cell membrane is in focus, stable cell-cell contact was assumed. This was set as t=0, the trap was not moved further, and turned off after ~ 300 s.

Table 5-2. Settings for TIRF-OT microscopy experiments

Setting	*Value*	*Remark*
488 nm laser intensity	~ 50 W/cm^2	Average intensity illuminated spot
568 nm laser intensity	~150 W/cm^2	Average intensity illuminated spot
1064 nm laser intensity	~500 mW	At back-aperture objective
Temperature stage	37 ºC	
Temperature objective	38.5 ºC	
Angle of incidence	~ 64 deg.	TIRF
	~ 61 deg.	HILO
Illumination time	100 ms	
Measurement frequency	1 or 0.33 Hz	
Filters	Notch 488 and Notch 568, 700 short pass, 560 dichroic mirror, 514/30 and 593/40 band pass	

As described in section 5.2.2, optimal HILO illumination requires a small beam, an angle close to the critical angle and perfect alignment to the contact site. In practice, the height, size and position of the contact site were not known beforehand, and fine-tuning of the positioning and angle was not trivial. Therefore, the HILO experiments described in the results section were performed with less

than optimal settings; that is, the beam was directed to the centre of the RAW-ALCAM-GFP cell, and the beam width was determined by Eq. 5.11, which can be derived from geometrical considerations requiring that the contact site should be within the FWHM of the beam (that is, at x=R the intensity is half of the maximum). This gives:

$$w = \frac{R + z\tan(\theta_t)}{\sqrt{2\ln 2}} \frac{\cos(\theta_i)}{\cos(\theta_t)} \qquad \text{Eq. 5.11}$$

When choosing R = 3 μm, z = 1 μm, and θ_i = 60 deg, this gives a minimum beam width $w \approx 21$ μm. This beam width corresponds to a full-width-half-maximum in the y direction of ($FWHM = 2\sqrt{2\ln 2}w$) ~ 50 μm, which should be the diameter of the spot on the microscope glass in y. This setting for w is used.

5.3.4 Data analysis of optical tweezers experiments

Data analysis of the time series of fluorescence images obtained with HILO-OT microscopy was done with DIPimage, a scientific image processing toolbox for Matlab (The MathWorks). Although the setup has been optimized to record images with the same focus, magnification and rotation on both EMCCD cameras, in practice, the overlap is not prefect. This means that a spot on camera 1 will not be at exactly the same pixel(s) on camera 2. For quantitative image analysis a perfect overlap would, however, be advantageous, for example for calculating the co-localisation of two fluorophores. Therefore, we determined the transformation of an image from camera 1 necessary to obtain a good overlap with an image from camera 2, as described in section 3.2.9). This transformation included rotation, translation and magnification of the pixels.

Ideally, the positions in the overlay image with both GFP and RFP fluorescence present could reveal the contact site. Here, we define the contact site as the place with ALCAM-GFP present and CD6-RFP present, which are presumably bound to each other. Since un-transfected Jurkat and RAW-ALCAM-GFP cells do not remain in stable contact (data not shown), this is a plausible assumption. However, we used HILO illumination with a wide Gaussian beam, and, therefore, ALCAM-GFP fluorescence at both ventral and dorsal sides of the RAW cells was imaged with high intensity and in focus. The segmented GFP-image, therefore, does

not directly provide information on the contact site. Therefore, we used the CD6-RFP images for image segmentation to determine the contact site. However, although section 5.2.2 explained that we do not detect out-of-focus light from the dorsal side of the Jurkat-CD6-RFP cell, out-of-focus light is detected from RFP on the side of the cell. This resulted in fluorescence images with considerable out-of-focus blur, hampering automatic segmentation as described in chapter 2. To obtain a suitable segmentation of the contact site, the first frame of the red fluorescence time series in which interaction was observed was manually segmented (determining the high intensity, in focus, spots as contact site). A smoothed version of this manual segmentation was used as a mask for segmenting the next frame and so forth. This segmentation method was based on the assumption that no large fluctuations and transitions occur from one frame to the next; after dilation of the mask from the previous frame, the new mask was set to the calculated isodata-threshold within the dilated mask minus 0.1 times the standard deviation in the intensity. This segmentation was similar to the observers view, and was used to segment both red and green fluorescence channels.

After segmentation, images were background corrected and the size of, and the mean intensity within the segmented area were determined. Furthermore, the Pearson's coefficient was determined as a measure for the co-localisation of RFP and GFP in the contact site. The Pearson's coefficient ranges from -1 to 1 and is a degree for the co-dependence of the channels; it measures the overlap of the pixels. The Pearson's coefficient makes a summation over all the pixels within the contact site:

$$p = \frac{\sum_{pixels}\left(I_{RFP,pixel} - I_{RFP,average}\right)\left(I_{GFP,pixel} - I_{GFP,average}\right)}{\sqrt{\sum_{pixels}\left(I_{RFP,pixel} - I_{RFP,average}\right)^2 \sum_{pixels}\left(I_{GFP,pixel} - I_{GFP,average}\right)^2}} \quad \text{Eq. 5.12}$$

When the Pearson's coefficient is 1, the signals in both channels vary in a correlated fashion, that is, when the signal in one channel varies from pixel to pixel, the signal in the other channel varies accordingly. The higher the p, the more correlated the signals are. When the Pearson's coefficient is negative, this means that when the signal in one channel increases, the signal in the other channel decreases. A p=0

indicates that the channels are not correlated, which is also the case if one of the channels does not vary (SVI-Hugens-Software, 2010).

Finally, the measured contact size, mean intensity of both channels, and calculated Pearson's coefficient calculated for each time frame were smoothed (10 points) and then averaged over 5 cell-cell interactions.

5.3.5 Micropipette experiments

Cell-cell interactions induced with a micropipette were measured on a confocal fluorescence microscope (LSM 510, Zeiss). The micropipette with its accompanying attributes is depicted in Fig. 5.6. A chambered coverslide (A; Labtec, NalgeNunc) was positioned in the 37 ºC heated stage (Harvard Apparatus). K562-ALCAM-GFP cells were injected in the well. A glass micropipette tip of ~ 1 μm diameter (B), made from a Borosilicate filament (OD 1.2 mm, ID .94 mm; Warner Instuments) on a pipette pulling apparatus (Sutter Intruments), was positioned in the capillary holder (C; Femtojet, Eppendorf)). The tip was brought close to a K562-ALCAM-GFP cell and by means of gentle suction with the syringe (E) connected through a pressure tube (D) was used to grab a cell at the tip of the pipette. The focus of the microscope was set to the dorsal side of a resting K562-ALCAM-GFP cell, and the optical slice thickness to 2 μm. The remote control of the micromanipulator (F; Olympus Narishige)) was used to position the micropipette-bound cell on top of the cell resting on the microscope glass slide; this was defined as the t=0 s point. Fluorescence images (256*256 pixels, 1.6 μs/pix) were taken every ~ 5 s. The sample was illuminated with 488 nm laser light (Argon, Lasos, 500 mW, used at 15 mW) via a HFT488 dichroic mirror. A 505 nm long pass filter was

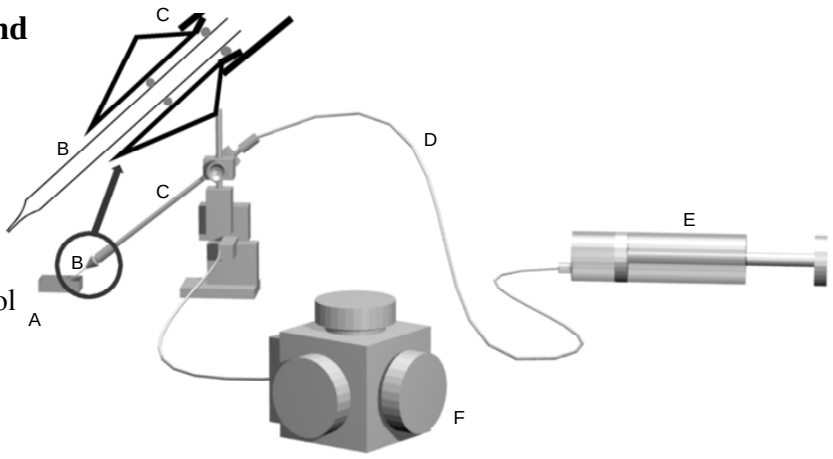

Fig. 5.6 Micropipette and micro manipulator
A) chambered coverslide, B) glass micropipette tip of ~ 1 μm diameter, C) capillary holder, D) pressure tube, E) syringe, F) remote control of the micromanipulator

positioned in the detection path.

The time series of images made on the confocal microscope were analysed similar to the HILO-OT data. First, a manual segmentation was performed on the first image. Second, DIPimage calculated the segmentation of the successive images based on the manual segmentation, the isodata-threshold and a standard deviation of 0.05%. After segmentation, the size and mean intensity in the segmented body were determined.

5.4 Results

This section describes the results of three different types of cell-cell experiments. First, TIRF illumination is used in combination with OT, addressing also the limitations of this technique. Second, a hybrid HILO-OT microscope is used for measuring cell-cell interactions, as a possible alternative for TIRF illumination. Finally, a micropipette is used on a confocal microscope to induce and measure cell-cell interactions. ALCAM-CD6 and ALCAM-ALCAM interactions will be used as a model system.

5.4.1 TIRF through an adhered cell

The challenge in using TIRF microscopy to visualize cell-cell interactions is in the excitation of the fluorophores at the contact site. Fig. 5.4B shows the intensity at different depths z. When the angle of incidence is larger than the critical angle (the condition for TIRF illumination), the intensity drops exponentially for increasing values of z (Eq. 5.8). Visualization of the contact site requires excitation of the fluorophores at the contact site of cell 1 and cell 2, through cell 1 (Fig. 5.7A). Although the exact distance for which fluorescence excitation can still be detected depends on the specific settings and sensitivity of the system used, this distance will be in the order of 300 nm[9]. Therefore, the part of cell 1 on which cell 2 is positioned should not be thicker than ~300 nm.

The focus of the research described in this thesis, is the interaction between dendritic cells (DCs) and T-cells. However, since DCs are difficult to culture and to

[9] Which is the penetration depth of the evanescent field for λ = 500 nm and θ_i slightly above the critical angle θ_c

transfect, we used RAW cells as a model system. RAW 246.7 cells are adherent mouse macrophages that can spread relatively thin on a substrate. Fig. 5.7B displays a TIRF image of RAW cells stretched on a microscope glass with a fluorescent membrane stain. This figure shows that RAW cells have long dendrites. In order to investigate whether these dendrites are thin enough to meet the requirement of a maximum thickness of ~300 nm, we measured the thickness with atomic force microscopy (AFM). Fig. 5.7C shows a white light overview image of measuring the topology of a RAW cell with AFM, and the resulting height profile along the line. The thickness of the dendrites is in the order of 300 nm. This indicates that TIRF excitation through these dendrites might be possible. In order to obtain a clean cell-cell contact, with only one contact site at the dendrite, the second, trapped cell has to be positioned onto these dendrites without interacting (first) with the thicker part of the cell, containing the nucleus.

To test whether excitation is possible, K562-ALCAM-GFP cells with a DiI stained membrane were trapped with OT and brought in contact with the RAW cells adhered to a microscope slide. No fluorescence of the GFP or DiI was visible (data not shown). For a second test, adhered RAW cells were covered with 100 nm beads and imaged with TIRF microscopy. Fig. 5.7D shows the TIRF image of two round cells and the dendrite of a third cell, all covered with fluorescent beads. The zoom-in has a different intensity scaling, but no beads are visible on the cells or dendrite. The fluorescent beads used for this test experiment are much brighter than an average fluorescent cell membrane. Therefore, we can conclude that TIRF is not possible through RAW cells. However, as described in the theory section (5.2), HILO illumination can overcome the problems due to a too thick cell 1.

5.4.2 ALCAM-CD6 interaction induced with optical tweezers

Using HILO illumination in combination with OT, the interaction between trapped Jurkat-CD6-RFP cells with RAW-ALCAM-GFP cells spread on a microscope glass was measured. A Jurkat-CD6-RFP cell was positioned at the peripheral part of a RAW-ALCAM-GFP cell, and a time series of GFP and RFP fluorescence images was collected. Fig. 5.8A shows the overlay of CD6-RFP fluorescence images and ALCAM-GFP fluorescence images at various time points.

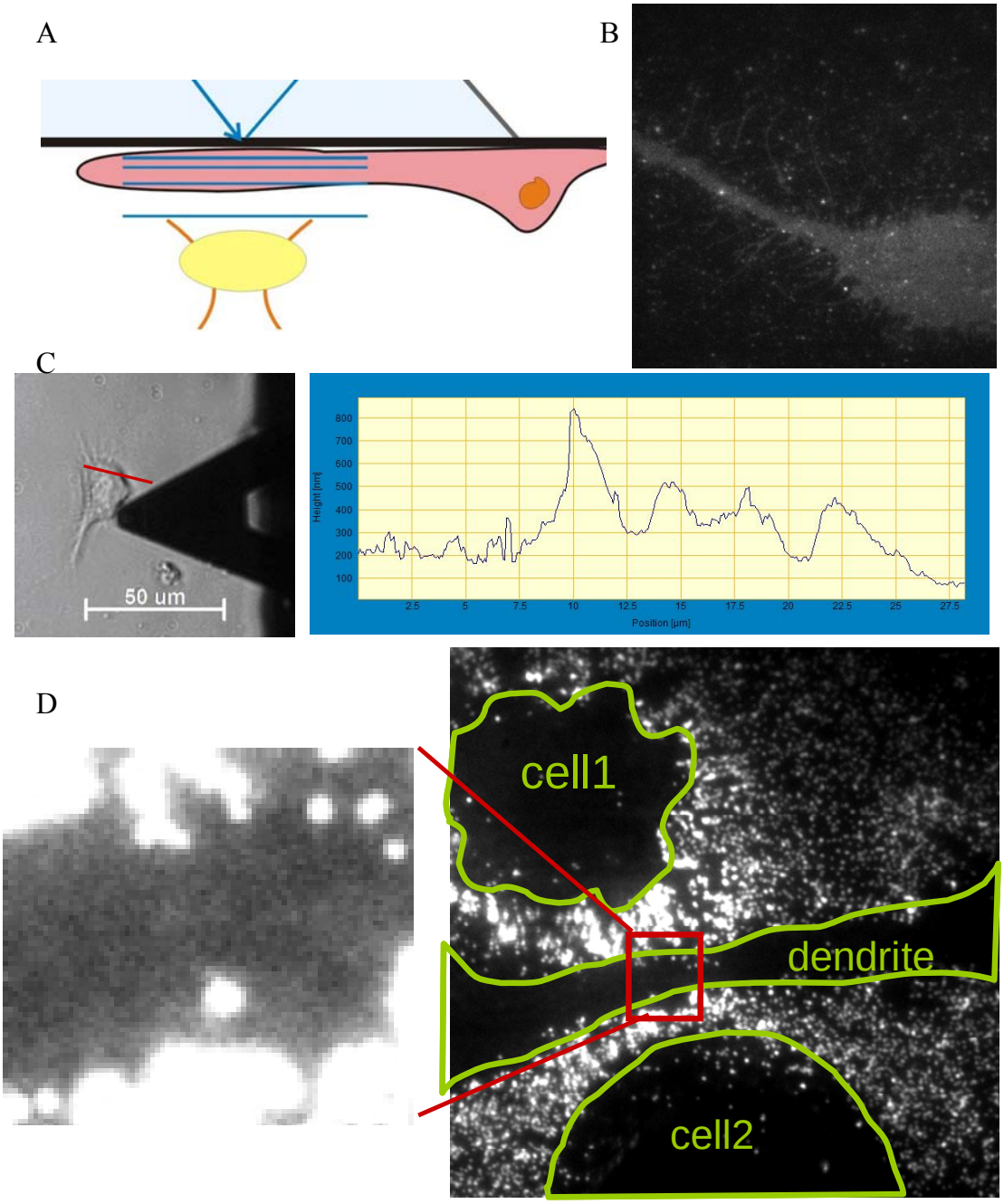

Fig. 5.7 TIRF microscopy through a cell

(A) Schematic representation of TIRF-OT microscopy for cell-cell interaction. The image is not to scale. The yellow, trapped cell has to be excited through the pink adhered cell by the exponentially decaying evanescent field. (B) TIRF image of RAW cell, with a DiI stained membrane (~50*50 µm). (C) AFM image of a stretched RAW cell, overview and height profile along the line. (D) TIRF image of three RAW cells covered with 100 nm fluorescent beads (~50*50 µm), and zoom-in of dendrite of cell 3 has a different intensity scaling to reveal any low intensity fluctuations at the dendrite.

The intensity scaling is different between the first and the last two rows. In the images, an increase in fluorescent intensity and an increase in colocalisation of the GFP and RFP can be observed. Fig. 5.8A demonstrates that the combination of HILO and OT can be used with versatility in measuring cell-cell interactions.

To quantify the changes in fluorescence, a semi-automated segmentation of the fluorescence intensity distribution was performed, as described in section 5.3.4. Then, the size of, and mean intensity in, the contact site were determined, together with the Pearson's coefficient, for every time frame. Fig. 5.8B-D show these measures (averaged over 5 cell-cell interactions) plotted against time, where the black lines give a measure for the contact site in total, the red solid line gives RFP specific measures and the green dashed line GFP specific measures. The mean intensity at the contact site (Fig. 5.8B) is a measure for the recruitment of ALCAM-GFP and CD6-RFP to the contact site. The graph shows some increase in mean intensity of the RFP, indicating recruitment, but not for GFP. It should be noted, however, that this data has only been corrected for the background signal and not for photobleaching. Assuming that the interaction of ALCAM and CD6 is stable and long-lived (te Riet et al., 2007), the GFP and RFP will be subjected to bleaching and the data might show an accumulation of CD6-RFP and ALCAM-GFP at the contact site. The observed lower increase in the ALCAM-GFP channel can be due to different photobleaching characteristics of GFP and RFP. Another possibility is that there is no recruitment of ALCAM because there is already an excess of ALCAM at the contact site, or that ALCAM is responding differently in RAW cells than in ALCAM's natural cell environment.

Fig. 5.8C shows the size of the contact site over time. As addressed in section 5.3.4, the contact site is defined as the position of in focus RFP fluorescence, assuming CD6-ALCAM is the only tight connection between the RAW-ALCAM-GFP cells and the Jurkat-CD6-RFP cells. The figure shows a decrease in contact size, opposed to the cell-substrate experiments described in previous chapters.

The Pearson's coefficient was calculated as a measures for the co-localisation of the fluorescence signal of CD6-RFP and ALCAM-GFP are calculated (Fig. 5.8D) An increase in the Pearson's coefficient is observed, indicating that upon contact CD6-RFP and ALCAM-GFP signals start to vary in a

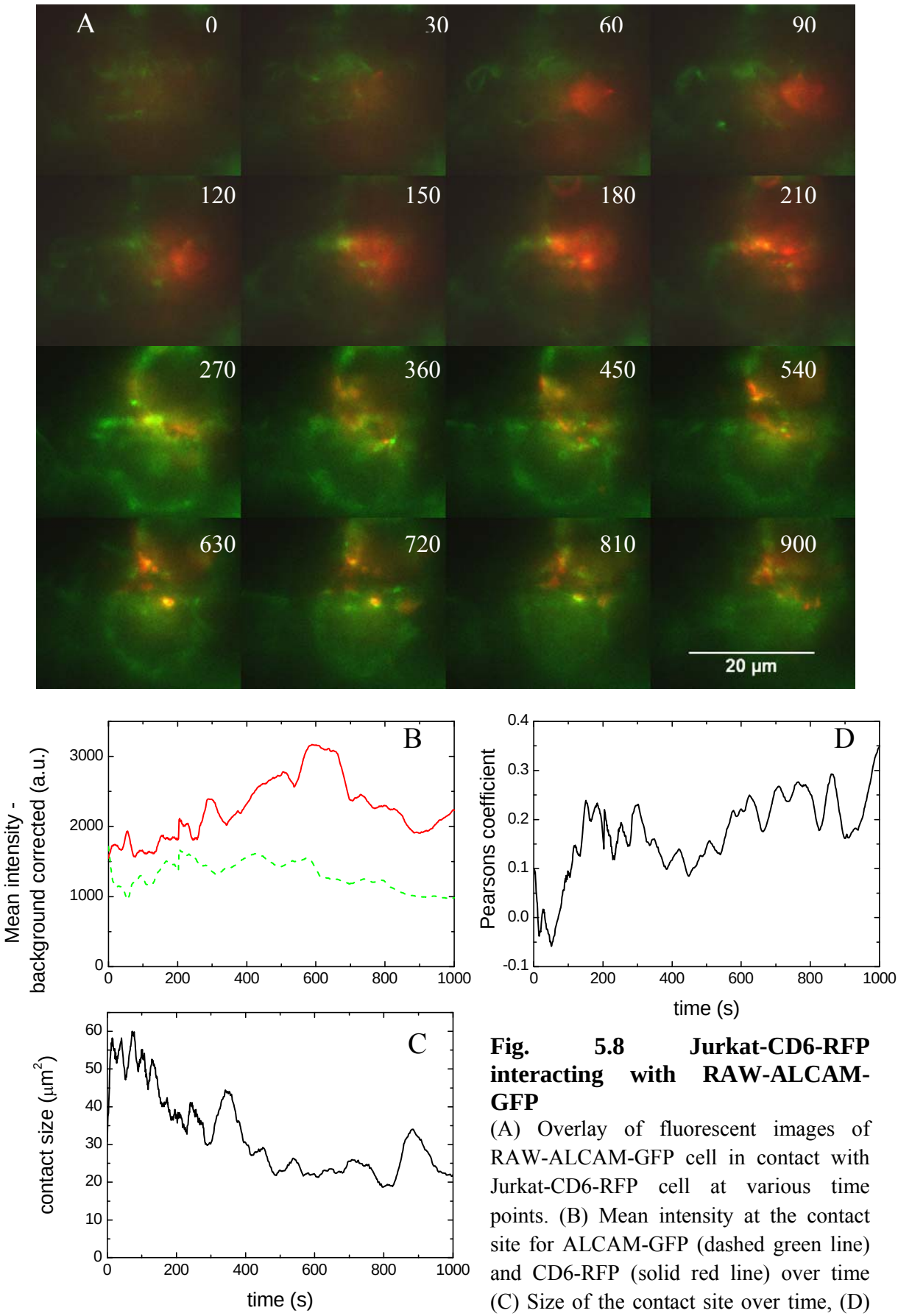

Fig. 5.8 Jurkat-CD6-RFP interacting with RAW-ALCAM-GFP

(A) Overlay of fluorescent images of RAW-ALCAM-GFP cell in contact with Jurkat-CD6-RFP cell at various time points. (B) Mean intensity at the contact site for ALCAM-GFP (dashed green line) and CD6-RFP (solid red line) over time (C) Size of the contact site over time, (D) Pearsons coefficient in the contact site

similar way with a maximum after ~140 s. Fig. 5.8D suggests that in the first 100-150 s of contact, the largest variations in ALCAM-GFP and CD6-RFP dynamics occur.

5.4.3 ALCAM-ALCAM interaction induced with micropipette

In the previous section, we used optical tweezers for positioning cells on top of each other. However, optical tweezers require a sophisticated microscopy setup, which is not available in every lab. Therefore, we discuss the use of a micropipette for micro positioning of a cell, in combination with a confocal fluorescence

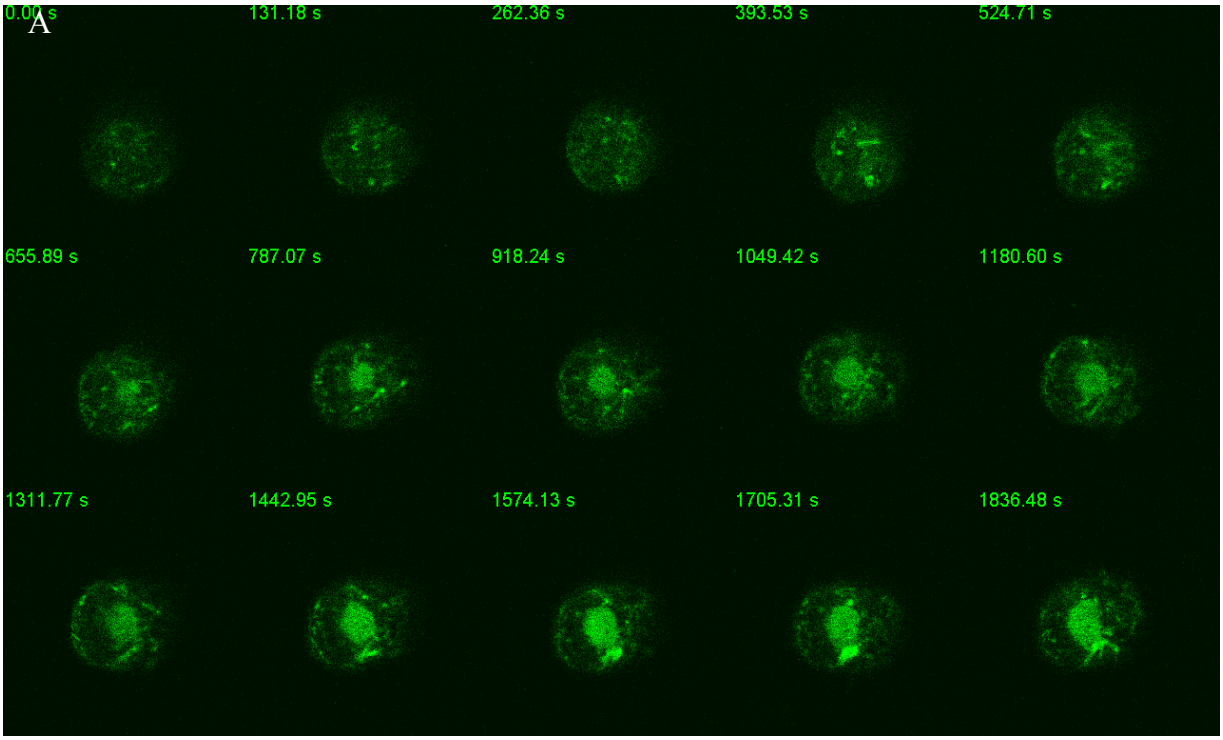

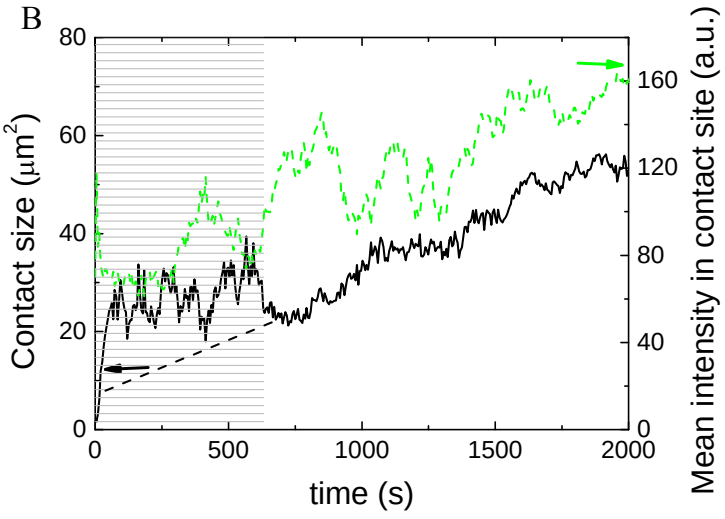

Fig. 5.9 ALCAM-ALCAM interaction induced with micropipette
A. Confocal fluorescence microscopy images of two K562-ALCAM-GFP cells interacting with each other in the plane of focus, brought in contact at t=0s by a micropipette. B. Contact size (left y-axis, black solid line) and mean intensity in the contact site (right y-axis, green dashed line) over time.

microscope, in this section.

Fig. 5.9A shows fluorescence images of two K562-ALCAM-GFP cells that are positioned on top of each other with a micropipette. The contact site is in the focal plane of the objective, which had an optical slice thickness of 2 μm. The images show the initiation and continuation of a circular contact site, with homogenous distribution of ALCAM-GFP. This ALCAM-GFP is transported towards the contact site in small clusters.

Data analysis of this time series of images quantified the increase in contact size (black solid line) and the intensity in the contact site (green dashed line), over time, as is plotted in Fig. 5.9B. For timeframes <650 s, the fluorescence varied too much in space and time, hampering the segmentation. Therefore, at these timeframes, the contact size and mean intensity within the contact size were not properly determined, indicated in Fig. 5.9B with the gray area. For timeframes >650 s, the segmentation process found a contact site as the observer would define it. The contact size in this first period might be more correctly represented by the black dashed line than by the black solid line, where the dashed line gives a linear extrapolation of the curve for timeframes <650 s. After ~650 s a circular contact site is initiated and the segmentation improved. The mean intensity in the contact site is not corrected for photobleaching. However, it is clear that ALCAM is recruited towards the contact site, giving rise to an increase in mean intensity. The time for this recruitment seems ~ 1500 s, after which the mean intensity graph reaches a plateau.

5.5 Discussion and Conclusion - Method

In this chapter, we investigated three methods to monitor and control cell-cell interactions. In the first place, we have shown that simulations can predict the number of cell-cell interactions based on probability of interaction, when cells are added into the same volume. However, this only gives a limited control: the number of interactions can be tuned, the starting point can be estimated, but the positioning of the interaction plane is not controlled. In the final stage, cells are next to each other, not giving a horizontal interaction plane (data not shown). TIRF excitation at the contact site of cell-cell interactions was not possible, because of the thickness of the cell adhered to the microscope glass. Although Sako et al. describe the

excitation by TIRF on the dorsal side of a cell in contact with the microscope glass (Sako et al., 2000), this method would not create an evanescent field in cell-cell interactions since no refractive index change would be present at the interface between the cells. The combination of HILO and OT enabled visualisation of the contact site together with control in both space and time in the positioning of the cell-cell interaction. In the third place, the combination of a micropipette with confocal fluorescence microscopy resulted into a fruitful method, again enabling control over the starting point of interaction and the interaction plane.

A limitation of the two last methods is the throughput. Since both methods are imaging cell-cell interactions in a serial manner, the amount of cell-cell interactions measured in a certain amount of time is limited by the time a single cell-cell contact is monitored. As a possible approach to increase throughput, a method with random seeding of the cells was discussed were the probability of an interaction is based on chance (section 5.2.1). However, with an average expected number of 6 single cell-cell interactions in the field of view, we showed that this method does not increase throughput much. When this method is implemented together with microwells, the limitations of the position of the contact site and the horizontal alignment of the contact site could possibly be overcome and this method might have a small throughput-advantage. Rosenbluth et al. (2006) describe a method to make microwells and position one cell per well. A device could be designed with small enough wells, so cells can not fall next to each other, and deep enough wells, so both cells fit in. In this way, multiple cell-cell interactions could be monitored in parallel in the focal plane.

Another possibility to study cell-cell interactions is a hybrid between the second and third method; a confocal microscope could be combined with optical tweezers. This has two advantages. In the first place, OT do not physically touch the cell membrane as the micropipette does. This contact of the micropipette with the cell might influence the mobility of the membrane molecules. The OT, furthermore, are using the same objective as the illumination light and do not require positioning of an external object. Since the micropipette is not positioned next to the microscope, a drift by the microscope (stage) can result in a misalignment of the micropipette with respect to the cell at the bottom (as can be observed as well in Fig. 5.9A). In the second place, confocal microscopy does not require detailed

optimization of the angle of incidence, and the position and width of the beam, as does HILO (section 5.2.2). With objective-based HILO microscopy, the light is focused on the back focal plane of the objective, resulting in a parallel beam in the sample. The angle of this beam in the sample depends on the distance between the optical axis and the position of the focus at the back aperture. When the incident beam of objective-based HILO is directed parallel to the optical axis, the beam in the sample will always be through the centre of the specimen plane. In practice, this means that when the contact site is in focus in the centre of the specimen plane, it will be illuminated. However, the method described and tested in this chapter, is prism-based TIRF. To guide the thin excitation beam properly to the contact site, so the P_{z1}/P_{z0} ratio is high (section 5.2.2), the position of the Gaussian beam at the microscope slide, determined by the *x,y*-position and depth of the contact site, is critical. Therefore, confocal microscopy is a less challenging to implement visualization technique. Especially, when a spinning-disk confocal microscope is used, the trade off for not using a CCD-camera as with TIRF and HILO microscopy, but an APD, might not be too high. This combination of spinning-disk confocal microscopy with optical tweezers has been described to study cell-cell interactions (McNerney et al., 2010). However, McNerney et al. still make a stack and have not used the optical tweezers to align the contact site to the field of view, in order to obtain higher spatial resolution. Furthermore, it could even be investigated whether it is possible to implement two optical tweezers, holding the cell each at a different axial position. In this configuration none of the cells would physically touch a glass surface, which possibly influences dynamics.

Table 5-3 summarizes the main characteristics of the control and visualisation methods described and tested in this chapter. All techniques have advantages and disadvantages. Preferably, the method to study cell-cell interaction should combine all the advantages, that is, all the highest scores in the table. This is best achieved by combining optical tweezers with spinning disk confocal microscopy, which is only limited in the throughput per unit time. Maybe holographic optical tweezers, using acousto-optic elements to create multiple individual traps, could be an option to overcome this issue. To conclude, we recommend exploring the combination of optical tweezers with confocal microscopy for studying cell-cell interactions from t=0s on.

Table 5-3. Controlled and quantitative visualisation of cell-cell interactions

Method / ***Measure***	***Random seeding***	***OT***	***Micropipette***
Throughput (interactions measured per time unit)	6x, higher for microwells?	1	1
Throughput (total number of measurements in configuration)	1, new well needed for every measurement	No limits in flowcell	Few times, then the well will be full
Precision positioning (x,y,z)	Only in microwells	~ 1 μm	~ 1 μm
Precision t=0 determination	Depends on measurement frequency	~2 s	Seconds
	TIRF	**HILO**	**Confocal microscopy**
Signal-to-background	Max. 0.5 for very thin cell 1 (Fig. 5.4A)	>1	>1
Measurement frequency	High; 35 Hz full frame	High; 35 Hz full frame	Low; ~1 Hz; high for spinning disk confocal microscope
Resolution	Diffraction limit (x,y) and depth of focus (DOF) in (z)	Diffraction limit (x,y) and depth of focus (z)	~0.7 * diffraction limit (x,y) and ~ 0.7 * DOF (z)
Implementation	Feasible, but only prim-based in combination with OT	Prim-based HILO difficult to optimize	Feasible & commercially available

5.6 Conclusion and Discussion – ALCAM and CD6

In this chapter, we used ALCAM-ALCAM and ALCAM-CD6 interactions to study the versatility of HILO-OT and micropipette-CLSM methods for cell-cell interaction studies. We observed in both ALCAM-ALCAM and ALCAM-CD6 interactions a change in fluorescence distributions at the contact site upon interaction. Although further investigations are necessary, we will hypothesize below about the reasons and consequences of our observations. Fig. 5.8 shows the

dynamics upon interaction between ALCAM and CD6. We observed a decrease in the size of the contact site (Fig. 5.8C). A possible reason for the fact that we do not observe an increase in contact size between RAW-ALCAM-GFP and Jurkat-CD6-RFP cells might be the hanging configuration as discussed in chapter 4. Since only CD6 and ALCAM contribute to a stable binding of these cells, the gravitational force might limit increase of the contact site. Besides, it has to be validated for cell-cell experiments whether CD6-RFP and ALCAM-GFP are correct measures for the size of the contact site. Furthermore, we observe an increase in mean intensity of the RFP, indicating that RFP is recruited towards the contact site (Fig. 5.8B). The ALCAM-GFP does not seem to be recruited towards the contact site, since the mean intensity does not increase. Most interesting is probably the increase in the Pearson's coefficient, which shows that the spatial distribution of ALCAM-GFP and CD6-RFP upon interaction is correlated (Fig. 5.8D). Together, this data hints to a model that upon interaction CD6 (and possibly ALCAM) is recruited towards the contact site, and, furthermore, that ALCAM and CD6 (either already present at the contact site or newly recruited) are reorganized in the contact site to obtain a correlated spatial distribution. With the current available data, we cannot discriminate between active recruitment of CD6 or passive (by diffusion), and we can not elaborate on whether the spatial reorganisation is only CD6 rearranging to existing ALCAM, or that both proteins are rearranging. However, Fig. 5.8A suggests the latter. Further experiments could elaborate more on these recruitment and rearranging processes, for example on the role of the actin cytoskeleton in this.

Data analysis on the interaction of ALCAM with ALCAM (Fig. 5.9) shows that the size of the contact site is increasing and that ALCAM is recruited towards the contact site (Fig. 5.9B), possibly in clusters (Fig. 5.9A). Table 5-4 summarizes the results obtained in this chapter, and compares these with results from cell-surface experiments (chapters 3 and 4) and cell-cell experiments by Zimmerman et al. (2006). Comparing the results, we observe that in all situations ALCAM and/or CD6 are recruited towards the contact site. Furthermore, strong spreading is observed for cells interacting with surfaces, but slower or not at all for cell-cell interactions. It is difficult to relate the generally faster recruitment process to the slower spreading process. However, both spreading and recruitment might be processes aimed to increase the number of available binding sites. Possibly

recruitment and spreading are two competing processes; when larger spreading is observed, recruitment (defined by the mean pixel intensity) might be lower. It is complex to separate these processes in the data analysis. Therefore, Spendier et al. (2010) use a micropipette to initiate cell contact with a functionalized substrate resulting in a large initial contact site. A micropipette can exert high enough forces to press the cell against the substrate (Hocde et al., 2009). This allowed studying the distribution of membrane molecules at small timescales, assuming cell spreading is negligible in this situation. Another, elegant experiment to address this issue is the use of patterned surface. Then, the size of the contact site can be controlled by the size of the patterns, while the redistribution and recruitment of molecules can be measured.

Table 5-4. Results on ALCAM and CD6 interactions

Interaction / *Measure*	*ALCAM-surface (Ch. 3)*	*ALCAM-ALCAM*	*CD6-surface (Ch. 4)*	*CD6-ALCAM*
Contact size – measured (time constant)	Increasing, ~330s	Increasing, ~1500 s	Increasing, ~435 s	Decreasing
Recruitment – measured	?	Yes, finished in ~1500 s	Yes, continuous	Yes, most likely
Recruitment – x (Zimmerman et al., 2006)		Start after ~6 min, finished in ~10 min.		Start after ~6 min, finished in ~13 min.
Distribution – measured	Homogenous, time constant ~30s	First spots, then homogenous	Homogenous	Spots ?

One point to take into consideration, comparing the different results, is the difference in cell types used. We performed ALCAM-CD6 experiments in RAW cells (mouse macrophage) with Jurkat cells (human T-cell line), while the reported experiments by Zimmerman are between K562 cells (human myeloid leukaemia line) and Jurkat cells. The association of ALCAM or CD6 with other molecules in the cells and the signalling in the cell might be influenced by the cell types used. Especially the recruitment and distribution of ALCAM on RAW cells might differ with respect dendritic cells, which express ALCAM endogenously. This might

influence the size of the contact site and the absolute numbers of the recruitment towards the contact site.

Another point of consideration is the measurement configuration. The recruitment index as calculated by Zimmerman et al. is based on images with the contact site perpendicular to the focal plane. Although it should be noted that both Zimmerman et al. and we only present one example, the observed differences in the time scale for ALCAM-ALCAM induced recruitment support our statement that precise measurement of membrane dynamics requires a method in which the contact site is in the focal plane.

As a next step, it would be interesting to transfect dendritic cells with fluorescent ALCAM and redo the ALCAM-CD6 experiments. Since dendritic cells spread strongly, they might furthermore be thin enough to use TIRF illumination. This would improve the signal-to-background ratio in the red channel and would enable fully automated segmentation of the contact site, improving the objectivity of the data analysis. However, as stated in section 5.5, the combination of optical tweezers and confocal microscopy would be the preferred method to apply in the first instance. Using ALCAM-GFP transfected dendritic cells and Jurkat-CD6-RFP cells, it would be possible to obtain relevant quantitative measures for the ALCAM and CD6 dynamics.

References

ALFSEN, A., YU, H., MAGERUS-CHATINET, A., SCHMITT, A. & BOMSEL, M. 2005. HIV-1-infected Blood Mononuclear Cells Form an Integrin- and Agrin-dependent Viral Synapse to Induce Efficient HIV-1 Transcytosis across Epithelial Cell Monolayer. Mol. Biol. Cell, 16, 4267-4279.

AXELROD, D. 2007. Total Internal Reflection Fluorescence Microscopy. Optical Imaging and Microscopy. Berlin: Springer Berlin/Heidelberg.

DUSTIN, M. L. 2009. The Cellular Context of T Cell Signaling. Immunity, 30, 482-492.

GROVES, J. T. & DUSTIN, M. L. 2003. Supported planar bilayers in studies on immune cell adhesion and communication. Journal of Immunological Methods, 278, 19-32.

HOCDE, S. A., HYRIEN, O. & WAUGH, R. E. 2009. Cell adhesion molecule distribution relative to neutrophil surface topography assessed by TIRFM. Biophys J, 97, 379-87.

KAIZUKA, Y., DOUGLASS, A. D., VARMA, R., DUSTIN, M. L. & VALE, R. D. 2007. Mechanisms for segregating T cell receptor and adhesion molecules during immunological synapse formation in Jurkat T cells. Proc Natl Acad Sci U S A, 104, 20296-301.

LIDKE, D. S. & WILSON, B. S. 2009. Caught in the act: quantifying protein behaviour in living cells. Trends in Cell Biology, 19, 566-574.

MCNERNEY, G. P., HUBNER, W., CHEN, B. K. & HUSER, T. 2010. Manipulating CD4(+) T cells by optical tweezers for the initiation of cell-cell transfer of HIV-1. Journal of Biophotonics, 3, 216-223.
MEDDENS, M. 2009. Microcontact printing to study the role of CD6 in T cell activation. Master thesis, University of Twente.
MOSSMAN, K. D., CAMPI, G., GROVES, J. T. & DUSTIN, M. L. 2005. Altered TCR signaling from geometrically repatterned immunological synapses. Science, 310, 1191-1193.
NAKANO, A. 2002. Spinning-disk confocal microscopy -- a cutting-edge tool for imaging of membrane traffic. Cell Struct Funct, 27, 349-55.
NELISSEN, J. M. D. T., PETERS, I. M., DE GROOTH, B. G., VAN KOOYK, Y. & FIGDOR, C. G. 2000. Dynamic regulation of activated leukocyte cell adhesion molecule-mediated homotypic cell adhesion through the actin cytoskeleton. Molecular Biology of the Cell, 11, 2057-2068.
ODDOS, S., DUNSBY, C., PURBHOO, M. A., CHAUVEAU, A., OWEN, D. M., NEIL, M. A. A., DAVIS, D. M. & FRENCH, P. M. W. 2008. High-Speed High-Resolution Imaging of Intercellular Immune Synapses Using Optical Tweezers. Biophysical Journal, 95, L66-L68.
OLYMPUS. 2010. Olympus FluoView Resource Center: Theory of confocal microscopy www.olympusfluoview.com [Online]. [Accessed].
PAWLEY, J. B. 1990. Handbook of biological confocal microscopy, New York, Plenum.
ROSENBLUTH, M. J., LAM, W. A. & FLETCHER, D. A. 2006. Force microscopy of nonadherent cells: A comparison of leukemia cell deformability. Biophysical Journal, 90, 2994-3003.
SAKO, Y., MINOGHCHI, S. & YANAGIDA, T. 2000. Single-molecule imaging of EGFR signalling on the surface of living cells. Nature Cell Biology, 2, 168-172.
SPENDIER, K., CARROLL-PORTILLO, A., LIDKE, K. A., WILSON, B. S., TIMLIN, J. A. & THOMAS, J. L. 2010. Distribution and Dynamics of Rat Basophilic Leukemia Immunoglobulin E Receptors (Fc epsilon RI) on Planar Ligand-Presenting Surfaces. Biophysical Journal, 99, 388-397.
SVI-HUGENS-SOFTWARE. 2010. http://support.svi.nl/wiki/ [Online]. [Accessed].
TE RIET, J., ZIMMERMAN, A. W., CAMBI, A., JOOSTEN, B., SPELLER, S., TORENSMA, R., VAN LEEUWEN, F. N., FIGDOR, C. G. & DE LANGE, F. 2007. Distinct kinetic and mechanical properties govern ALCAM-mediated interactions as shown by single-molecule force spectroscopy. J Cell Sci, 120, 3965-3976.
TOKUNAGA, M., IMAMOTO, N. & SAKATA-SOGAWA, K. 2008. Highly inclined thin illumination enables clear single-molecule imaging in cells (vol 5, pg 159, 2008). Nature Methods, 5, 455-455.
ZIMMERMAN, A. W., JOOSTEN, B., TORENSMA, R., PARNES, J. R., VAN LEEUWEN, F. N. & FIGDOR, C. G. 2006. Long-term engagement of CD6 and ALCAM is essential for T-cell proliferation induced by dendritic cells. Blood, 107, 3212-20.

Appendix 5A. K562-ALCAM-GFP cell characteristics

We measured the characteristics of K562-ALCAM-GFP cells moving downwards in a well due to gravity.

Materials and Methods

Cells were added in a Labtec chambered coverglass on a confocal microscope. The focal plane was set 50 μm above the well surface. A time series of images was recorded. The cell diameter (D_c) was measured, and the time the cells entered and leaved the focal plane, which gave an estimate for the elapsed time (t_{last} - t_{first}). Assuming the cell is a homogenous sphere submersed in water, we can determine the following:

Velocity of the cell (v_c) : $v_c = \frac{D_c}{(t_{last} - t_{first})}$

Buoyancy force on the cell: $F_B = V \rho_w g$, with the cell volume $V = \frac{4}{3}\pi r^3$ and ρ_w=1000 kg/m^3

The gravitational force experienced by the cell is: $F_G = -V\rho_c g$

The drag force through viscous medium is: $F_D = 6\pi\eta r v$, with η the viscosity of the medium ($\eta = 1,0 \cdot 10^{-3}$ Pa · s for water), v the velocity and r the radius.

Assuming the net force on the cell is zero, this gives $(\rho_c - \rho_w) = \frac{6\pi\eta r v}{Vg}$.

Results

The velocities of 22 cells were determined and plotted in a histogram (Fig. 5A1). The median cell velocity is approximately 2.7 μm/s. Table 5A gives the determined cell characteristics.

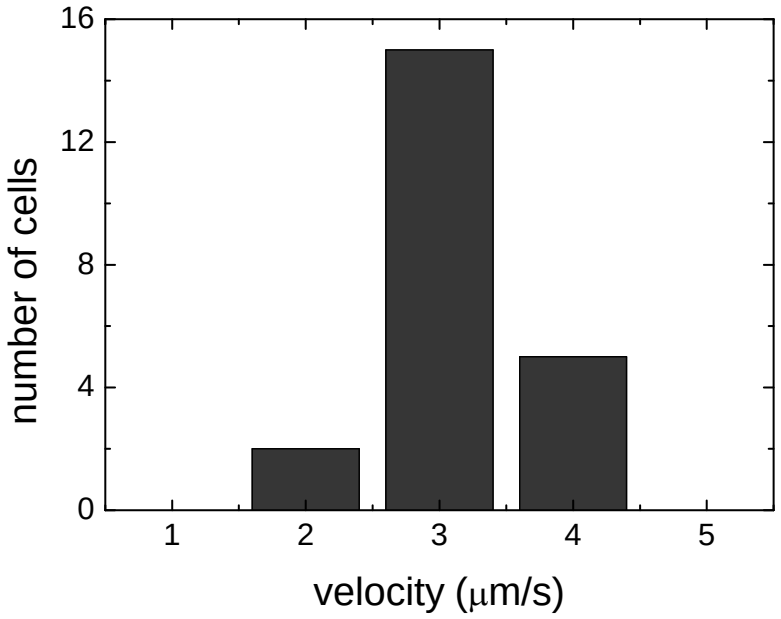

Fig. 5A1 Histogram of 22 cell velocities

Table 5A: The properties of a typical K562 cell

Diameter	*Velocity*	*Volume*	*Density*	*Mass*
15 μm ± 3 μm	2.7×10^{-6} m/s	1.8×10^{-15} m^3	1.024×10^{3} kg/m^3	1.8×10^{-12} kg

Chapter 6 –

Conclusions and Outlook

6.1 Conclusions

6.1.1. Method related conclusions

We have developed a method that can monitor cell-substrate and cell-surface interactions in a controlled and quantitative manner. The method is based on total internal reflection fluorescence (TIRF) microscopy, allowing a high selectivity in the axial direction and providing high signal-to-background images. To control the onset of interaction and to position the interaction site in the field of view, we used optical tweezers (OT) to capture and spatially manipulate a cell. The two main requirements for the method developed were to have the interaction site aligned parallel to the focal plane of the objective (for high spatial resolution) and to visualize the interaction from the precise time point of onset of the interaction.

We demonstrated that a hybrid prism-based TIRF-OT microscope could be built with an optical trap that is steerable independent of the focus of the objective. We characterized this combination, and measured that the trap has a lateral accuracy of 10 nm, and is able to move a trapped cell with an axial speed of ~ 0.5 μm/s. We could determine the onset of the interaction with a temporal accuracy of ~ 2 s. We visualized the interaction with a ~ 250 nm lateral resolution (diffraction limit) and ~ 300 nm axial resolution (extent of the detected evanescent field). Data analysis of the fluorescence images recorded was able to reveal the contact site based on the quantitative measures of the observed fluorescence. We demonstrated that we could measure the increase in the size of the contact site over time for cell-substrate interactions, the mean intensity in the contact site (a measure for the number of fluorophores present in the contact site), and the homogeneity of the fluorescence in

the contact site (a measure for the distribution of the membrane molecules in the contact site). Since the onset of interaction was determined accurately, it was possible to average the data acquired from several cells to limit the influence of cell-to-cell variations.

We used this TIRF-OT microscopy combination to measure the interaction of cells with a functionalized surface, which revealed interesting insights into the dynamics of the membrane proteins ALCAM and CD6 upon interaction. Additionally, we observed that the hanging configuration of prism-based TIRF microscopy combined with OT is more sensitive to changes in the cell, and furthermore, influences the characteristic time of cell spreading. Since TIRF microscopy of cell-cell interactions proved to be difficult, we tested two other possible combinations. We demonstrated in a proof-of-principle experiment the versatility of combining HILO microscopy with OT, and of combining micropipettes with confocal microscopy to study cell-cell interactions. We demonstrated that the throughput of micropipette or OT experiments is ~6x lower than for random seeding experiments, but that the latter approach does not provide control over the alignment of the interaction site to the field of view.

6.1.2. Biology related conclusions

We studied in a dynamic manner the interaction of the activated leukocyte cell adhesion molecule (ALCAM) and its ligand CD6, both membrane proteins involved in the adaptive immune system. We showed that K562-ALCAM-GFP cells spread on a surface functionalized with CD6. This spreading behaviour is in accordance with an existing model (Chamaraux et al., 2005), which is based on the force balance between the cell membrane tension and actin polymerization. Additionally, we described an active redistribution of ALCAM upon contact initiation with a characteristic time of ~35 s. The latter redistribution time constant is ~ 10 times smaller than the spreading time constant. Therefore, we concluded that spreading, recruitment and redistribution might be different processes, which require more detailed study of the underlying mechanisms (like cytoskeleton involvement).

In addition, the hybrid TIRF-OT method developed was used to investigate the CD6-induced cell spreading and recruitment of CD6 towards the contact site in

the interaction between Jurkat-CD6-RFP cells and a functionalized surface. We showed that Jurkat-CD6-RFP cells spread on anti-CD6 functionalized surfaces with a characteristic time of 435 s, similar to K562-ALCAM-GFP cells on CD6 functionalized surfaces. Furthermore, we showed by cytoskeleton disruption that the actin cytoskeleton is involved in CD6 induced cell spreading. Moreover, we measured recruitment of CD6 towards the contact site, on anti-CD6 and non-CD6 specific functionalized surface. This recruitment is an active process. We suggested a model in which upon contact with a surface, the actin cytoskeleton is polymerized towards the contact site, delivering the CD6 or dragging the CD6 along. Once at the contact site, the increased actin concentration induces cell spreading.

Finally, in the proof-of-principle cell-cell experiments we observed an increase in the contact site for ALCAM-ALCAM interaction between cells, but not for ALCAM-CD6 interactions. We also observed recruitment of ALCAM to the ALCAM-ALCAM interaction site and CD6 recruitment to the ALCAM-CD6 interaction site. Further experiments should provide more robust statistics and insights into the processes underlying these dynamics.

6.2 Outlook

6.2.1. Instrumentation

Throughput of cell-substrate experiments

Hybrid TIRF-OT microscopy is able to induce and visualize cell-substrate interactions. However, only one cell at the time can be positioned on the functionalized glass surface and measurements of multiple cells have to be performed in a sequential manner. Therefore, it is recommended that for biological experiments that require a high throughput to implement objective based TIRF and let the cells settle by gravity. When a CCD camera is used with more pixels (e.g. 1024*1024 pixels with 100 nm/pixel), it is possible to have multiple cell-substrate interactions in the field of view (e.g. ~ 30 individual cells). In this situation, the onset of interaction can be determined afterwards for each cell by image and data analysis. This would combine the high signal-to-background advantage of TIRF microscopy with higher throughput.

Imaging cell-cell interactions

Cell-cell interactions can be monitored with highly inclined laminated optical sheet (HILO) microscopy and confocal microscopy. Both methods are able to reduce out-of-focus light, and therefore have a high signal-to-background ratio. The advantage of confocal microscopy is that commercial setups are available, even with high frame rates (~50 Hz full frame for spinning-disk confocal microscopy). Since the advantage of optical tweezers over the use of a micropipette is that OT do not physically touch the cells, we recommend to implement (multiple) optical tweezers with spinning disk confocal microscopy. This would enable high-throughput and high signal-to-background imaging of cell-cell interactions, right from the onset of interaction.

Manipulation

Cell-cell interactions can be induced by random seeding, where cells sediment under gravity, or by the use of optical tweezers or a micropipette. As discussed in chapter 5, random seeding does not provide control over the alignment of the interaction site to the field of view. If the higher throughput of random seeding is advantageous for the cell-cell experiments of interest, it is recommended to combine the random seeding method with a microwell array. In this microwell array, cells are aligned by the walls of the well. Most likely, this procedure will only be suitable for non-adherent, spherical cells. The most optimal control over the onset, position and alignment of cell-cell interactions, however, is achieved by optical tweezers.

An interesting improvement with respect to the manipulation by optical tweezers might be the implementation of multiple optical traps that could improve the throughput by trapping more cells simultaneously and bringing them to the interaction surface. Also the interaction of a single cell with multiple other cells could be studied. To this end, multiple trapped cells of type B could be positioned on one cell of type A situated at the surface. Furthermore, it might be possible to separately trap a single cell A and a single cell B, and bring them in contact without any physical interaction with a (glass) surface. This would enable the study and quantification of the possible influence of such a surface on the dynamics of the membrane proteins in the interaction site.

Forces in the optical trap

Optical tweezers can be used as force transducer, by measuring the deflection of the infrared beam. Therefore, it would be interesting to implement a detection path for the infrared beam. For prism-based TIRF this should be a detection path in an IR-reflection based manner, as described by (Huisstede et al., 2005). It would be useful to have a sensor that could measure the force experienced by a trapped particle upon interaction with a cell. This could, for example, provide new insight in the mechanism and forces related to the (possible) interaction between CD6 and the cytoskeleton. Because of the inhomogeneity of cells, force sensing on trapped cells by optical tweezers might be difficult (Ramser and Hanstorp, 2010). Alternatively, a functionalized polystyrene bead could be used to measure and exert forces on a cell. When this bead is brought to the cell in the optical trap, the interaction dynamics from the fluorescently labelled membrane molecules and the force on the bead could be measured. Furthermore, the force exerted on polystyrene beads can be higher than on cells, since they are more uniform, have a higher refractive index and can withstand higher laser powers. Therefore, the use of functionalized polystyrene beads enables the manipulation of the contact site by exerting forces on the cell. For example, if the bead is hold at the same position, this might act as a barrier for translocation of interacting molecules, similar to experiments reported by (DeMond et al., 2008) that demonstrated a stick-slip mechanism for TCR translocation.

Peters et al. (1999) describe optical tweezers experiments (not combined with fluorescence microscopy) to study the movement of membrane molecules under applied force (pN range) using a functionalized bead. Thoumine et al. (2008) combined fluorescence microscopy and optical tweezers to study the on-and off-rate of the binding of membrane molecules and the diffusion and recruitment of these molecules. To rupture the binding (ALCAM-ALCAM or ALCAM-CD6) forces of ~ 65 pN are required (te Riet et al., 2007), which is in the order of the maximum force the OT are able to apply. When multiple ALCAM-interactions exist, this implies that terminating the interaction between a functionalized bead and a cell might not be possible, but influencing ALCAM rearrangements on the cell membrane by holding and moving the bead might be possible. Therefore, implementing a detector to measure the deflection of the trapping laser beam in our setup would combine the

abilities of the aforementioned experiments and enable the study of membrane protein dynamics under applied force while monitoring the distribution of the proteins.

6.2.2 Applications of developed methods

Intracellular interactions

The method described here for the measurement of cell spreading and recruitment of membrane molecules can be very fruitfully used to study intracellular interactions upon contact initiation. For example, calcium concentration measurements could reveal early signalling events directly upon interaction (Gunzer et al., 2000) and tyrosine phosphorylation measurements could indicate T-cell receptor activation (Kaizuka et al., 2009). Since dual colour imaging is implemented in the current microscope, both these signalling and membrane protein (for example, CD6) distributions could be visualized simultaneously. This approach allows determining both time and spatial correlations between physical contact, distribution of membrane proteins at the contact site and intracellular signalling events. Furthermore, the presented method can be very well combined with other optical microspectroscopic techniques such as fluorescence resonance energy transfer (FRET) and fluorescence lifetime imaging microscopy. This would allow, for example, to measure colocalisation of molecules on a nanometer scale during cell-cell interactions. Here, it would be very interesting to study dynamic interactions between CD6 and (mediated by Syntenin-1) the cytoskeleton.

Lipid bilayers

We demonstrated that TIRF-OT microscopy can be perfectly well used to study the interaction between a cell and a functionalized surface. A next step could be to induce interactions between cells and supported lipid bilayers. These bilayers can be functionalized with one or more molecules of interest. The molecules in the lipid bilayer are able to move freely in the lateral direction when the cytoplasmic tail is truncated (Groves and Dustin, 2003). In chapter 5, we proposed that cell spreading (increasing the contact site) and recruitment towards the contact site of ALCAM and CD6 are competing processes. If this hypothesis is true, lipid bilayer

experiments might reveal recruitment of membrane molecules towards the contact site, but not cell spreading. Furthermore, experiments on lipid bilayers can reveal quantitative information on the 2D dissociation constant of the interacting molecules, and the amount of (for example) interacting molecules in the contact site (Zhu et al., 2007). This would support and extent the substrate coating and cell surface expression results obtained in chapter 4.

Patterned surfaces

We demonstrated that CD6 is recruited towards the contact site. More detailed information on the cellular mechanisms underlying the recruitment could be revealed by using surfaces that are functionalised in a patterned way. For example, a patterned surface of anti-CD6 and anti-β1-integrin could reveal whether CD6 is specifically recruited towards the anti-CD6 spots, or also to the anti·β1-integrin sites. Furthermore, if the size of anti-CD6 spots in, for example, a bovine serum albumin environment (preventing aspecific interaction), and the distance between the spots are varied, cell spreading and molecular recruitment could be studied separately. In this case, cell spreading would be limited to the spot size, whereas recruitment might be independent of this spot size. Mossman et al. (2005) describe the use of patterned bilayers with boundaries between the different parts. It would be interesting to develop a method in which a raster can be positioned between two cells in cell-cell contact to study the influence of boundaries in this situation. This could reveal whether the influence of spatial organisation and membrane protein dynamics on cell signalling, as pointed out by cell-lipid bilayer experiments is biologically relevant for cell-cell interaction in vivo. One possible approach could be to perform this experiment in a well with cells adhered to the bottom, then adding a raster and letting it sediment by gravity, followed by a second type of cell (with a micropipette, for example), as depicted in Fig. 6.1a.

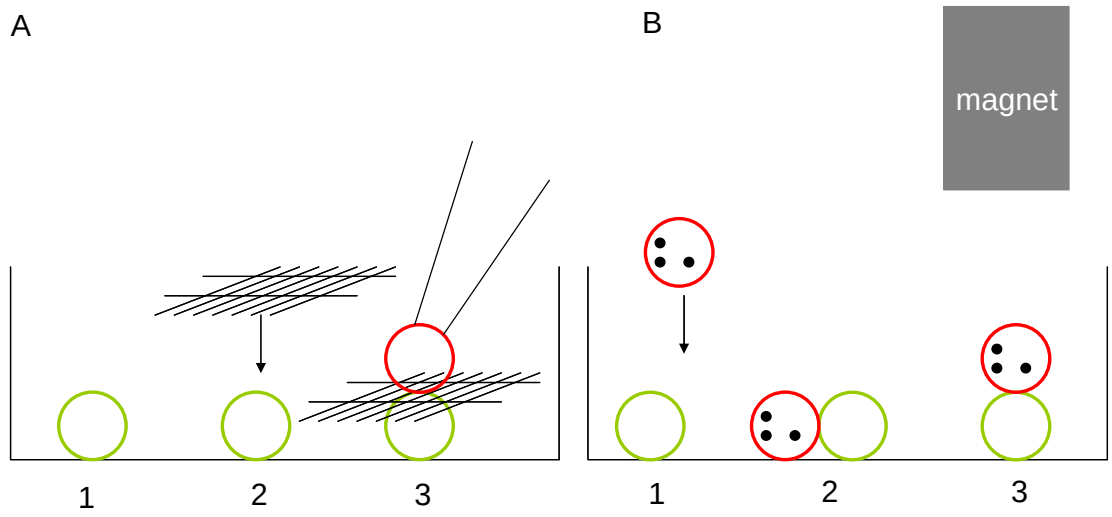

Fig. 6.1 Future experiments (A) To test the influence of hindering membrane dynamics in cell-cell interactions, cells at the bottom (1) can be covered with a grid (2), after which a cell of a second type is brought in contact with the first by means of a micropipette. (B) To test the influence of stress on cell-cell interactions, cells of type B that have phagocytosed magnetic particles can be added to a cell of type A at the bottom (1). After contact initiation (2), a magnet is positioned above the sample to lift the cell of type B, in order to align the contact site in the field of view and to exert a force on the interaction (3).

Hanging configuration

In chapter 4, we showed that cell spreading was influenced by the measurement configuration. In the hanging configuration, cell spreading is lower than in the supported configuration, which we explained by the forces acting on a cell (Fig. 4.6). In the human body, cells are also subjected to forces, for example, shear forces by other cells in the arteries, or forces applied by the extracellular matrix. Measuring cell-substrate or cell-cell interactions in the hanging situation compared to the supported situation might reveal the influence of the forces on a cell with respect to cell spreading and the recruitment of membrane molecules towards the contact site. For example, if cell spreading is smaller in the hanging configuration, and recruitment similar to the supported configuration, this would suggest that recruitment and spreading are not competing processes (as suggested above). In this respect it also might be interesting to apply additional forces on the cells during the interaction which can be done by either the OT or by inducing a flow inside the measuring chamber.

Furthermore, the hanging configuration can be used to measure, in a more sensitive way than traditional microscopy, the influence of certain treatments of the cells (for example, the treatment with DMSO) on cell behaviour. Another possible application is the study of T-cell arrest on dendritic cells and the formation of long-lasting contacts. It has been demonstrated that the amount and quality of peptide-MHC ligands is important for T-cell arrest (Bousso, 2008). Since the hanging configuration influences the formed contact by reducing the contact size, having interaction under external loading of the interacting molecules and influencing the amount of contacts, it would be interesting to use the hanging configuration to influence the amount of stimulating contacts in the formed contact site in order to provide insights into the mechanism of T-cell arrest.

Another method to study the influence of stress on the interaction and the contact size, is the use of magnetic tweezers. Assuming cells of type A are adhered to a glass slide, cells of type B could be added that have phagocytosed magnetic particles (Fig. 6.1b). Once the cells B are sedimented and start to interact with cells A, a magnet can be positioned above the well, to slightly lift cells of type B. In this manner, the interaction site might stay aligned parallel to the focal plane of the objective. The application of this method should be carefully tested so the magnetic particles do not interfere with cellular processes and the force on the binding is not too high to make sure the cells remain in contact. The advantage of magnetic tweezers over OT is the throughput, which can be higher for magnetic tweezers than for OT. The advantage of both magnetic and optical tweezers over shear stress by a fluid stream is that the direction of the force keeps the cells in the field of view (no rolling). These measurements, on the influence of stress on cell interactions, could reveal essential information for, for example, coating vascular grafts with epithelial cells, or other applications in tissue engineering

References

BOUSSO, P. 2008. T-cell activation by dendritic cells in the lymph node: lessons from the movies. *Nature Reviews Immunology,* 8, 675-684.

CHAMARAUX, F., FACHE, S., BRUCKERT, F. & FOURCADE, B. 2005. Kinetics of Cell Spreading. *Physical Review Letters,* 94, 158102.

DEMOND, A. L., MOSSMAN, K. D., STARR, T., DUSTIN, M. L. & GROVES, J. T. 2008. T Cell Receptor Microcluster Transport through Molecular Mazes Reveals Mechanism of Translocation. *Biophys. J.,* 94, 3286-3292.

GROVES, J. T. & DUSTIN, M. L. 2003. Supported planar bilayers in studies on immune cell adhesion and communication. *Journal of Immunological Methods,* 278, 19-32.

GUNZER, M., SCHAFER, A., BORGMANN, S., GRABBE, S., ZANKER, K. S., BROCKER, E. B., KAMPGEN, E. & FRIEDL, P. 2000. Antigen presentation in extracellular matrix: Interactions of T cells with dendritic cells are dynamic, short lived, and sequential. *Immunity,* 13, 323-332.

HUISSTEDE, J. H. G., VAN DER WERF, K. O., BENNINK, M. L. & SUBRAMANIAM, V. 2005. Force detection in optical tweezers using backscattered light. *Optics Express,* 13, 1113-1123.

KAIZUKA, Y., DOUGLASS, A. D., VARDHANA, S., DUSTIN, M. L. & VALE, R. D. 2009. The coreceptor CD2 uses plasma membrane microdomains to transduce signals in T cells. *J Cell Biol*.

MOSSMAN, K. D., CAMPI, G., GROVES, J. T. & DUSTIN, M. L. 2005. Altered TCR signaling from geometrically repatterned immunological synapses. *Science,* 310, 1191-1193.

PETERS, I. M., VAN KOOYK, Y., VAN VLIET, S. J., DE GROOTH, B. G., FIGDOR, C. G. & GREVE, J. 1999. 3D single-particle tracking and optical trap measurements on adhesion proteins. *Cytometry,* 36, 189-194.

RAMSER, K. & HANSTORP, D. 2010. Optical manipulation for single-cell studies. *Journal of Biophotonics,* 3, 187-206.

TE RIET, J., ZIMMERMAN, A. W., CAMBI, A., JOOSTEN, B., SPELLER, S., TORENSMA, R., VAN LEEUWEN, F. N., FIGDOR, C. G. & DE LANGE, F. 2007. Distinct kinetic and mechanical properties govern ALCAM-mediated interactions as shown by single-molecule force spectroscopy. *J Cell Sci,* 120, 3965-3976.

THOUMINE, O., BARD, L., SAINT-MICHEL, E., DEQUIDT, C. & CHOQUET, D. 2008. Optical Tweezers and Fluorescence Recovery After Photo-Bleaching to Measure Molecular Interactions at the Cell Surface. *Cellular and Molecular Bioengineering,* 1, 301-311.

ZHU, D.-M., DUSTIN, M. L., CAIRO, C. W. & GOLAN, D. E. 2007. Analysis of Two-Dimensional Dissociation Constant of Laterally Mobile Cell Adhesion Molecules. *Biophys. J.,* 92, 1022-1034.

Abbreviations

α: characteristic spreading constant (s^{-1})
αCD6: anti-CD6 antibody
λ: wavelength (nm)
θ_i, θ_c: incident, respectively critical, angle (deg. or rad.)
AFM: atomic force microscope
ALCAM: activated leukocyte cell adhesion molecule (CD166)
BA: back-aperture
BPF: band pass filter
BSA: bovine serum albumin
CCD: charged coupled device
CD6: cluster of differentiation 6
CLSM: confocal laser scanning microscopy
CytD: cytochalasin D
d: diffraction limit
d_e: extent of the evanescent field
d_p: penetration depth
D: diffusion constant
DC(s): dendritic cell(s)
DMSO: dimethylsulfoxide
DOF: depth of focus / focal depth
FACS: fluorescence activated cell sorting (flow cytometry)
FBS/FCS: fetal bovine/calf serum
FRAP: fluorescence recovery after photobleaching
FRET: fluorescence resonance energy transfer
FWHM: full width half maximum
gαHu-fc: goat-anti-human-fc antibody
GFP: green fluorescent protein
HILO: highly inclined laminated optical sheet
IMDM: Iscove's modified Dulbecco's medium, type of cell culture medium
IR: infrared
IS: immunological synapse
MHC: major histocompatibility complex
n: refractive index
NA: numerical aperture of a lens
NSOM: near-field scanning optical microscopy

OT: optical tweezers
PBS: buffer of 150mM NaCl, 10 mM PO_4^{3-}, pH 7.4
PLL: poly-l-lysine
R: radius
(m)RFP: (monomeric) red fluorescent protein
RPMI: Roswell Park Memorial Institute, type of cell culture medium
S: size of the contact area
SMAC: supra molecular activation cluster
SPF: short pass filter
SPT: single particle tracking
T-cells: lymphocytes matured in thymus
TCR: T-cell receptor
TIRF: total internal reflection fluorescence
TSM: buffer of 20 mM Tris-HCl (pH 8.0), 150 mM NaCl, 1 mM $CaCl_2$, 2 mM $MgCl_2$

Summary

This thesis describes the development, validation, and application of a hybrid microscopy technique to study cell-substrate and cell-cell interactions in a controlled and quantitative manner. We studied the spatial and temporal dynamics of the selected membrane molecules CD6 and the activated leukocyte cell adhesion molecule (ALCAM), since they appear to play an important role in T-cell activation in the immune system.

Chapter 1 introduced the need for visualization and manipulation techniques with high spatial and temporal resolution in order to obtain detailed information on interaction dynamics of cell membrane molecules. Total internal reflection fluorescence (TIRF) microscopy uses an evanescent field to illuminate the sample, resulting in high signal-to-background images. To align the interaction site in the focal plane of the microscope objective and to visualize the interactions from the precise timepoint of onset of these processes, we use optical tweezers (OT). OT are used to capture and manipulate the cells and to control the induction of the interaction with high spatial and temporal fidelity.

In Chapter 2, we presented the concept, technical design and construction of a hybrid TIRF-OT microscope. We used a commercial microscope, on which we added steerable optical tweezers (in *x,y,z*), prism-based TIRF illumination and two CCD cameras for dual colour detection. Additionally, we described the technical requirements and design of a flowcell that could be used for combined TIRF-OT experiments. Finally, we explained the isodata thresholding method applied for data analysis of the fluorescence images and described the image processing procedure to generate accurate overlap between images from two different cameras.

Chapter 3 demonstrated that the combination of prism-based TIRF microscopy with optical tweezers yields a versatile hybrid method to study cell-substrate interactions. We described the method developed in detail and presented its application to study the interaction of K562 cells, stably expressing GFP-tagged ALCAM with a CD6-functionalized surface. The cells and the size of the contact site were not influenced by the OT. We demonstrated a temporal accuracy of ~ 2s in determining the onset of interaction. Since t=0 s is known, averaging the data acquired from several cells is possible, which facilitates statistically-relevant quantitative analysis of temporal dynamics and reduces the effect of cell-to-cell variations. Furthermore, we showed that K562-ALCAM-GFP cells spread on the surface in accordance with an existing model (time constant ~330 s), based on the force balance between the cell membrane tension and actin polymerization.

Additionally, we described an active redistribution of ALCAM upon contact initiation with a characteristic time of ~35 s. We concluded that spreading, recruitment and redistribution might be distinct but linked processes, which require more detailed study of the underlying mechanisms (such as involvement of the actin cytoskeleton).

We further used the hybrid TIRF-OT method, in chapter 4, to investigate the CD6-induced cell spreading and recruitment of CD6 towards the contact site in the interaction between Jurkat-CD6-RFP cells and a functionalized surface. We showed that Jurkat-CD6-RFP cells spread on anti-CD6 functionalized surfaces in an active process with a possible role for the actin cytoskeleton. Additionally, we observed that the since the cells are hanging on the functionalized substrate in our prism-based TIRF-OT microscope, we are more sensitive to changes in the cell. We also measured recruitment of CD6 towards the contact site on anti-CD6 and non-CD6 specific functionalized surfaces. This recruitment is also an active process. Therefore, we suggest a model in which upon contact with a surface, the actin cytoskeleton is polymerized towards the contact site, delivering the CD6 or dragging the CD6 along. Once at the contact site, the increased actin and CD6 concentration induces cell spreading.

In chapter 5, we tested three manipulation and three visualisation methods to measure cell-cell interactions in a controlled and quantitative manner. We demonstrated that random seeding of the cells gave a six-fold increase in throughput over optical tweezers and micropipette-based methods. However, the latter two approaches can be very well combined with microscopy methods, such that the interaction plane is fully in the field of view. Combinations of highly inclined laminated optical sheet (HILO) microscopy with OT and confocal microscopy with a micropipette are both able to induce contact between two cells in a controlled way, while simultaneously monitoring the interaction site in the field of view. Considering the potential for higher signal-to-background ratio of confocal microscopy and the better long-term throughput of the optical tweezers, we recommend a combination of these techniques for optimally controlled quantitative visualisation of cell-cell interactions.

Finally, in chapter 6, we presented a perspective on fruitful future approaches. In particular, we suggested implementing multiple traps to study cell-cell interactions in a detailed manner and with higher throughput. Furthermore, the OT could be used as a force transducer to measure the influence of (applied) forces on the interaction dynamics. We also recommend performing experiments with lipid bilayers and patterned substrates to elaborate on the mechanisms of membrane protein recruitment and cell spreading.

Samenvatting

Dit proefschrift beschrijft de ontwikkeling, validatie en toepassing van een hybride microscopietechniek voor het gecontroleerd en kwantitatief bestuderen van cel-substraat en cel-celinteracties. We hebben de ruimtelijke en temporale dynamica van de membraanmoleculen CD6 en ALCAM (*activated leukocyte cell adhesion molecule*) bestudeerd, omdat zij een belangrijke rol blijken te spelen in de activatie van T-cellen in het immuunsysteem.

Hoofdstuk 1 introduceert de noodzaak van visualisatie- en manipulatie-technieken om gedetailleerde informatie over de interactiedynamica van celmembraanmoleculen te verkrijgen. Totale interne reflectie fluorescentie (TIRF) microscopie maakt gebruik van een evanescent veld om het sample te belichten, wat resulteert in afbeeldingen met een hoge signaal-achtergrondverhouding. Om het interactievlak volledig in het focusvlak van het microscopie-objectief uit te lijnen en de interacties precies vanaf de start van de interactieprocessen te visualiseren, gebruiken we een optisch pincet (OT). OT gebruiken we om de cellen vast te pakken, te manipuleren en de interactie gecontroleerd te starten met een hoge ruimtelijke en temporale nauwkeurigheid.

In hoofdstuk 2 presenteren we het concept, het technische ontwerp en de constructie van de hybride TIRF-OT microscoop. We hebben een commercieel verkrijgbare microscoop als basis gebruikt waaraan we bestuurbare OT (in *x,y,z*), TIRF belichting met behulp van een prisma en twee CCD camera's voor tweekleurendetectie hebben toegevoegd. Daarnaast beschrijven we de technische vereisten en het ontwerp van een stroomcel die gebruikt kan worden voor de TIRF-OT-experimenten. Tenslotte leggen we de *isodata threshold* methode uit, die gebruikt wordt voor de analyse van de fluorescentieafbeeldingen en beschrijven we de procedure om de afbeeldingen van de twee cameras goed te overlappen.

Hoofdstuk 3 laat zien dat de combinatie van prisma-TIRF-microscopie met een optische pincet een vruchtbare methode opleverd om cel-substraatinteracties te bestuderen. We beschrijven de ontwikkelde methode in detail en presenteren de toepassing door middel van de interactie tussen K562 cellen (stabiel getransfecteerd met ALCAM gelabeld met een groen fluoriserend eiwit (GFP)) met een CD6 gefunctionaliseerd oppervlak. De cellen en de grootte van het contactoppervlak werden niet beinvloed door de OT. We laten zien dat we een temporale nauwkeurigheid hebben van ~2s in het bepalen van het startpunt van de interactie. Omdat t=0 s bekend is, is het mogelijk om de data van meerdere cellen te middelen, wat meer statistisch-relevante kwantitative analyse van temporale dyanmica

mogelijk maakt en het effect van variaties tussen cellen verminderd. Daarnaast laten we zien dat K562-ALCAM-GFP celspreiding op het oppervlak beschreven kan worden met een bestaand model, gebaseerd op de krachtbalans tussen membraanspanning en actinepolymerisatie (tijdsconstante ~330 s). Verder beschrijven we de actieve herverdeling van de ALCAM na contact-initiatie met een karakteristieke tijd van ~35s. We concluderen dat spreiding, recruitment en redistributie mogelijk verschillende maar verbonden processen zijn, die een meer gedetailleerd onderzoek van de onderliggende mechanismen (zoals bijvoorbeeld de betrokkenheid van het actine cytoskelet) nodig maken.

Verder hebben we de hybride TIRF-OT methode gebruikt, in hoofdstuk 4, om CD6-geinduceerde celspreiding en recrutering van CD6 naar het interactievlak tussen Jurkat-CD6-RFP cellen een een gefunctionaliseerd oppervlak. We laten zien dat Jurkat-CD6-RFP cellen spreiden op anti-CD6 gefunctionaliseerde oppervlakken door middel van een actief proces met een mogelijk rol voor het actine cytoskelet. Daarnaast observeren we dat de cellen hangend onder het oppervlak in onze prisma-TIRF microscoop gevoeliger zijn voor veranderingen in de cellen. We hebben recrutering van CD6 naar het interactievlak op anti-CD6 en niet-CD6-specifieke gefunctionaliseerde oppervlakken gemeten. Deze recrutering was een actief proces. Onze metingen suggereren een model waarbij door het contact met het oppervlak het actine cytoskelet polymeriseert richting het interactievlak, CD6 met zich meenemend. Eenmaal in het interactievlak zorgen de toegenomen hoeveelheid actine en CD6 voor celspreiding.

In hoofdstuk 5 hebben we drie manipulatie en drie visualisatiemethoden getest om cel-celinteracties te meten op eengecontroleerde en kwantitatieve manier. We hebben laten zien dat het willekeurig zaaien van cellen op het oppervlak een zesvoudige vergroting van de verwerkingscapaciteit geeft ten opzichte van een OT of een micropipet, maar dat de laatste twee werkwijzen goed gecombineerd kunnen worden met microscopiemethoden zodat het interactievlak in het focusvlak van de microscoop ligt. Combinaties van HILO (*highly inclined laminated optical sheet*) microscopy met OT en confocale microscopie met een micropincet zijn beide in staat tot het induceren van een interactie tussen twee cellen op een gecontroleerde manier, terwijl intussen het interactievlak wordt bestudeerd. Gezien de mogelijkheden van een hoge signaal-achtergrondverhouding in confocale microscopie en de betere langetermijnverwerkingscapaciteit van OT, bevelen wij een combinatie van deze technieken aan voor een optimale, gecontroleerde en kwantitatieve visualisatie van cel-celinteracties.

Tenslotte, in hoofdstuk 6, presenteren we een toekomstperspectief voor vruchtbare toekomstige aanpakken. In het bijzonder suggereren we het implementeren van meerdere OT om cel-celinteracties te kunnen bestuderen met

een hogere verwerkingscapaciteit. Daarnaast zouden OT gebruikt kunnen worden voor het meten van de invloed van (uitgeoefende) krachten op de interactiedynamica. We raden ook aan om experimenten uit te voeren met lipide membranen en gepatroneerde oppervlakken om de mechanismen van membraaneiwitrecrutering en celspreiding beter te kunnen onderzoeken.

Dankwoord

Aan het einde van mijn promotietraject gekomen, is de tijd daar om terug te kijken en te bedanken. Veel mensen hebben eraan bijgedragen dat dit proefschrift tot stand is gekomen, zowel met inhoudelijke en huishoudelijke ondersteuning van het project als door support van mij als persoon.

Vinod, dank je wel dat je me stimuleerde om te komen promoveren. Dank je wel voor je enthousiasme en positieve insteek van het onderzoek en voor je motiverende woorden als het allemaal eens lastiger was. Ook als een gesprek geen concrete antwoorden of oplossingen had opgeleverd, dan nog voelde ik me gesterkt om er weer tegenaan te gaan. Bedankt ook voor je open, toegankelijke houding. Veel succes met het tot grote hoogten brengen van NBP.

Hans, ook jij van harte bedankt voor je ondersteuning. Dank je wel dat ik makkelijk bij je naar binnen kon lopen en dat je ook praktisch in het lab wilde meewerken aan de opstelling. Ook je kritische blik over de meer theoretische, modelmatige kant van de vraagstelling en de resultaten was heel nuttig en hield me scherp. Succes gewenst om de biologische vraagstukken en natuurkundige technieken te combineren tot een doorgaande en vruchtbare combinatie.

Dit proefschrift is het resultaat van een duidelijk multidisiplinair project. Carl, bedankt dat je meedeed in mijn project. Ik heb veel mogen leren van je andere (biologische) kijk op de dingen en je gedreven houding. Jammer dat je niet mijn co-promotor kon zijn om de samenwerking ook een meer formele status te geven. Alessandra, dank je wel voor je down-to-earth benadering van de ideeen en resultaten waar ik mee kwam. Je kritische vragen en praktische support hebben een belangrijke bijdrage geleverd aan de biologische kant van dit proefschrift. Bernd, dank je wel voor jouw bijdragen in de data analyse van alle images die ik heb genomen. Zonder jouw kennis van image analysis was het heel moeilijk geworden om ook maar enige kwantitatieve conclusies te trekken uit de data.

I would also like to use this opportunity to thank the other members of the thesis committee for their input, for allowing me to defend my thesis and for being part of the defense-ceremony. Thank you, professor Boller, professor French, professor Neefjes, and professor Terstappen.

Veel mensen hebben mij geholpen bij de inhoudelijke en technische kanten van het onderzoek. Bedankt, Aufried (het levende optica handboek), Frans, Johan, Erwin, Christian (die bleef helpen, ook als de FACS eens geen zin had), Kees (precieze, grondige flow-cell fabrikage), Robert (de laser expert), Martin en Rob

(dat ik jullie lasers mocht gebruiken toen die van mij het niet meer deden), Kirsten, Yvonne, Marloes en Wilma (voor jullie geduld om een natuurkundige de cel en biochemische kennis te laten ontdekken en toepassen), Tom (dé bioloog), Martijn van Raaij (voor de experimenten met de AFM), Jesse Szepieniec en Leon Buikstra (de bachelorstudenten die de micropipetexperimenten hebben uitgevoerd), Alma Dudia en Aurel Ymeti (voor de interferometrymeting). Allemaal heel erg bedankt!

Ook wil ik graag van de gelegenheid gebruikmaken om de mensen in Nijmegen en Barcelona te bedanken voor het meedenken tijdens de (SMART) meetings en de goede sfeer als we elkaar ontmoeten. In het bijzonder wil ik Ben (voor de introductie op cellen en het imagen van cellen), Inge Beeren (voor het stabiel transfecteren van de RAW-ALCAM-GFP cellen), Marjolein Meddens (voor het stabiel transfecteren van de Jurkat-CD6-RFP cellen), Joost, Agnieszka, en Maria noemen.

Naast de vakinhoudelijke support, hierboven genoemd, zijn er nog veel meer mensen om te bedanken. Om te beginnen mijn kamergenoten. Christian, Dianwen, Cynthia, Chien-Ching, Malte, Geert, Daniele, Cicerone, Shashank en Inge, heel hartelijk bedankt voor jullie gezelligheid en support. Ik hoop dat ik jullie niet teveel van jullie werk heb gehouden ;-). Chien-Ching, thank you for your friendship, I'll miss our conversations. I'm very happy you can be my paranymph. Kim, ook jij heel erg bedankt voor de gezelligheid, dat we het over van alles konden hebben en dat je mijn paranimf wilt zijn. Succes met het afronden van je eigen onderzoek! Sylvia heel erg bedankt voor je ondersteuning en meeleven. Ook wil ik Roy, Janine, Maryana, Tomasz, Arjen, Bart, Mireille, Cees, Liesbeth, Remco, Peter en alle BPE groepsleden bedanken voor hun tijd en hulp, gezelligheid en aandacht op allerlei terreinen en ook tijdens de gezamelijke koffie- en lunchpauzes (die ik zal gaan missen). Tenslotte wil ik nog het Female Faculty Network Twente bedanken dat ik als bestuurslid een tijd mee mocht kijken en werken in de keuken van de universiteit. Ik geloof dat wij (vrouwen) een waardevolle, onmisbare bijdrage kunnen leveren aan de maatschappij en de organisaties waar we werkzaam in zijn door onze manier van werken.

Tot slot wil ik ook Harm Frederik, Ruben, mijn familie, mijn vrienden, bijbelstudiemaatjes en schaatsmaatjes heel erg bedanken. Zonder jullie ondersteuning, gezelligheid en afleiding waren de afgelopen jaren veel minder goed en leuk geweest.

Bedankt!
Marieke

Controlled initiation and quantitative visualization of cell interaction dynamics - Marieke Snijder-van As

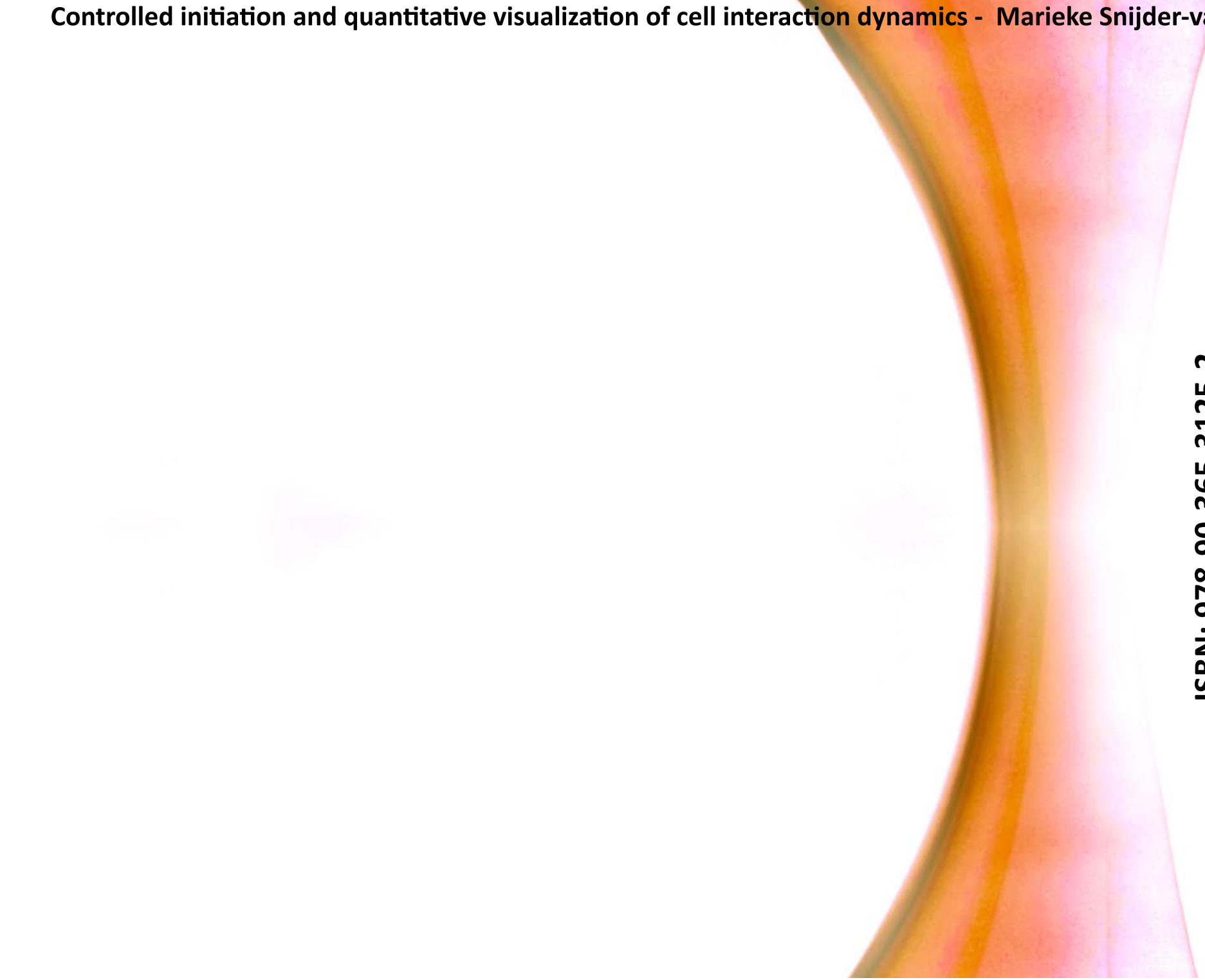

ISBN: 978-90-365-3125-2